Institut für Physik und Astronomie
Arbeitsgruppe III

Stochastic re-acceleration of particles in supernova remnants

Dissertation
zur Erlangung des akademischen Grades
"doctor rerum naturalium"
(Dr. rer. nat.)
in der Wissenschaftsdisziplin "Theoretische Astroteilchenphysik"

eingereicht an der
Mathematisch-Naturwissenschaftlichen Fakultät
der Universität Potsdam

von
Alina Wilhelm
geboren am 12.06.1986 in Omsk

Potsdam, den 13.01.2021

Supervisor:
Prof. Dr. Martin Pohl

Reviewers:
Prof. Dr. Christoph Pfrommer
Prof. Dr. Julia Tjus

Published online on the
Publication Server of the University of Potsdam:
https://doi.org/10.25932/publishup-51291
https://nbn-resolving.org/urn:nbn:de:kobv:517-opus4-512915

Acknowledgments

This dissertation would not be possible without support and guidance from many people to whom I want to express my deep gratitude. First and foremost, this is my supervisor Prof. Dr. Martin Pohl, who gave me the opportunity to accomplish a doctorate and to experience the routine of the scientific world. Secondly, I am grateful to my co-mentor and collaborator Dr. Igor Telezhinsky, with whom it was always a pleasure to work.

Also, I would like to extend my sincere gratitude to the reviewers Prof. Dr. Christoph Pfrommer and Prof. Dr. Julia Tjus, as well as the chairman and the members of the examination committee.

I owe a particular debt to Dr. Robert Brose and Dr. Iurii Sushch, who have taken the task of advising me and proofreading this dissertation, as well as Dr. Pau Amaro Seoane, and Dr. Andrew Taylor for giving me their general impression and numerous comments about this work.

Further, I want to offer my acknowledgments to my former colleagues: Dr. Shan Gao, Dr. Artem Bohdan, Vasundhara Shaw, Heshou Zhang, Dr. Iman Rafighi, Dr. Nils Håkansson, Dr. Anton Baushev, Dr. Robert Rettig, Dr. Simone Federici, Dr. Arjen van Vliet, Dr. Leonel Hernandez, Dr. Xavier Rodrigues, and Samata Das. Furthermore, I am grateful to my collaborators Dr. Vikram Dwarkadas, Dr. Sajan Kumar and the entire VERITAS collaboration. I offer a special thanks to Prof. Dr. Karl Jansen and Dr. Walter Winter for their help and advice during the compilation of this dissertation.

Moreover, I want to express my gratitude to my parents Galina and Alexander Wilhelm, and my best friend Katharina Suhanova. Last but not least, I thank my husband Igor Isaev. I cannot emphasize enough how important were his loving support and patience in all these years.

Table of contents

Abstract

Supernova remnants (SNRs) are discussed as the most promising sources of galactic cosmic rays (CR). The diffusive shock acceleration (DSA) theory predicts particle spectra in a rough agreement with observations. Upon closer inspection, however, the photon spectra of observed SNRs indicate that the particle spectra produced at SNRs shocks deviate from the standard expectation. This work suggests a viable explanation for a softening of the particle spectra in SNRs. The basic idea is the re-acceleration of particles in the turbulent region immediately downstream of the shock. This thesis shows that the re-acceleration of particles by the fast-mode waves in the downstream region can be efficient enough to impact particle spectra over several decades in energy. To demonstrate this, a generic SNR model is presented, where the evolution of particles is described by the reduced transport equation for CR. It is shown that the resulting particle and the corresponding synchrotron spectra are significantly softer compared to the standard case. Next, this work outlines RATPaC, a code developed to model particle acceleration and corresponding photon emissions in SNRs. RATPaC solves the particle transport equation in test-particle mode using hydrodynamic simulations of the SNR plasma flow. The background magnetic field can be either computed from the induction equation or follows analytic profiles. This work presents an extended version of RATPaC that accounts for stochastic re-acceleration by fast-mode waves that provide diffusion of particles in momentum space. This version is then applied to model the young historical SNR Tycho. According to radio observations, Tycho's SNR features the radio spectral index of approximately -0.65. In previous modeling approaches, this fact has been attributed to the strongly distinctive Alfvénic drift, which is assumed to operate in the shock vicinity. In this work, the problems and inconsistencies of this scenario are discussed. Instead, stochastic re-acceleration of electrons in the immediate downstream region of Tycho's SNR is suggested as a cause for the soft radio spectrum. Furthermore, this work investigates two different scenarios for magnetic-field distributions inside Tycho's SNR. It is concluded that magnetic-field damping is needed to account for the observed filaments in the radio range. Two models are presented for Tycho's SNR, both of them feature strong hadronic contribution. Thus, a purely leptonic model is considered as very unlikely. Additionally, to the detailed modeling of Tycho's SNR, this dissertation presents a relatively simple one-zone model for the young SNR Cassiopeia A and an interpretation for the recently analyzed VERITAS and *Fermi*-LAT data. It shows that the γ-ray emission of Cassiopeia A cannot be explained without a hadronic contribution and that the remnant accelerates protons up to TeV energies. Thus, Cassiopeia A is found to be unlikely a PeVatron.

Nomenclature

CD	Contact discontinuity
CMB	Cosmic microwave background
CR	Cosmic rays
DSA	Diffusive shock acceleration
IC	Inverse-Compton
IR	Infra-red
ISM	Interstellar medium
MHD	Magnetohydrodynamic
NLDSA	Non-linear diffusive shock acceleration
NTB	Non-thermal bremsstrahlung
RATPaC	Radiation Acceleration Transport Parallel Code
SED	Spectral energy distribution
SNR	Supernova remnant
TTD	Transit-time damping

Foreword

For this dissertation, I have gathered three articles that I have published together with my collaborators in the last years. A common thread for all three publications is the particle acceleration in supernova remnants (SNRs). The order I have chosen to present these works in my thesis is not chronological, but logical and allows the reader to follow a natural flow of ideas to better picture the main tasks of this dissertation. Here, in the foreword, I give concise explanations for the goals and motivation of every individual article. The papers are then presented in a distributed fashion in the next chapters.

[Article I] presents very detailed modeling of Tycho's SNR. The project revealed the difficulties to explain the available data of Tycho's SNR self-consistently within the common theory of particle acceleration in SNRs. A particular problem was the inconsistency between the observed radio spectrum and the synchrotron emission predicted within the conventional picture of particle acceleration at SNRs shocks. Therefore, this project gave rise to the idea of stochastic re-acceleration of particles immediately behind the forward shock of an SNR, which has become the main topic of this thesis. Based on that idea, I established a comprehensive model for the observations from Tycho's SNR and outlined the shortcomings and inconsistencies of the previous approaches to model this remnant. To this end, I used hydrodynamic simulations performed by my collaborator Dr. Vikram Dwarkadas and a detailed code for particle acceleration and transport, called RATPaC, originally designed by my collaborator and co-supervisor Dr. Igor Telezhinsky. I extended the latter code and modified it to account for the stochastic re-acceleration process and diffusive shock acceleration simultaneously.

[Article II] is the natural side project of **[Article I]**, which generally investigates the impact of stochastic re-acceleration inside SNRs. Having realized by the case of Tycho's SNRs that the detailed self-consistent modeling of SNR requires an additional ingredient and that the stochastic re-accelerations immediately behind the SNRs shocks is a promising concept, I focused on that phenomena. Thus, the goal of this work was a better understanding of the impact of stochastic re-acceleration on electron spectra produced in SNRs. In the first part, the article provides a theoretical basis for the further study of stochastic re-acceleration inside SNRs, developed by my supervisor and collaborator, Prof. Dr. Martin Pohl. At the beginning, the paper examines three different types of turbulence and presents analytical calculations for the corresponding momentum-diffusion coefficient for each type of waves. Having

established that the fast-mode waves are the only type of turbulence that can significantly contribute to the stochastic re-acceleration process, the article continues with a generic model for SNRs and presents electron spectra modified by stochastic re-acceleration. The resulting spectra are significantly softer than that predicted by the convenient picture. To model the electron re-acceleration, I solved the reduced transport equation numerically and calculated the spectral indices of the corresponding radio emission. The paper demonstrates that the stochastic re-acceleration is a viable explanation for the observed soft radio spectra from many SNRs. Once this project was completed, I returned to work presented in **[Article I]**.

[Article III] is a work published within the VERITAS (Very Energetic Radiation Imaging Telescope Array System) collaboration, which presents recent γ-ray data of the young SNR Cassiopeia A. The data observed with the VERITAS telescope was analyzed by Dr. Sajan Kumar, another leading author of this paper. As one of the few theoreticians specialized in SNRs in the VERITAS collaboration, I decided to interpret the data. Thus, I performed the theoretical modeling for the entire spectral energy distribution of Cassiopeia A. To perform the modeling, again I used parts of RATPaC. This work establishes characteristic features of Cassiopeia A, such as particle spectral indices, the corresponding maximum energy, and the maximal magnetic field inside the remnant. Like in the case of Tycho's SNR, the spectra derived for electrons and protons distributions in Cassiopeia A are significantly softer than predicted by the standard theory.

Since all of the articles have been published in collaboration, it might be difficult to understand what my contribution was. To clarify this point, I present here the list of published papers and a note indicating what my contribution has been. Additionally, at the beginning of each chapter, I give a reference to the article from which the chapter has benefited. For the full titles of the papers, acronyms, as well as an explanation of my contribution and journal references, see the following table of publications.

List of featured articles

[Article I] "Stochastic re-acceleration and magnetic-field damping in Tycho's SNR".

Astronomy and Astrophysics, Volume 639, article number A124, 14 pp. (2020).
A. Wilhelm, I. Telezhinsky, V. V. Dwarkadas and M. Pohl

My contribution: Using hydrodynamical simulations of my collaborator Dr. Vikram Dwarkadas I performed the entire modeling and wrote most of the text.

[Article II] "Reacceleration of electrons in SNRs".

Astronomy and Astrophysics, Volume 574, article number A43, 11 pp. (2015).
M. Pohl, **A. Wilhelm** and I. Telezhinsky

My contribution: I numerically solved the reduced transport equation and calculated all the electron and synchrotron spectra.

[Article III] "Evidence for proton acceleration up to TeV energies based on VERITAS and *Fermi*-LAT observations of the Cassiopeia A SNR".

Astrophysical Journal, Volume 894, Number 1, p 51. (2020).
A.U. Abeysekara et al. (The VERITAS Collaboration)

My contribution: I performed the theoretical modeling and interpretation of the data and wrote the corresponding section for the article.

Chapter 1

Introduction

Supernova remnants (SNRs) are among the most exciting astrophysical objects because they may shed light on a major question of physics: the origin of cosmic rays (CR).

Despite misleading denotation, which is historically determined, CR are energetic particles that permeate the Universe. Discovered for the first time about hundred years ago by Victor Hess (Hess (1912), Hess (2018)[1]), the phenomena of CR still provide fascinating and challenging tasks. The production of CR is still ambiguous, despite the remarkable progress that has been done in this field. CR reveal the following composition: ∼88% protons, ∼10% helium nuclei, ∼1% nuclei of heavier particles, and ∼1% electrons and positrons. Hence the charged nature of CR prevent from retracing their sources, as the particles get manifoldly deflected in the galactic and intergalactic magnetic fields. Therefore, the researchers have to rely on indirect observations, such as the detection of neutral-charged mediators produced in CR interactions. In this regard, an important role is played by photons, which can be observed across the whole electromagnetic spectrum.

The differential flux of CR obtained by numerous experiments is presented in Figure 1.1. Remarkably, the CR spectrum expands over 13 decades in energy and outreaches energies typical for large particle colliders. Above $\sim$ 100 GeV, the observed flux forms a power law in energy, E^{-s}, with a spectral index, s, close to 3. The green dashed line in Figure 1.1 is an analytical power-law function with a spectral index of 3, intended to visualize the rough behavior of the overall spectrum. On closer look, the region between $\sim$ 100 GeV and a few PeV features the spectral index of $s \approx 2.7$. The distinct kink around few PeV is called the *knee* of the CR spectrum. Another prominent kink is the so-called *ankle* at a few EeV. The spectrum in the energy range between knee and ankle is slightly softer with spectral index of $s \approx 3.1$. Above the ankle, the CR spectrum hardens again to $s \approx 2.6$. Figure 1.2 presents the differential CR spectrum between 10^{13} and 10^{20} eV that is multiplied by $E^{2.6}$ in order to make the knee and the ankle more visible.

It is generally assumed that the particles detected with energies below $\sim$ 10 GeV are mainly the solar CR. The particles with energies above the ankle are considered to be from extragalactic origin since their gyroradii exceed the size of the Galaxy. Consequently, CR below the knee, and hence with energies less than a PeV, are believed to emerge within our Galaxy. At the highest energies of $\sim 10^{20}$ eV, the CR flux terminates.

[1]English translation of the work Hess (1912), which is originally in German.

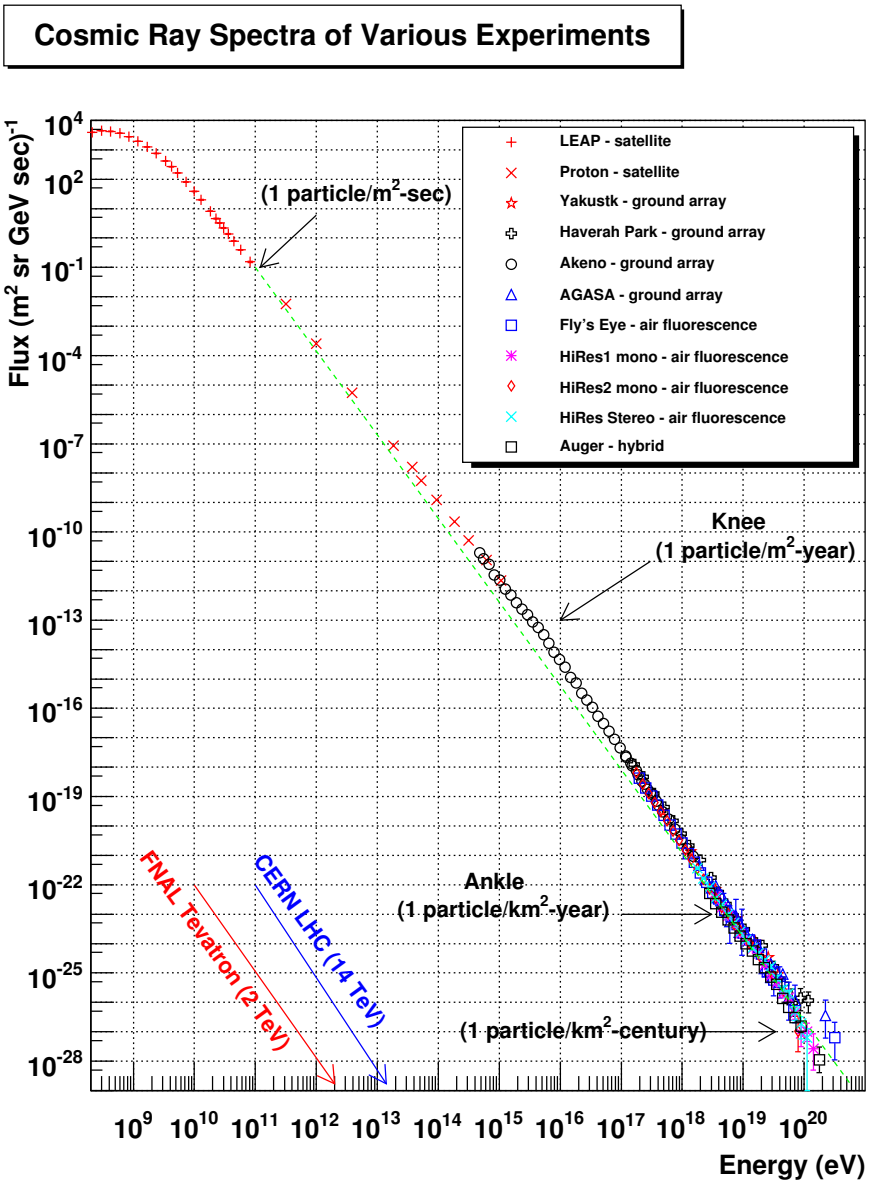

Figure 1.1: Overall CR flux as a function of energy observed by diverse experiments. Figure is taken from Hanlon (2008).

This fact is usually referred to as the theoretically predicted Greisen-Zatsepin-Kuzmin cutoff (Greisen, 1966). According to Greisen (1966), the supression of cosmic protons with energies 10^{20} eV and higher is interpreted to occur due to their inevitable inelastic scattering on the photons provided the cosmic microwave background (CMB). More precisely, when propagating through CMB, protons with energies above $\sim 6 \times 10^{19}$ eV interact with photons and generate a Delta resonance. This particle is unstable and decays via two channels: proton plus neutral pion or neutron plus positive pion. Throughout this process, the parent proton changes its direction and losses about 20 percent of its energy.

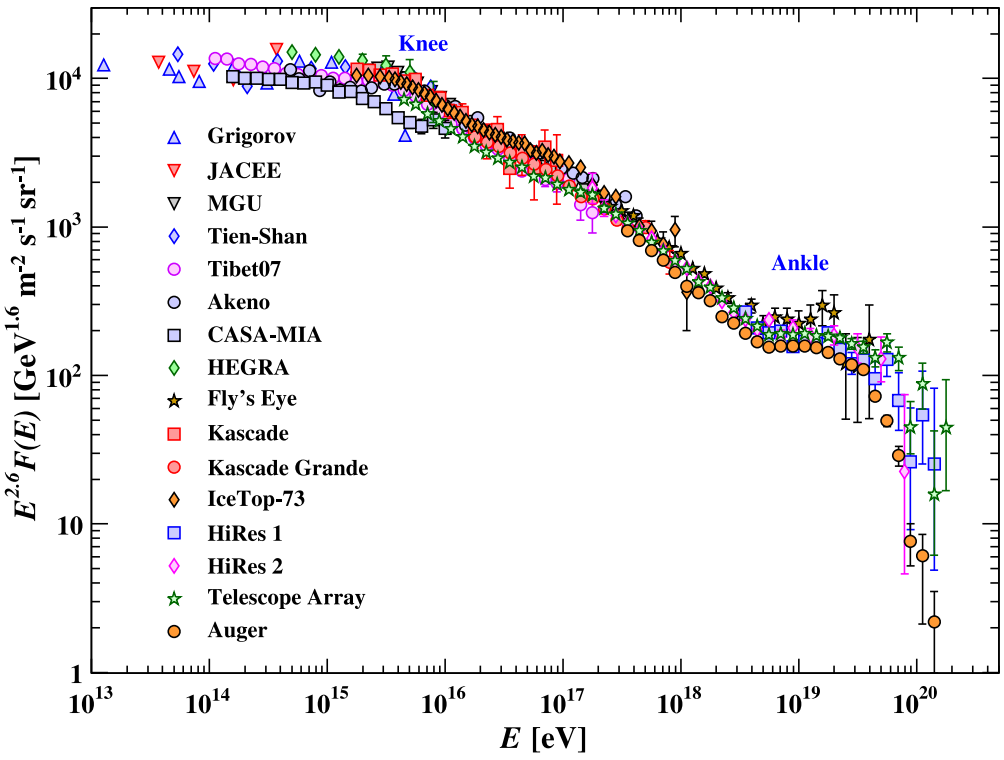

Figure 1.2: Differential CR spectrum multiplied by $E^{2.6}$. Figure is adapted from Patrignani et al. (2016).

The proton-photon interactions reoccur as long as the energy of the proton stays above the threshold $\sim 6 \times 10^{19}$ eV, required to generate the Delta resonance. For extragalactic sources, the probability that the proton with energy above this limit does not scatter on CMB photon and thus reaches the Earth is close to zero. Consequentially, no protons above Greisen-Zatsepin-Kuzmin limit can be detected.

Baade and Zwicky (1934) first proposed that the CR might originate from exploding stars, i.e., supernovae. As of today, SNRs, which are the relics of the stellar explosions, remain the most promising sources of galactic CR. First of all, because their energy is sufficient to maintain the CR energy flux in our Galaxy (Ginzburg and Syrovatskiĭ, 1966). Additionally, diffusive shock acceleration (DSA), which is the standard theory for particle acceleration at astrophysical shocks, predicts a power-law particle spectrum with the spectral index of 2 for strong shocks and test-particle limit (e.g., Bell, 1978a), which is in rough agreement with the observed CR flux. Indeed galactic CR observed at the Earth show a power law with spectral index ≈ 2.7. Corrected for the propagation effects

in our Galaxy, the spectral index at the source is obtained to be $\approx 2.2 - 2.4$ (Strong and Moskalenko, 1998; Strong et al., 2000; Putze et al., 2009). Furthermore, there is extensive observational evidence in the form of radio emission, X- and γ-ray photons detected from many SNRs (e.g., Koyama et al., 1995; Bamba et al., 2003; Aharonian et al., 2004, 2006; Green, 2009; Helder et al., 2012; Ackermann et al., 2013), which indicates in situ production of CR inside SNRs. Theoretical estimations show (e.g., Hillas, 2005) that SNRs are capable to accelerate particles up to a PeV and thus able to account for the CR spectrum up to the knee. The present work is solely focused on galactic CR and SNRs as their production sites. Thus, hereafter we always refer to galactic CR with energies below PeV.

Despite the wide agreement on SNRs being sources of CR, several discrepancies in this field remain unsolved, and hence many details are still in discussion. On closer inspection, the multi-wavelength data from various SNRs suggest that the actual particle spectra in SNR significantly differ from simple power-laws and are often softer than expected from DSA (e.g., Green, 2009). Therefore, further investigations and sophisticated models are needed to understand the numerous details of particle acceleration in SNRs. The goal of this thesis is to demonstrate the above-mentioned deviations from the standard theory on particular objects. Furthermore, this work presents a new scenario that involves stochastic re-acceleration of particles in the immediate downstream region of SNRs. It is shown that this scenario is able to explain the observed soft radio spectra of SNRs.

This work is organized as follows: In Chapter 2, the theory and basic concepts of particle acceleration in SNRs are reviewed. We introduce general aspects and a generic model for stochastic re-acceleration inside SNRs via fast-mode waves in Chapter 3. Chapter 4 is dedicated to the description of RATPaC, a code that is designed for the detailed modeling of SNRs. One of the main tasks of this thesis is to include the process of stochastic re-acceleration into RATPaC; the corresponding details are also presented in Chapter 4. We apply RATPaC to model the young SNR Cassiopeia A in Chapter 5. Therein, we review a model for Cassiopeia A SNR, which explains the recently observed VERITAS and *Fermi*-LAT data. Finally, Chapter 6 presents a global model for Tycho's SNR, where the extended version of RATPaC, which accounts for stochastic re-acceleration, is used.

Chapter 2

Basic theory

In this chapter, the current state of the field of particle acceleration in SNRs is presented. The theoretical study of SNRs as sources of high energy particles is based on the understanding of two fundamental fields. First of all, it is the knowledge about the time-evolution of SNR as a macroscopic object, described by the hydrodynamic equations. Secondly, one needs to understand the microscopic processes responsible for particle acceleration inside an SNR. Hence, firstly a brief overview of the dynamic evolution of SNRs is given, followed by an introduction to the particle acceleration mechanisms.

2.1 Evolution of SNRs

An SNR is the outcome of a violent explosion of a massive star, i.e., a supernova. In such events, an enormous amount of energy is quickly released, and the envelope of a star is ejected at supersonic velocities. This process gives rise to a double-shocked structure consisting of a forward shock expanding into the stellar environment and a reverse shock that propagates back into the ejecta.

A simplified structure of a young SNR, which is usually observed and predicted by hydrodynamic simulations, is depicted in Figure 2.1. The forward shock sweeps up and compresses the surrounding medium (blue-shaded area), which is consequentially heated to very high temperatures, of the order of $\sim 10^9$ K. The shocked ambient medium and the stellar ejecta are separated by the contact discontinuity (CD), marked as the green-shaded area. As the reverse shock propagates back through ejecta, it consequentially reheats and decelerates the ejecta. The shocked ejecta is depicted as the orange-shaded area in Figure 2.1. It is important to stress here that for young SNRs, the reverse shock is moving backward in a Lagrangian sense: it propagates inward in the rest-frame of the forward shock but expands outward in the observer rest-frame.

The time-evolution of an SNR can be roughly divided into four phases. After the explosion, the ejected stellar mass is moving outward into the surrounding medium with a supersonic speed, $\sim 10^4$ km/s. It pushes the ambient material generating a shock wave with radial velocity, i.e., the forward shock. In the first phase, this shock wave created by the explosion expands with no resistance to the interstellar medium (ISM). Therefore, this development period is called the *free expansion phase*. The entire energy of the explosion,

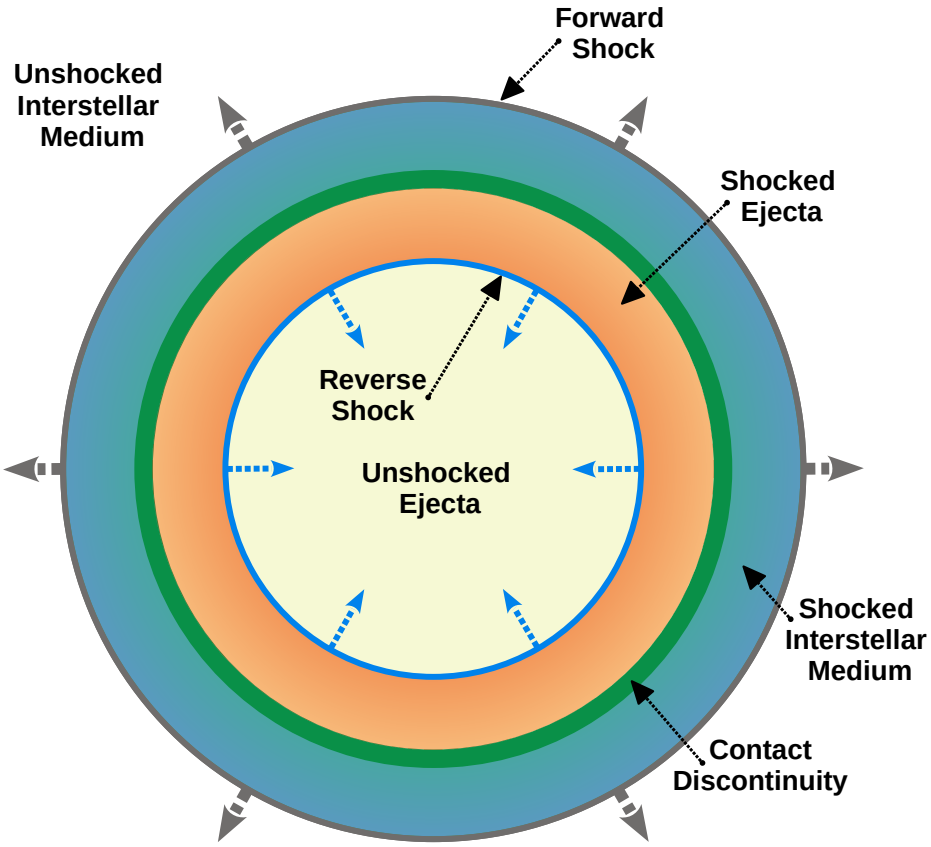

Figure 2.1: Schematic structure of a young SNR.

$E_{\rm SN}$, is carried by the ejected stellar mass, M_e, and the shock speed can be approximated by the relation

$$V_{\rm sh} \simeq \left(\frac{2E_{\rm SN}}{M_e}\right)^{1/2} . \tag{2.1}$$

The shock radius scales then in time, t, with the constant shock speed as

$$R_{\rm sh}(t) \simeq V_{\rm sh}\, t\,. \tag{2.2}$$

The free expansion terminates when the forward shock accumulates an amount of the ambient material, which is of the order of the ejecta mass. Hence the swept-up material starts to affect the dynamics of the remnant and to slow down the shock's motion. This condition can be roughly expressed by equating the swept-up mass with the ejecta mass. The shock radius that marks the end of the free expansion phase is then given by

$$R_{\rm sw} = \left(\frac{3M_e}{4\pi\rho_{\rm ISM}}\right)^{1/3} , \tag{2.3}$$

where $\rho_{\rm ISM}$ is the ambient density. The corresponding age of an SNR is typically a few

hundred years. From that moment, the remnant enters the *Sedov-Taylor phase* (Sedov, 1959; Taylor, 1950), in which the SNR expands adiabatically. The energy losses are negligible, and the cooling of the hot plasma occurs solely due to its expansion. The shock dynamic can be described by the adiabatic blast-wave solutions

$$R_{\mathrm{sh}}(t) = \eta_0 \left(\frac{E_{\mathrm{SN}}}{\rho_{\mathrm{ISM}}} \right)^{1/5} t^{2/5}, \tag{2.4}$$

$$V_{\mathrm{sh}}(t) = \eta_0 \frac{2}{5} \left(\frac{E_{\mathrm{SN}}}{\rho_{\mathrm{ISM}}} \right)^{1/5} t^{-3/5}, \tag{2.5}$$

where η_0 is the dimensionless constant, which for an ideal gas is $\sim$1.17.

As the remnant continues to expand and to decelerate, its post-shock temperature drops to $\sim 10^6$ K. At this point, ionized atoms start to capture free electrons and produce line emission. The forward shock accumulates a large amount of material, like a snow-plough amass snow. Hence, the third evolution stage of an SNR is called the *snow-plough* or *radiation phase*.

Finally, at the *dissipative stage*, the velocity of the forward shock becomes subsonic spelling the end of the SNR. The remnant falls apart, dissolving in the ISM.

2.2 Classification of SNRs

The historical classification of SNRs is based on their spectroscopical properties. Astronomers defined two classes of SNRs: Type I and Type II. The remnants of the first group do not feature any hydrogen lines in their optical spectrum, while for the second group the hydrogen lines are observed. Later, SNRs of Type I were split into subtypes, called Type Ia, Type Ib, and Type Ic, depending on the additional spectral characteristics: absence or presence of silicon and helium lines. Also, SNRs of Type II were divided into subtypes, labelled Type IIP, Type IIL, Type IIn, and Type IIb, according to the differences in their light curves.

Alternatively, one can classify SNRs into two basic types, which reflect the explosion mechanism of their progenitor stars. The first is the afore-mentioned Type Ia, which is believed to originate from the thermonuclear deflagration of a white dwarf. The explosion of a white dwarf occurs when its mass is close to the Chandrashekhar-mass limit $\sim 1.4 M_{\odot}$, with $M_{\odot}$ denoting one solar mass. The white dwarf can accumulate material via accretion of the mass of a binary companion or via merging another white dwarf. When the critical mass value is reached, the white dwarf becomes gravitationally unstable because the degeneracy pressure of its electrons does not suffice to compensate own gravitational force. The star implodes, which causes a rapid rise in temperature. This process activates fusion reactions of carbon and oxygen, which result in the thermonuclear explosion.

The type of an SNR reveals its typical characteristics, such as the mass of ejecta and the structure of the ambient medium. These properties consequently determine the dynamical evolution of an SNR. Due to Chandrashekhar-mass limit, the ejecta for Type Ia most likely comprises $\sim 1.4 M_{\odot}$. Furthermore, a white dwarf does not undergo any considerable mass

losses and thus has a negligible effect on the ambient ISM. Therefore, Type Ia SNR is usually assumed to expand in the ISM of a constant density.

The second group of SNRs, which includes all the historical types of SNR except of Type Ia, is believed to arise from the so-called core-collapse supernovae. As the name suggests, the explosion is provoked by the core collapse of a massive star, i.e., a star more massive than $8M_{\odot}$. Contrary to a white dwarf, a massive star can fabricate elements heavier than oxygen in its interior, ending up with a dense iron core. Because iron is a very stable element, the fusion and thus the energy release inside the star terminates. There is no more sufficient radiation pressure that can balance the gravity, and so the star starts to contract and its density increases. At some point, the critical nuclear density inside the core is reached, where the strong nuclear force becomes suddenly important. It bounces outwards, producing a shock wave, which expels the outer layers of the star.

Throughout its life, a massive star loses a significant amount of its mass in the form of stellar winds. This mass loss creates a wind-blown bubble bordered by a dense thin shell. Thus, for a core-collapse SNR, the forward shock expands within a modified medium instead of ISM. The interaction of the forward shock with this circumstellar medium can affect the acceleration of particles inside a core-collapse SNRs (Telezhinsky et al., 2013).

2.3 Particle acceleration

Enrico Fermi was the first who suggested that a crucial ingredient for particle acceleration in astrophysical plasmas is magnetic turbulence (Fermi, 1949). In the original Fermi approach, charged particles are scattered by randomly moving magnetic perturbations, referred by Fermi as magnetic mirrors. Both a particle and a magnetic mirror move in the reference frame of the observer with velocities v and u, respectively. A head-on collision leads to energy gain, while a head-off collision results in energy loss for a particle. As head-on collisions are statistically more numerous, interactions between charged particles and magnetic perturbations result in the energy gain rate of the order $(u/v)^2$. The scenario proposed by Fermi is nowadays known as the *second-order Fermi acceleration* mechanism or *stochastic acceleration*. Beyond the simple Fermi picture, where the turbulence is represented by randomly moving magnetic mirrors, one realizes that the exact type of turbulence is crucial for the acceleration process and hence resulting particle spectrum. Being a stochastic process, second-order Fermi acceleration can be represented by diffusion in momentum space.

A more efficient and widely accepted process to produce high-energy CR is the *diffusive shock acceleration* (DSA) theory, developed by Krymskii (1977), Axford et al. (1977), Blandford and Ostriker (1978) and Bell (1978a,b). It involves the presence of a strong shock wave with a sufficient amount of magnetic irregularities up- and downstream. In this scenario, particles are confined by small-amplitude plasma waves near the shock receiving energy by multiple crossing of the shock via back and forth scattering. As a consequence, these particles experience only head-on collisions when crossing the shock front. The fact that there are no head-off collisions makes the particle acceleration via DSA very efficient. It can be shown for DSA that a particle gains momentum $\delta p/p \sim (V_{\rm sh}/v)$ when crossing the shock front (e.g., Bell, 1978a). Therefore, it is also referred to as *first-*

order Fermi acceleration, in analogy to the second-order Fermi process. In contrast to stochastic acceleration, where the resulting form of the particle spectra depends on the turbulence type, DSA is almost insensitive to the microscopic conditions. The particle spectra generated by DSA is shaped as a power-law, where the corresponding spectral index is determined by the shock compression ratio. This fact, together with the high efficiency of DSA, makes it to the well-established theory for particle acceleration in astrophysical environments.

Stochastic acceleration plays a crucial role in the propagation of CR in interstellar environments (Strong and Moskalenko, 1998). In the presence of a shock, however, the efficiency of the second-order Fermi acceleration is perceived to be low compared to DSA. Nevertheless, it was realized that stochastic acceleration of particles can play an additional role in SNRs (Drury, 1983b). Also, some models involve only second-order Fermi acceleration to explain the entire emission from SNRs up to the TeV energy range (Liu et al., 2008). As it will be demonstrated in this thesis, second-order Fermi process can significantly affect the electron spectrum in SNRs and leave its imprint in the observed synchrotron flux.

In the following section, the so-called macroscopic approach to the DSA theory and stochastic acceleration is reviewed. As the name suggests, the macroscopic approach does not deal with individual particles but involves their phase space density and the related diffusion-convection equation instead. This approach is extremely useful when it comes to the description of long-lasting macroscopic objects, such as SNRs. Also, this work deals with solutions of the convection-diffusion equation, which in plasma and CR astrophysics is also known as *the transport equation for CR*.

2.3.1 Transport equation for cosmic rays

In the following theory, the electromagnetic fields are assumed to be given, and the behavior of particles is governed by those predefined electromagnetic fields. The fields that are potentially produced by the charged particles are neglected. Under these assumptions, the transport equation for CR originates from the Vlasov equation, which is based on the conservation of the phase space density, $f_d(\mathbf{r}, \mathbf{p}, t)$. For one sort of particles, the Vlasov equation reads

$$\frac{\partial f_d}{\partial t} + \mathbf{r}\frac{\partial f_d}{\partial \dot{\mathbf{r}}} + \mathbf{p}\frac{\partial f_d}{\partial \dot{\mathbf{p}}} = S(\mathbf{r}, \mathbf{p}, t)\,, \tag{2.6}$$

where $S(\mathbf{r}, \mathbf{p}, t)$ denotes a source term. The corresponding equations of motions are given by the Lorentz force. In a uniform magnetic field, B_0, the charged particles simply gyrate along the magnetic field lines. The corresponding gyroradius, which is also known as Larmor radius, in cgs-units[1] is given by

$$r_g = \frac{pc}{ZeB_0} \simeq (3 \cdot 10^4\,\mathrm{cm})\,\frac{1}{Z}\left(\frac{E}{\mathrm{TeV}}\right)\left(\frac{B_0}{10\,\mu\mathrm{G}}\right)^{-1}\,, \tag{2.7}$$

[1]Larmor radius in SI units is $r_g = \frac{p}{ZeB_0}$. In this work, however, cgs-units are used by default unless otherwise stated.

where Z is the total charge in units of the elementary charge constant, e, and E is the energy of the particle. The angle between the uniform magnetic field and the particles momentum, θ, which is known as pitch angle, remains constant. As the particles are tied to the uniform magnetic field lines, it is more convenient to refer to the guiding center than to their precise position when describing their dynamics.

Turbulence in the plasma reflected by the field distortion, $\delta\mathbf{B}$, changes the velocity direction of the particle when interacting with it. Thus, the particles motion diverts from the large-scale magnetic field lines, which consequentially modifies the pitch angle. If sufficient field disturbances are present, this process recurs, resulting in diffusive behavior in space, i.e., pitch-angle scattering.

It is common to divide the total electromagnetic fields into uniform and turbulent components

$$\mathbf{B}(\mathbf{r},t) = B_0\mathbf{e}_z + \delta\mathbf{B}(\mathbf{r},t)\,, \qquad \mathbf{E}(\mathbf{r},t) = \delta\mathbf{E}(\mathbf{r},t)\,. \tag{2.8}$$

The uniform magnetic field in this example is aligned with the z-axis and assumed to be significantly larger than the turbulent component, $B_0 \gg \delta B$. The large-scale electric field can be neglected due to the high conductivity of cosmic plasma. Furthermore, it is assumed that the ensemble-averaged fields are equal to the background fields, $\langle\mathbf{B}(\mathbf{r},t)\rangle = B_0$, $\langle\mathbf{E}(\mathbf{r},t)\rangle = 0$. It is important to stress that pure magnetic disturbances can only change the direction of the particles and hence induce spatial diffusion. For an energy transfer between waves and particles and hence diffusion in momentum space, a distinct electric component is needed.

Combining Equations 2.6 and 2.8 and assuming that the changes in the particle distribution induced by the field distortions are sufficiently small, the diffusion-convection equation, also known as the transport equation for CR, can be derived (e.g., Kirk et al. (1988), Dung and Petrosian (1994), Schlickeiser (2002); pp 293-312):

$$\frac{\partial f}{\partial t} = \frac{\partial}{\partial z}D_s\frac{\partial f}{\partial z} - \frac{\partial\,(uf)}{\partial z} + \frac{p}{3}\frac{du}{dz}\frac{\partial f}{\partial p} + \frac{1}{p^2}\frac{\partial}{\partial p}\left(p^4 D_p\frac{\partial f}{\partial p}\right) + Q\,. \tag{2.9}$$

Here $f(z,p,t)$ is the pitch-angle averaged distribution function of particles, p is the scalar momentum magnitude, and Q is the pitch-angle averaged source term. They can be introduced if the scattering time is shorter than the time scale of all other processes, and hence the distribution of particles is roughly isotropic in pitch angle. The first term on the right-hand side of Equation 2.9 determines the spatial diffusion of particles via spatial diffusion coefficient, D_s. The second and the third terms account for the spatial convection and spatial changes in the velocity of the plasma flow, u. A gradient of the local plasma velocity in Equation 2.9 leads to DSA. Equation 2.9 accounts for the second-order Fermi acceleration via the fourth term on the right-hand side. The momentum diffusion coefficient, D_p, contains the properties of the turbulence that is responsible for the stochastic acceleration. The spatial and the momentum diffusion coefficients are defined through the Fokker-Planck coefficients, $D_{\mu\mu}$, $D_{\mu p}$, and D_{pp}, as

$$D_s = \frac{v}{3}\lambda_{\rm mfp} = (v^2/8)\int_{-1}^{1} d\mu\, \frac{(1-\mu^2)^2}{D_{\mu\mu}(\mu)}\,, \tag{2.10}$$

$$D_p = 1/(2p^2)\int_{-1}^{1} d\mu\, \left(D_{pp}(\mu) - \frac{D_{\mu p}^2(\mu)}{D_{\mu\mu}(\mu)}\right)\,, \tag{2.11}$$

where μ is the cosine of the pitch angle. The mean free path of a particle, $\lambda_{\rm mfp}$, is the typical length that particles propagate between interactions. In general, the Fokker-Planck coefficients are determined by the electromagnetic fluctuations. Once derived, the coefficients describe the behavior of stochastic interactions between waves and particles. It is worth to note that the calculation of the Fokker-Planck coefficients for particular astrophysical environments is highly extensive (Yan and Lazarian, 2004, 2008; Shalchi, 2009).

Equation 2.9 cannot be solved analytically in its general form. Thus throughout this work, numerical solutions of Equation 2.9 are applied to model particular SNRs and their emissions.

2.3.2 Magnetohydrodynamic turbulence

The different modes of the magnetohydrodynamic (MHD) turbulence are obtained from the general MHD equations (presented in Appendix A). A class of waves, in which the restoring force is provided by the magnetic-field tension and no pressure or density fluctuations are carried, are called Alfvén waves. They propagate along the mean magnetic field lines with speed

$$v_{\rm A} = \frac{B_0}{\sqrt{4\pi\rho_0}}\,, \tag{2.12}$$

where ρ_0 is the density of the medium. The Alfvén waves have a prominent magnetic component, which is much larger than their electric field, as reflected by relation $|\delta B| = c/v_{\rm A}|\delta E|$. Therefore, the Alfvén waves can efficiently change the moving direction of a particle and are widely considered as the major agents for particle scattering around a shock wave and in astrophysical plasma in general. In the absence of a shock wave, particle acceleration by Alfvén waves is basically a classical second-order Fermi process.

Besides Alfvén waves, two other modes exist, called slow and fast-mode waves. The corresponding phase velocities resulting from the MHD equations in ideal plasma are given by

$$v_{\rm fm,sm} = \left[\frac{1}{2}\left\{c_s^2 + v_{\rm A}^2 \pm \sqrt{(c_s^2+v_{\rm A}^2)^2 - 4c_s^2 v_{\rm A}^2\cos^2\psi}\right\}\right]^{1/2}\,. \tag{2.13}$$

Here c_s is the speed of sound, and ψ is the angle between the wave-vector and the mean magnetic field orientation. Fast-mode waves are of particular relevance for this work, as will be discussed in the following sections. Unlike the Alfvén waves, the fast-mode waves feature a compressible magnetic-field component and their energy is partially carried by

kinetic fluctuations. The velocity of the fast-mode waves varies depending on the physical environment, as summarized in Figure 2.2. For highly magnetized plasmas and therefore $v_\mathrm{A} > c_s$, the speed of the fast-mode waves is close to the Alfvén velocity. In environments with high thermal pressure and low magnetic fields ($c_s > v_\mathrm{A}$), the speed is roughly equal to that of the sound wave.

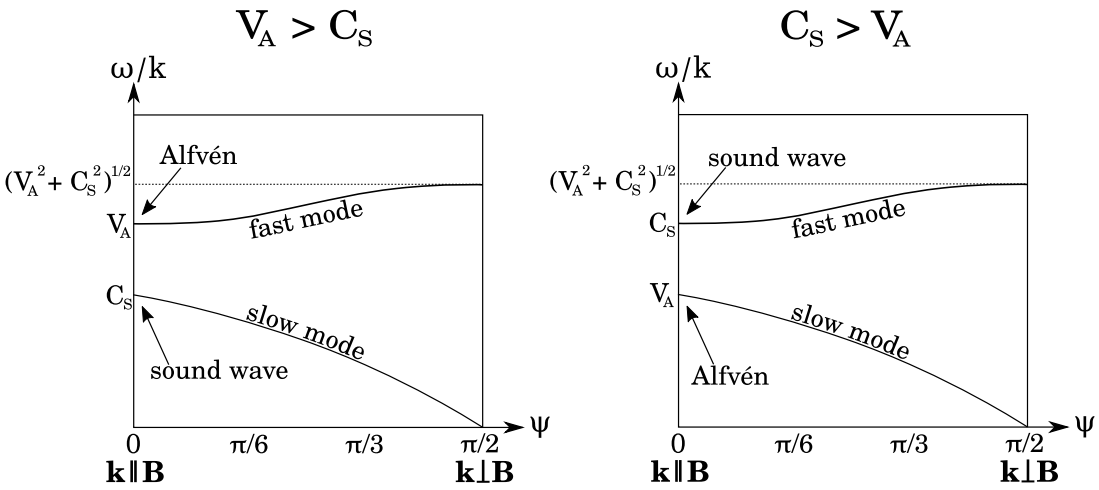

Figure 2.2: Dependence of phase velocity, ω/k, on propagation angle ψ for $v_\mathrm{A} > c_s$ (left) and $c_s > v_\mathrm{A}$ (right) enviroments.

In order for particles to interact with the MHD turbulence, their gyroradius has to be of the order of the wavelength. If the particle's gyroradius is significantly larger than the scale of the field irregularities, the particles do not feel the fine field structure and their trajectories follow the averaged field lines instead. In the opposite case, when the gyroradius is much smaller than the size of the magnetic fluctuations, the particles experience the turbulence just as a large-scale magnetic field. A resonant interaction is given by the gyroresonance condition

$$\omega - k_{||} v_{||} - n\Omega = 0 \quad \text{with} \quad n = \pm 1, 2, 3 \ldots , \tag{2.14}$$

where ω is the wave frequency, $k_{||}$ is the wavevector component parallel to the magnetic field, while $v_{||}$ is the component of a particle's velocity parallel to the magnetic field. Intuitively, Equation 2.14 means that in the rest frame of the particles guiding center, the Doppler-shifted wave frequency, $\omega - k_{||} v_{||}$, has to be the multiple of the particles gyrofrequency, $\Omega = eZB_0/mc$. In that case, the particle can resonantly interact with the wave and hence be scattered.

The peculiar case for $n = 0$, which does not depend on particles gyrofrequency, is called the transit-time damping (TTD). This interaction type is possible for the fast-mode waves due to their compressive magnetic field component. The name TTD comes from the fact that the resonance condition 2.14 for $n = 0$ can be expressed as $\lambda_{||}/v_{||} \approx T$, where $\lambda_{||} = 2\pi/k_{||}$ is the parallel wavelength component and $T = 2\pi/\omega$ is the wave

period. Therefore, for the TTD interaction the transit time of a particle across the wave compression has to match the wave period.

2.3.3 Diffusive shock acceleration

In the following section, a simplified approach to derive the particle distribution produced by DSA is presented. The transport equation for CR in steady state can be solved analytically for a plane-parallel shock. As depicted in Figure 2.3, in this configuration the plasma flow and magnetic flux are parallel, and both perpendicular to the shock normal.

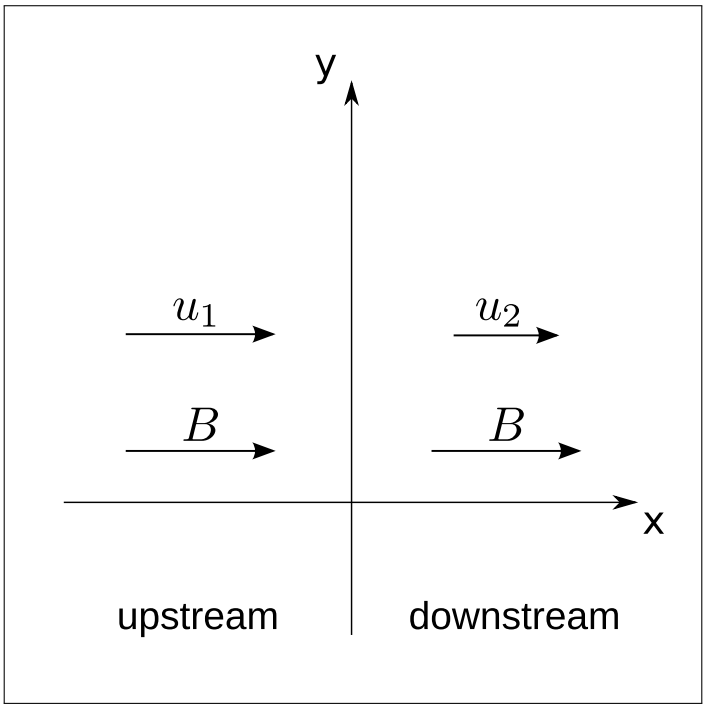

Figure 2.3: Schematic representation of a plane-parallel shock wave in its rest-frame. The plasma flow velocities are u_1 in upstream and u_2 in downstream regions, respectively.

In the shock-rest frame, Equation 2.9 that does not contain the second-order Fermi acceleration term simplifies to

$$\frac{\partial}{\partial x}\left(D_s(x,p)\frac{\partial}{\partial x}f(x,p)\right) - \frac{\partial}{\partial x}\left(u(x)f(x,p)\right) + \frac{p}{3}\frac{du(x)}{dx}\frac{\partial}{\partial p}f(x,p) + \frac{q_0}{p_{\rm inj}^2}\delta(p-p_{\rm inj})\delta(x) = 0\,. \tag{2.15}$$

The last term represents the injection of particles at the shock ($x = 0$) at the injection momentum $p_{\rm inj}$. Here and in the following, we use the thermal leakage injection model (Blasi et al., 2005), which we shall discuss in more detail in Section 4.4. In general, the thickness of the collisionless shock is roughly given by $u_1/\Omega_{\rm ci}$, where u_1 is the upstream plasma velocity in the shock-rest frame and $\Omega_{\rm ci}$ is the ion cyclotron frequency in the upstream

magnetic field (e.g., Leroy et al., 1982). In the scenario described by the thermal leakage injection model, a particle is injected when it perceives the shock wave as a sharp discontinuity. Thus, its Larmor radius must be larger than $u_1/\Omega_{\rm ci}$. The corresponding normalization factor q_0 of the source term scales in that scenario linearly with the plasma velocity, u_1, and density of the upstream region.

For simplicity, the spatial diffusion coefficient and the plasma flow velocities are assumed to be constant in the upstream and downstream regions but with a drastic jump at the shock position

$$D_s(x,p) = \begin{cases} D_1(p) & \text{for } x < 0 \\ D_2(p) & \text{for } x > 0 \end{cases} \qquad u(x) = \begin{cases} u_1 & \text{for } x < 0 \\ u_2 & \text{for } x > 0. \end{cases} \tag{2.16}$$

Obviously, under those assumptions the third and the fourth terms of Equation 2.15 disappear outside the shock. The general solution valid for $x \neq 0$ is therefore (e.g., Vladimirov (2009))

$$f(x,p) = \begin{cases} A(p)\exp\left(\frac{u_1 x}{D_1(p)}\right) + B(p) & \text{for } x < 0 \qquad \text{(upstream region)} \\ C(p)\exp\left(\frac{u_2 x}{D_2(p)}\right) + E(p) & \text{for } x > 0 \qquad \text{(downstream region).} \end{cases} \tag{2.17}$$

Additionally, the following trivial boundary and continuity conditions have to be fulfilled:

$$\lim_{x\to\infty} f(x,p) < \infty\,, \tag{2.18}$$

$$\lim_{x\to-\infty} f(x,p) = 0\,, \tag{2.19}$$

$$\lim_{x\to 0^-} f(x,p) = \lim_{x\to 0^+} f(x,p)\,. \tag{2.20}$$

Using the above conditions, one can find the three unknown functions in Equation 2.17. Equation 2.18 gives $C(p) = 0$ and Equation 2.19, which basically means that there are no external CR source, provides $B(p) = 0$. The third condition ensures that the upstream and downstream solutions match each other at $x = 0$, giving $f_0(p) \equiv A(p) = E(p)$. Summarizing, Equation 2.17 can be rewritten as

$$f(x,p) = \begin{cases} f_0(p)\exp\left(\frac{u_1 x}{D_1(p)}\right) & \text{for } x \leq 0 \qquad \text{(upstream region)} \\ f_0(p) & \text{for } x \geq 0 \qquad \text{(downstream region).} \end{cases} \tag{2.21}$$

Finally, in order to find the particle distribution function at the shock, $f_0(p)$, one can integrate Equation 2.15 around the shock position, $x = 0$, from $x = 0^-$ to $x = 0^+$, while

taking all terms into account. Hence Equation 2.15 gives

$$D_d(p)\frac{\partial f(x,p)}{\partial x}\bigg|_{x=0^+} - D_u(p)\frac{\partial f(x,p)}{\partial x}\bigg|_{x=0^-} + \frac{p}{3}\frac{df_0(p)}{dp}(u_2-u_1) + \frac{q_0}{p_{\rm inj}^2}\delta(p-p_{\rm inj}) = 0\,. \quad (2.22)$$

Note that the second term in Equation 2.15 cancels out when integrating due to conservation of mass. Inserting Equation 2.21 into 2.22 results into

$$\frac{p}{3}\frac{\partial f_0(p)}{\partial p}(u_2-u_1) - u_1 f_0(p) + \frac{q_0}{p_{\rm inj}^2}\delta(p-p_{\rm inj}) = 0\,. \quad (2.23)$$

The well-known solution of Equation 2.23 is found to be (e.g., Blasi et al. (2005))

$$\begin{aligned} f_0(p) &= \int_{p_0}^{p}\frac{d\bar{p}}{\bar{p}}\frac{3q_0}{p_{\rm inj}^2}\frac{\delta(\bar{p}-p_{\rm inj})}{(u_1-u_2)}\exp\left(-\int_{\bar{p}}^{p}\frac{dp'}{p'}\frac{3u_1}{(u_1-u_2)}\right) \\ &= \frac{3q_0}{p_{\rm inj}^3(u_1-u_2)}\exp\left(-\frac{3u_1}{(u_1-u_2)}\int_{p_{inj}}^{p}dp'\frac{1}{p'}\right) \\ &= \frac{3q_0}{p_{\rm inj}^3(u_1-u_2)}\left(\frac{p}{p_{\rm inj}}\right)^{-\frac{3u_1}{(u_1-u_2)}}\,. \end{aligned} \quad (2.24)$$

In summary, the final solution of the transport equation 2.15 is given by the expression 2.21, where the particle distribution function at shock is given by Equation 2.24.

To describe the collective particle behavior, the differential particle number density $N(\boldsymbol{r},p)$ is commonly used. It is defined and related to the distribution function as follows: the number of particles in an infinitesimal phase-space volume element $dV\,d^3p$ at $\boldsymbol{r}$, $\boldsymbol{p}$ is $d\mathcal{N} = f(\boldsymbol{r},\boldsymbol{p})dV\,d^3p$. The particle number density at a fixed momentum presented in the spherical coordinates is therefore

$$\frac{d\mathcal{N}}{dV} = f(\boldsymbol{r},\boldsymbol{p})p^2dp\,d\Omega\,. \quad (2.25)$$

Assuming isotropy in momenta, which is required for the transport equation for CR, the differential particle number density can be defined as

$$N(\boldsymbol{r},p) \equiv \frac{d\mathcal{N}}{dV\,dp} = 4\pi p^2 f(\boldsymbol{r},p). \quad (2.26)$$

With the above definition, the solution for the particle number density at the plane shock

reads as

$$N(x,p) = \begin{cases} \frac{12\pi q_0}{p_{\rm inj}(u_1-u_2)} \left(\frac{p}{p_{\rm inj}}\right)^{-s} \exp\left(\frac{u_1 x}{D_1(p)}\right) & \text{for } x \leq 0 \qquad \text{(upstream region)} \\ \frac{12\pi q_0}{p_{\rm inj}(u_1-u_2)} \left(\frac{p}{p_{\rm inj}}\right)^{-s} & \text{for } x \geq 0 \qquad \text{(downstream region)}, \end{cases} \tag{2.27}$$

where the power-law index is defined as $s \equiv (u_1+2u_2)/(u_1-u_2)$. This result demonstrates that the particle number density at the shock and the immediate downstream region is simply a power law in momentum. In the upstream region, the particle density decays exponentially with the distance. Applying this solution on SNR, it is useful to introduce the volume-integrated particle number densities for downstream and upstream regions of the remnant

$$N_d(p) \equiv \int_{V_d} N(\boldsymbol{r},p) dV = \frac{12\pi q_0 V_{\rm SNR}}{p_{\rm inj}(u_1-u_2)} \left(\frac{p}{p_{\rm inj}}\right)^{-s}, \tag{2.28}$$

$$\begin{aligned} N_u(p) \equiv \int_{V_u} N(\boldsymbol{r},p) dV &= \frac{12\pi q_0 A_{\rm SNR}}{p_{\rm inj}(u_1-u_2)} \left(\frac{p}{p_{\rm inj}}\right)^{-s} \int_{-\infty}^{0} \exp\left(\frac{u_1 x}{D_1(p)}\right) dx \\ &= \frac{12\pi q_0 A_{\rm SNR}}{p_{\rm inj}(u_1-u_2)u_1} D_1(p) \left(\frac{p}{p_{\rm inj}}\right)^{-s}. \end{aligned} \tag{2.29}$$

Here V_d and V_u are the volumes of the downstream and upstream regions, respectively, $V_{\rm SNR}$ is the total volume and $A_{\rm SNR}$ the surface of the SNR. Introducing shock compression ratio

$$r_{\rm sh} \equiv \frac{u_1}{u_2}, \tag{2.30}$$

one can rewrite the spectral particle index as

$$s = \frac{(r_{\rm sh}+2)}{(r_{\rm sh}-1)}. \tag{2.31}$$

Summarizing, DSA yields a simple power-law spectrum, where the spectral index is solely determined by the shock compression ratio. The compression ratio for the strong shocks, $r = 4$, provides the well-known DSA solution $N_d(p) \propto p^{-2}$.

2.3.4 Bohm diffusion

The particle distribution in the upstream region depends on the spatial diffusion coefficient, $D_1(p)$. A common choice for the DSA in astrophysical plasma is the Bohm-like diffusion. In this scenario, the magnetic turbulence scatters particles with gyroradii of

the same size as its wavelength, $\lambda \approx r_g$. As a particle interacts with a field irregularity, δB, its pitch angle changes by approximately $\delta\theta \approx \delta B/B_0$ per one wavelength. While a random scattering $\delta\theta^{-2}$ interactions are needed to modify the pitch angle by one radian. The mean free path of a particle that is randomly scattered can be then expressed as

$$\lambda_{\rm mfp} \approx r_g \left(\frac{B_0}{\delta B}\right)^2 . \tag{2.32}$$

With the above assumption, the general form for the spatial diffusion coefficient, in general, defined as $D_s \equiv (v/3)\lambda_{\rm mfp}$, can be rewritten for relativistic particles as

$$D_s(p) \simeq \frac{c}{3}\lambda_{\rm mfp} = \xi \frac{pc^2}{3ZeB_0} , \qquad \text{with} \qquad \xi = \left(\frac{B_0}{\delta B}\right)^2 . \tag{2.33}$$

The case with $\xi = 1$, which is known as the Bohm-limit, provides the most effective spatial diffusion. It is important to stress that the diffusion coefficient 2.33 can be formally derived for the Alfvén waves from Fokker-Planck coefficients via Equation 2.10 (e.g., Schlickeiser, 2002).

For the Bohm-like diffusion, the volume-integrated particle number density in the upstream region of the strong shock is

$$N_u(p) = \frac{16}{3}\frac{\pi \xi c^2 q_0 A_{\rm snr}}{V_{\rm sh}^2 ZeB_0}\left(\frac{p}{p_{\rm inj}}\right)^{-1} , \tag{2.34}$$

as can be seen from Equation 2.29. Thus, the total particle spectrum in the upstream region is harder than that of the downstream region.

2.4 Radiative processes

As it was pointed out in the introduction, interstellar magnetic fields induce multiple deflections of charged particles that propagate in our Galaxy. Thus it is not possible to track charged CR to the origin and to determine their factories directly. Instead, the researchers rely on the observations of photons that are produced in the CR interactions. The elementary processes that are relevant for SNRs are synchrotron radiation, bremsstrahlung, and inverse Compton (IC) scattering from electrons, as well as neutral-pion decay produced by high-energy protons. The four radiation processes are outlined in the following sections.

2.4.1 Synchrotron emission

In the presence of magnetic field, B, the electrons are forced to follow circular movement around a field line and to radiate their energy in the form of synchrotron emission, as shown in Figure 2.4.

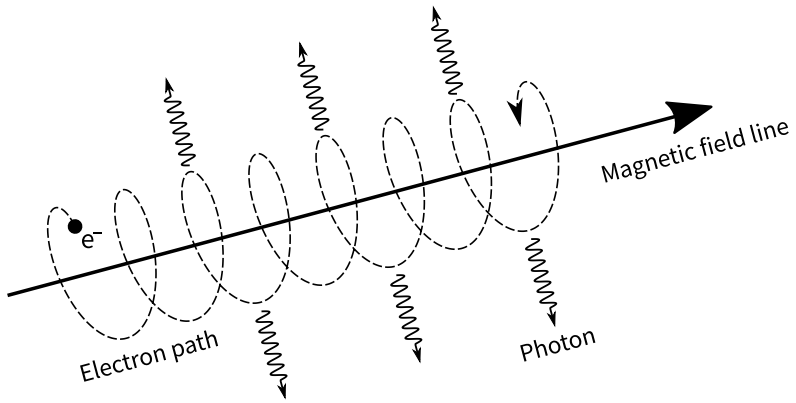

Figure 2.4: Synchrotron radiation of an electron.

An electron with Lorentz factor γ in a homogeneous magnetic field B produces a continuous spectral power (e.g., Crusius and Schlickeiser, 1986)

$$P_\nu = 1.8 \frac{\sqrt{3} e^3 B}{4\pi m_e c^2} \left(\frac{\nu}{\nu_0}\right)^{1/3} \exp\left(-\frac{\nu}{\nu_0}\right), \tag{2.35}$$

which peaks at characteristic photon frequency

$$\nu_0 = \frac{3e}{4\pi m_e c} B\gamma^2 . \tag{2.36}$$

The spectral power per electron is presented as dashed line in Figure 2.5. It rises with spectral index 1/3 and falls exponentially toward higher frequencies.

Integrating over an electron population, it can be shown that the electron number density $N_e(E) = N_0 E^{-s}$ generates a synchrotron spectrum shaped as a power law (e.g., Pacholczyk (1970))

$$\frac{dn_\gamma}{dE_\gamma dt dV} \approx 10^{-23} \left(\frac{4\pi}{h}\right) (8.31 \times 10^{-8})^{(s-1)/2} N_0 B^{(s+1)/2} E_\gamma^{-(1+s)/2} \quad \frac{\text{photons}}{\text{erg s cm}^3} . \tag{2.37}$$

It is important to note here that this calculation assumes by default a homogeneous magnetic field and hence a delta function for the probability distribution of local magnetic-field amplitudes. In radio astronomy, it is more convenient to use the emissivity function

in units erg cm^{-3}s^{-1}Hz^{-1} sr^{-1}, defined as

$$j_{sy} \equiv \left(\frac{4\pi}{hE_\gamma}\right)\left(\frac{dn_\gamma}{dE_\gamma dt dV}\right) \propto N_0 B^{(s+1)/2} E_\gamma^{-(s-1)/2}\,. \tag{2.38}$$

Throughout discussions in this work, the latter notation is used, and the spectral index of a synchrotron flux, S_ν, is defined as

$$\alpha = \frac{1-s}{2} \qquad \text{where} \qquad S_\nu \propto \nu^\alpha \propto E_\gamma^\alpha\,. \tag{2.39}$$

In the case of a turbulent magnetic field, care must be exercised to properly account for magnetic field fluctuations in calculating the synchrotron emissivity function. The magnetic-field amplitudes distribution is dispersed compared to the standard case, and its exact form is unknown. In the literature, one finds modified emissivities for exponential (Zirakashvili and Aharonian, 2010) and power-law (Kelner et al., 2013) distributions. Pohl et al. (2015) derived the synchrotron emissivity function for the Gaussian distribution of magnetic-field amplitudes, which is given by

$$P_{\rm eff} \simeq 1.8\frac{\sqrt{3}e^3 B_{\rm rms}}{4\pi m_e c^2}\sqrt{\frac{2}{\pi}}\left(\frac{\nu}{\nu_c}\right)^{1/3}\exp\left(-\frac{3}{2}\left(\frac{\nu}{\nu_c}\right)^{2/3}\right)\left(1+1.65\left(\frac{\nu}{\nu_c}\right)^{0.42}\right)^{0.53}\,. \tag{2.40}$$

Here $\nu_c \equiv \nu_0(B_{\rm rms})$ denotes the characteristic frequency for a root mean square of the distribution $B_{\rm rms}$. A comparison of the standard emissivity function with that derived in Pohl et al. (2015) is presented in Figure 2.5. The modified function (solid line) is smeared compared to the standard one (dashed line). Featuring the same slope below ν_c, the modified emissivity shows a harder cutoff at higher frequencies than the standard expression. Throughout this work, the modified function from Pohl et al. (2015) is used for modeling of SNRs.

Synchrotron emission in SNRs is firmly confirmed by observations in the radio range (Green, 2009; Urošević, 2014). Furthermore, measurements of nonthermal X-rays from the limbs of young SNRs (Koyama et al., 1995; Hughes et al., 2000; Gotthelf et al., 2001; Hwang et al., 2002) are conventionally interpreted as synchrotron emission from electrons in TeV-ranges. The observed radio spectra from individual SNRs reflect the spectral index of the nonthermal electron distributions below the cutoff, which can be deduced via Equation 2.39. Measurements in the X-ray range typically indicate the presence of a cutoff in the synchrotron flux, which may be attributed to a cutoff in the parent electron spectra.

The synchrotron emission is a significant loss mechanism for electrons in the TeV-energy range. The corresponding loss-time scale that reflects the time in which a particle

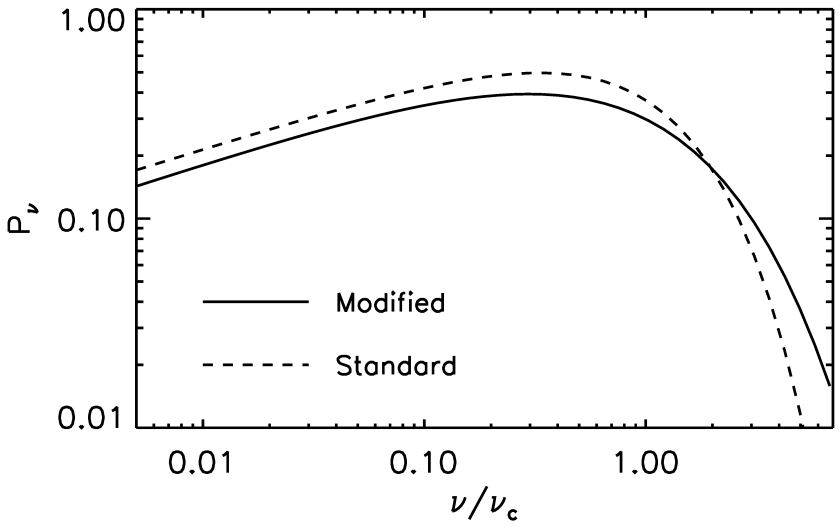

Figure 2.5: Standard expression for the spectral synchrotron power (dashed line) versus the synchrotron emissivity for turbulent magnetic field with Gaussian distribution (solid line). Figure is taken from Pohl et al. (2015).

release half of its energy, is given by

$$\tau_{\rm loss} \equiv E/\dot{E} \simeq 130\,{\rm yr}\,\left(\frac{B}{100\,\mu{\rm G}}\right)^{-2}\left(\frac{E}{10\,{\rm TeV}}\right)^{-1}\,. \tag{2.41}$$

Hence, it is important to include the synchrotron losses when modeling the electron acceleration at shocks of SNRs.

2.4.2 Thermal and nonthermal bremsstrahlung

Besides the synchrotron emission, electrons can produce X-ray and γ-ray photons via bremsstrahlung mechanism. In general, bremsstrahlung occurs due to the deceleration of electrons in the electric Coulomb fields of a nuclei, as schematically depicted in Figure 2.6. A distinction is made between "thermal" and "nonthermal bremsstrahlung", which are, however, basically the same process. The terms "thermal" and "nonthermal" refer to the electron population involved in radiation. Hence, the nonrelativistic electrons in thermal equilibrium with temperature T_e emit X-ray continuum, where the energy emissivity per unit energy interval can be approximated for the photon energy above 0.1 keV with (Hnatyk and Petruk, 1999)

$$P_c(T_e,\epsilon) = 1.652\cdot 10^{-23} n_e^2 G_c T_6^{-\frac{1}{2}} \exp\left(\frac{-11.59\epsilon}{T_6}\right)\quad \frac{\rm erg}{\rm keV\ s\ cm^3}\,. \tag{2.42}$$

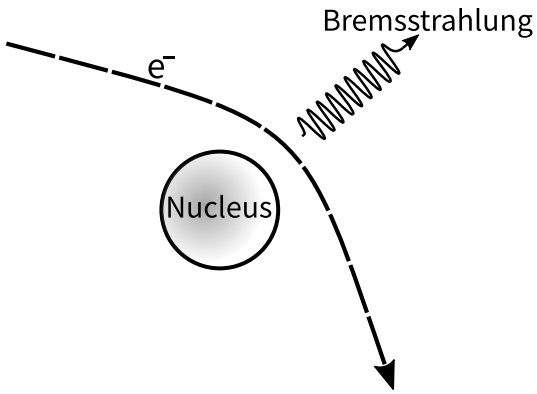

Figure 2.6: Bremsstrahlung process.

Here T_6 is the temperature in 10^6 K, n_e is the electron number density, and ϵ is the photon energy in keV. The corresponding factor G_c is estimated to be

$$G_c(T_e, \epsilon) = 27.83(T_6 + 0.65)^{-1.33} + 0.35\epsilon^{-0.34} T_6^{0.422} \,. \tag{2.43}$$

Nonthermal electrons produce γ-ray flux, which is referred to as nonthermal bremsstrahlung (NTB). This emission has the same spectral index $\Gamma \approx s$ as the corresponding electron spectrum, $N_e \propto E^{-s}$. Roughly, the photon flux from the electron number density N_e can be approximated with (Gaisser et al., 1998)

$$\frac{dn_\gamma}{dE_\gamma dt dV} \simeq 7 \cdot 10^{-16} n_{\rm H} N_e \quad \frac{\text{photons}}{\text{erg s cm}^3} \,, \tag{2.44}$$

where $n_{\rm H}$ is the hydrogen number density.

2.4.3 Inverse-Compton Scattering

Another mechanism to produce γ-ray photons is the IC scattering. In this process, the ultra-relativistic electrons transfer their energy to low-energy photons, as schematically depicted in Figure 2.7. If the initial energy of the photon, $E_{\gamma i}$, is far less than the electrons rest energy in the particles rest-frame, $m_e c^2$, the interaction occurs with the Thomson cross section

$$\sigma_T \equiv \frac{8\pi r_e^2}{3} \approx 6.65 \times 10^{-25}\,\text{cm}^2 \,. \tag{2.45}$$

Here $r_e = 2.82 \times 10^{-13}\,\text{cm}$ is the classical electron radius. The corresponding condition allowing for this case, which is called Thomson regime, can be expressed via parameter

$$\Gamma_{kn} \equiv 4\gamma E_{\gamma i}/m_e c^2 \ll 1 \,, \tag{2.46}$$

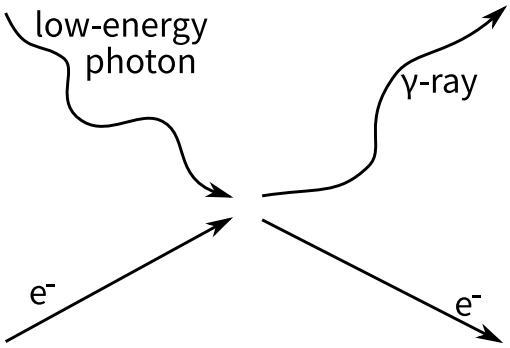

Figure 2.7: Schematic representation of IC scattering.

where γ is the Lorentz factor of the electron, defined as $\gamma \equiv (1 - v^2/c^2)^{-\frac{1}{2}}$. Beyond condition 2.46, the IC scattering takes place with Klein-Nishina cross section (Klein and Nishina, 1929), which decreases with higher photon energies.

A useful approximation for the energy of a scattered photon in laboratory frame for the so-called Thomson and Klein-Nishina regimes is

$$E'_\gamma \simeq \begin{cases} \gamma^2 E'_i & \text{for} \quad E'_i \ll m_e c^2/\gamma \quad \text{(Thomson regime)} \\ \frac{1}{2}\gamma m_e c^2 & \text{for} \quad E'_i \gg m_e c^2/\gamma \quad \text{(Klein-Nishina regime)}\,, \end{cases} \tag{2.47}$$

where E'_i is initial photon energy in laboratory frame.

The general result for an upscattered uniform photon distribution per electron with energy $\gamma m_e c^2$ is (Jones, 1968; Blumenthal and Gould, 1970)

$$\frac{dn_\gamma}{dE_\gamma dt} = \frac{3}{4}\frac{\sigma_T c}{\gamma^2}\frac{m_e c^2}{E_{\gamma i}}\frac{dn_\gamma(E_{\gamma i})}{dV}\,dE_{\gamma i}\left[2q\ln q + (1+2q)(1-q) + \frac{\Gamma_{kn}^2 q^2(1-q)}{2(1+\Gamma_{kn}q)}\right]. \tag{2.48}$$

Here E_γ is the energy of the outgoing photon, $dn_\gamma(E_{\gamma i})/dV$ is the distribution of the seed photon field and

$$q \equiv \frac{E_\gamma}{\Gamma_{kn}(\gamma m_e c^2 - E_\gamma)}\,. \tag{2.49}$$

The seed photon field for the IC scattering in SNRs can be naturally provided by the CMB or by the infra-red (IR) emission. IC emission from CMB can be well estimated within Thomson regime. In contrast, the more energetic IR photon requires Klein-Nishina regime for the calculation of IC emission.

The photon distribution of CMB is described via black-body radiation

$$\frac{dn_\gamma(E_{\gamma i})}{dV} = \frac{1}{\pi^2(\hbar c)^3}\frac{E_{\gamma i}^2}{\exp(E_{\gamma i}/k_B T) - 1}\,, \tag{2.50}$$

where k_B is the Boltzmann constant, $\hbar$ is the reduced Planck's constant, and T is the

temperature measured for CMB to be approximately 2.73 K. Thermal emission of the form of Equation 2.50 but deviant normalization is usually referred to as gray-body radiation.

The total emission from an electron population is obtained by integration of expression 2.48 over the entire particle distribution. For an energy distribution shaped as a power law, $N(E) \propto E^{-s}$, and the photon seed provided by CMB, the resulting photon spectrum below the cutoff scales as

$$\frac{dn_\gamma}{dE_\gamma dt dV} \propto E_\gamma^{-(1+s)/2} \,. \tag{2.51}$$

Thus, an electron population produces the same slopes for the synchrotron emission and γ-ray spectra via IC scattering on CMB photons (cf. Equation 2.37).

2.4.4 Pion decay

High-energy protons can produce γ-ray emission when colliding with a nucleus at rest from the ambient medium or dense gas clouds. The inelastic hadron-hadron interaction creates a π-mesons, where the one-third consist of the neutral pion, π^0. The neutral pion with the rest mass $m_\pi \approx 136$ MeV is unstable and decays into two γ-ray photons

$$\pi^0 \rightarrow \gamma + \gamma \,. \tag{2.52}$$

The resulting photon spectrum is symmetric around $m_\pi/2 \approx 68$ MeV. The total photon flux is a superposition of these individual pion-produced γ-ray spectra. It can be roughly estimated from the proton spectra N_p as (Gaisser et al., 1998)

$$\frac{dn_\gamma}{dE_\gamma dt dV} \simeq 10^{-16} n_{\mathrm{H}} N_p \quad \frac{\text{photons}}{\text{erg s cm}^3} \,. \tag{2.53}$$

The threshold energy for this process is roughly ~ 0.28 GeV. A proton in the TeV-energy range transfers approximately 10% of its energy to a produced γ-particle. A pion bump cuts off below 70 MeV and features the same spectral index as the primary proton number density.

In general, it is challenging to distinguish between leptonic and hadronic γ-ray emissions in SNRs, since the corresponding fluxes are observed in the same energy range from 70 MeV to TeV. Mostly, particular modeling of SNRs allows for both leptonic and hadronic scenarios. Nevertheless, certain constraints can be achieved by means of global modeling that includes the entire available multi-wavelength spectrum of the SNR. Furthermore, the shapes of hadronic and leptonic flux contributions are essentially different. Provided a comprehensive data set with a sufficiently small error bars, the slope and the curvature of the spectrum can indicate its production mechanism. Therefore, extended γ-ray observations that can exhibit a particular shape of the spectra are needed. Acker-

mann et al. (2013) detected for the first time characteristic hadronic spectra and hence confirmed proton acceleration in two SNRs, IC443 and W441.

2.4.5 Filaments

High-resolution X-ray observations reveal that the nonthermal emission of shell-type SNRs posses a filament structure (e.g., Koyama et al., 1995; Hughes et al., 2000; Gotthelf et al., 2001; Hwang et al., 2002; Bamba et al., 2005; Parizot et al., 2006). The bright emission in the X-ray energy range peaks in the immediate vicinity of the forward shock of an SNR and falls toward its interior. A common explanation for the drastic decrease of the photon flux inside the remnant are the significant energy losses for the high-energy electrons. The electrons inevitably experience synchrotron losses due to high magnetic fields while propagating in the downstream region. The observed thin structures reflect then the corresponding electron energy distributions.

To describe the above situation again, the transport equation for CR (Equation 2.9) can be used. The synchrotron losses can be included via catastrophic loss term, $f(x,p)/\tau_{\rm loss}$, where $\tau_{\rm loss}$ is the synchrotron loss time scale. Transport equation for the downstream region ($x > 0$) that includes spatial diffusion and advection reads then

$$D_2 \frac{\partial^2 f(x,p)}{\partial x^2} - u_2 \frac{\partial f(x,p)}{\partial x} - \frac{f(x,p)}{\tau_{\rm loss}} = 0\,. \tag{2.54}$$

The general solution of Equation 2.54 is

$$f(x,p) \propto \exp\left(\frac{-x}{l_{\rm loss}}\right)\,. \tag{2.55}$$

It demonstrates that the particle distribution drops exponentially with a typical length scale given by

$$l_{\rm loss} = \frac{2D_2/u_2}{\sqrt{1 + 4D_2/(u_2^2\tau_{\rm loss})} - 1}\,. \tag{2.56}$$

It is important to distinguish two limits: the advection-dominated and the diffusion-dominated propagation. The advection-dominated case is valid for the relatively low-energy particles, which transport is governed by advection. In this case, the corresponding propagation length simplifies to

$$l_{\rm adv} \approx u_2 \tau_{\rm loss}\,. \tag{2.57}$$

For the diffusion-dominated propagation, which applies to the higher energy electrons, the length scale is approximately given by

$$l_{\rm diff} \approx \sqrt{D_2 \tau_{\rm loss}}\,. \tag{2.58}$$

An alternative explanation for the bright synchrotron rims observed at SNRs is the

magnetic-field damping (Pohl et al., 2005). The basic idea is that the thin structures reflect the magnetic-field profile. The magnetic-field strength, which co-determines the synchrotron production falls toward the interior of the remnant, giving rise to the exponentially decreasing luminosity distribution. The advantage of the magnetic-field damping scenario is that in contrast to the previous interpretation, it is additionally able to explain the filaments in the radio range. In Chapter 6, we focus on both potential scenarios when modeling a particular remnant, the Tycho's SNR.

2.5 Beyond the standard model

2.5.1 Alvénic drift

Despite the huge success of the DSA theory, many SNRs show radio spectral indices, α, that vary between -0.2 and -0.8 Green (2009). This clearly deviates from the canonical solution -0.5 provided for the strong shocks by the standard DSA and indicates that the electron spectrum produced in SNRs can be softer or harder than p^{-2}. An example, which will be discussed in detail in Chapter 6, is the young historical SNR Tycho with $\alpha \approx -0.65$ (Kothes et al., 2006).

A popular explanation for the observed soft spectra ($|\alpha| > 0.5$) is a phenomenon called Alfvénic drift (Bell, 1978b). In this picture, scattering centers moving with Alfvénic velocity relative to the background plasma are assumed. The relative direction of the propagation of the Alfvén waves is reflected by the cross helicity, $H_c = \pm 1$. Thus the effective compression ratio seen by particles is

$$r_{\rm eff} = \frac{u_1 + H_{c1} v_{\rm A1}}{u_2 + H_{c2} v_{\rm A2}}\,, \tag{2.59}$$

where u_1, H_{c1}, $v_{\rm A1}$ are the plasma velocity, the helicity, and the Alfvén velocity in the upstream and u_2, H_{c2}, $v_{\rm A2}$ in the downstream regions, respectively.

Several global models for SNRs involve this concept (Morlino and Caprioli, 2012; Jiang et al., 2013; Slane et al., 2014). Usually, the helicities $H_{c1} = -1$ and $H_{c2} = 0$ are assumed, which corresponds to the situation shown in Figure 2.8. In the downstream region, the velocity of the scattering centers equals the plasma velocity, $u_2 = u_1/r_{\rm sh} = V_{\rm sh}/r_{\rm sh}$. In the upstream region, where the Alvénic drift is present, the Alfvén waves propagate predominantly opposite to the plasma flow, and the effective velocity of the scattering centers is $u_1' = u_1 - v_{\rm A}$. As a result, the corresponding effective compression ratio is reduced compared with the classical case:

$$r_{\rm eff} = \frac{u_1 - v_{\rm A1}}{u_2} = r_{\rm sh} \frac{V_{\rm sh} - v_{\rm A1}}{V_{\rm sh}}\,. \tag{2.60}$$

Consequentially, the particle spectrum with power-law index $s = (r_{\rm eff} + 2)/(r_{\rm eff} - 1)$ becomes softer. This effect is more pronounced with higher magnetic field since the

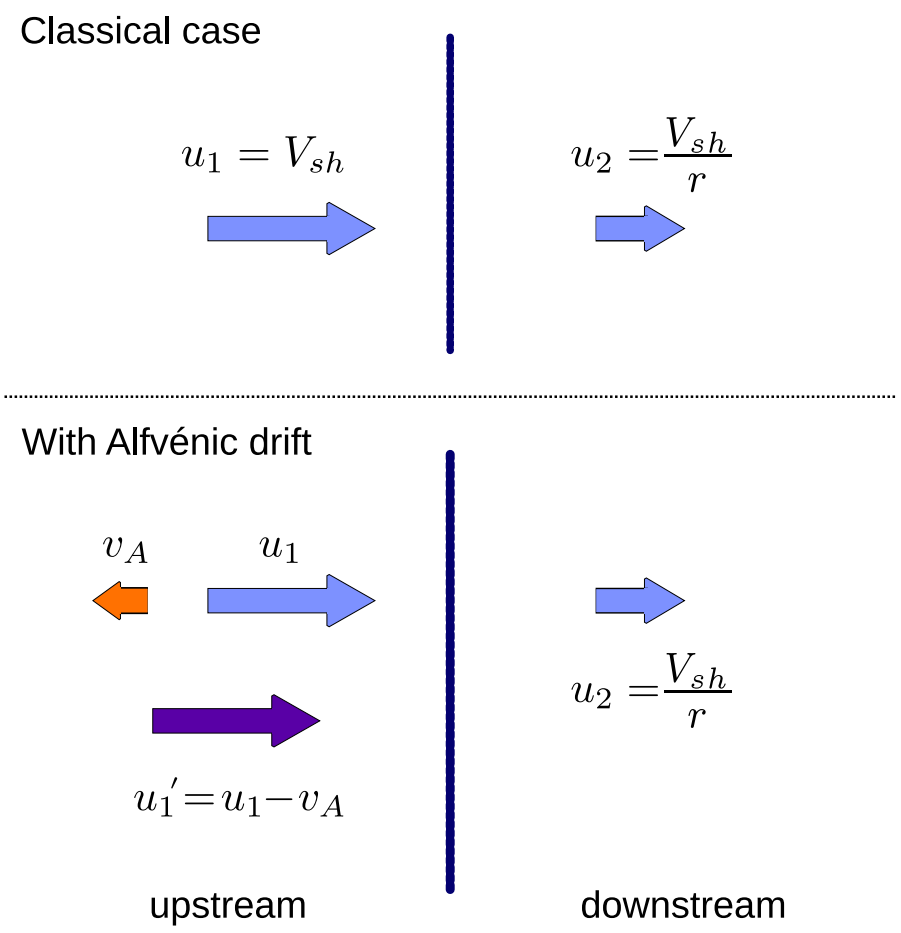

Figure 2.8: Velocities of the scattering centers in the shocks restframe without (upper drawing) and with (bottom drawing) Alvénic drift.

Alfvén velocity scales with the overall magnetic-field strength.

Despite its convenience and simplicity, the Alvénic drift concept has certain discrepancies. We demonstrate them in Chapter 6, where we focus on global modeling of Tycho's SNR.

2.5.2 Nonlinear DSA

The previously described DSA approach is valid for the test-particle approximation, which requires that the dynamical CR feedback on the shock structure is negligible. This assumption is justified as long as the CR pressure stays below 10% of the shock ram pressure (Kang and Ryu, 2010). Nevertheless, the ion to electron ratio, ∼70, measured around 10 GeV, implies that numerous SNRs convert about 10% of their energy into particle acceleration (Gaisser, 1990). In that case, when the dynamic effect from the high-energy particles becomes important, it modifies the shock structure and, consequently, the particle spectrum (Drury and Völk, 1981; Malkov and Drury, 2001).

To simply estimate the total change of the plasma velocity, δu, induced by the CR pressure, $P_{\rm cr}$, one can use the general equation of motion in fluids. The force, $\boldsymbol{F}$, in a certain volume of a fluid, V, is given by the pressure gradient:

$$\frac{\boldsymbol{F}}{V} = -\nabla \boldsymbol{P}\,. \tag{2.61}$$

For the one-dimensional case of the planar shock in its rest-frame with the pressure provided by CR, Equation 2.61 reduces to

$$\rho \frac{du}{dt} = -\frac{\partial P_{\rm cr}}{\partial x}\,, \tag{2.62}$$

where ρ is the background plasma density. Transforming the variable $dt = dx/u$, one obtains for the relative velocity change in a region $[x_2 : x_1]$

$$\frac{\delta u}{u} = -\frac{1}{u^2\rho}\int_{x_1}^{x_2} dx \frac{\partial P_{\rm cr}(r)}{\partial x} = \frac{P_{\rm cr}(x_1) - P_{\rm cr}(x_2)}{u^2\rho} \equiv \frac{\delta P_{\rm cr}}{u^2\rho}\,. \tag{2.63}$$

This expression demonstrates that the relative-velocity change, $\delta u/u$, is equal to the ratio of the CR to the flow pressures. Thus, following Kang and Ryu (2010), in the case of a test-particle limit, the relative plasma velocity change should not exceed the value 0.1. If this condition is violated, the back-reaction of the accelerated CR on the shock dynamics cannot be neglected, and hence the standard DSA approach is no longer valid. Instead, an extended theory, called the nonlinear DSA (NLDSA) (e.g., Drury, 1983a; Berezhko and Ellison, 1999; Blasi, 2002b,a), is required. In the following, a rough idea behind NLDSA is presented.

Figure 2.9(a) illustrates the differences between the modified and unmodified shocks. The blue dashed line represents the plasma velocity of a shock for the classical DSA, and the red solid line displays a shock significantly affected by the CR pressure. In simple terms, in the classical case, the shock wave features a drastic velocity jump, which is sufficiently characterized by the shock compression ratio $r_{\rm sh} = u_1/u_2$. However, if enough CR are present, the velocity profile shows a slightly complicated structure. The CR streaming forms a density and velocity gradient ahead of the shock front, called a dynamic precursor. The velocity in the immediate upstream region, u_1, is decreased compared to that of the classical case. Conversely, the plasma velocity in the far upstream, u_0, is larger than the upstream velocity for unmodified shock. Thus, the modified shock profile can be described in terms of two quantities: the subshock compression ratio, $R_{\rm sub} \equiv u_1/u_2$, and the total compression ratio, $R_{\rm tot} \equiv u_0/u_2$, where the following condition is fullfilled: $R_{\rm sub} < r_{\rm sh} < R_{\rm tot}$.

As the high-energy particles have larger gyroradii (cf. Equation 2.32), they rather see the larger compression ratio, $R_{\rm tot}$. On the opposite, the low-energy particles reside in the vicinity of the shock front, experience the thermal subshock and hence the smaller compression ratio, $R_{\rm sub}$. As a result, the particle spectra produced at the modified shock yield a concave shape: they are softer at lower and harder at higher energies, as can

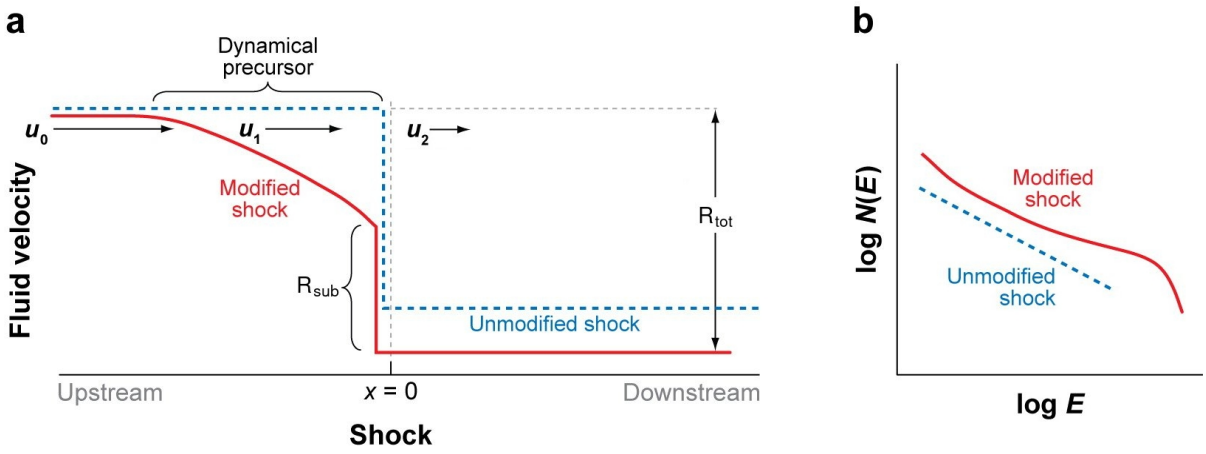

Figure 2.9: (a) Comparison between CR-modified (red solid line) and unmodified (blue dashed line) shock velocity profiles. (b) The corresponding particle spectra, produced at CR-modified (red solid line) and unmodified (blue dashed line) shocks. Figure adapted from Reynolds (2008).

be seen from Equation 2.31. The schematic comparison between particle spectra for the standard and nonlinear DSA is shown in Figure 2.9(b). While the particle spectrum from the unmodified shock (blue dashed line) is shaped as a simple power-law, the spectrum produced at the modified shock (red solid line) features a distinct curvature. The stronger the dynamical CR feedback on the shock, the more pronounced is the concave curvature in the particle spectrum.

Parts of this chapter have been published in
Pohl et al. 2015, A&A 574, A43
(See table of publications)

Chapter 3

Stochastic re-acceleration in SNRs

The content of this chapter has been published in Pohl et al. (2015). The paper presents analytic calculations performed by my supervisor Prof. Dr. Martin Pohl. Additionally, Pohl et al. (2015) presents a simple generic model for stochastic re-acceleration of electrons in SNRs. The corresponding particle spectra and synchrotron emissions are computed by the author of this thesis and hence described in the following sections.

3.1 Introduction

As mentioned before, radio spectral indices of SNRs are expected to reflect the electron spectra in the GeV-energy range. The standard DSA for the strong shocks predicts $N(p) \propto p^{-2}$ and, therefore, a synchrotron flux, $S \propto \nu^{\alpha}$, with $\alpha = -0.5$. However, the radio observations of ∼270 SNRs reveal a dispersion around $\alpha = -0.5$. The corresponding measurements show flatter and steeper slopes with indices varying between -0.2 and -0.8 (Green, 2009). The synchrotron losses for electrons become significant at TeV-scale and thus are not able to explain the observed discrepancies.

As described in Section 2.5.2, a slight softening can occur due to feedback of CR on the shock structure of the remnant (e.g., Blandford and Eichler (1987)). Another common explanation involves the Alfvénic drift, which can modify the effective shock compression ratio seen by particles (see Section 2.5.1). However, Vainio and Schlickeiser (1999) explicitly calculated the transmission coefficients for Alfvén waves and showed that their presence can harden the particle and, consequentially, the synchrotron spectra. Thus, the results of Vainio and Schlickeiser (1999) imply that the presence of Alfvénic drift fails to account for the observed softening in the radio range[1]. An alternative scenario for the soft radio spectra is therefore of great interest.

Drury (1983b) suggested that second-order Fermi acceleration can impact the particle spectra in SNRs besides the DSA. In fact, there are several mechanisms that can generate various types of turbulence in SNRs. For example, instabilities are expected to evolve in the downstream region due to shock rippling (Giacalone and Jokipii, 2007; Fraschetti, 2013). Obviously, the type of turbulence plays an essential role in the acceleration process.

[1]Findings of Vainio and Schlickeiser (1999) are at odds with the claims of Morlino and Caprioli (2012) and Slane et al. (2014), which we shall discuss in Chapter 6.

The nonresonant streaming instability, for example, posses a negligible phase velocity in the shock's rest-frame (Bell, 2004). Thus it can account for the spatial diffusion of particles, but not for the diffusion in momentum space or Alfvénic drift. In contrast, the turbulence generated by nonresonant small-scale instabilities operating in the upstream in the nonlinear phase can promote stochastic acceleration (Stroman et al., 2009). The Alfvén waves are able to transfer energy to particles, as they possess an electric component. The Alfvén speed depends on magnetic-field strength though, which is typically small inside SNRs. Since the corresponding momentum-diffusion coefficient is likewise small, stochastic acceleration by Alfvén waves is rather insignificant. An eligible turbulence mode for stochastic acceleration of electrons inside SNRs are the fast-mode waves. As discussed in Section 2.3.2, in weakly amplified magnetic media, the phase velocity of the fast-mode waves is approximately given by the speed of sound. In the downstream region of SNRs, the sound speed typically yields a significant value of the order of $\sim 1000\,\mathrm{km/s}$.

Pohl et al. (2015) examined three different types of turbulence that can be expected in the immediate downstream region of an SNR: fast-mode waves, small-scale nonresonant modes, and large-scale MHD turbulence. The corresponding momentum diffusion coefficients typical for the post-shock environment of SNRs are explicitly derived in this work. Pohl et al. (2015) concludes that fast-mode waves are the only type of waves among these that can be significant in SNRs as their acceleration time, τ_{acc}, is of the order of few years.

In the following sections, a generic model that is based on the idea of efficient stochastic re-acceleration of electrons by the fast-mode waves in the immediate downstream region of SNRs is presented.

3.2 Model assumptions

To investigate the impact of stochastic re-acceleration in SNRs, a generic 1D model is used. Its schematic structure is depicted in Figure 3.1. We assume that in a thin region behind the forward shock, a turbulent region (marked as yellow area) is built. Stochastic acceleration is an important damping process of fast-mode waves (cf. Thornbury and Drury, 2014), and so it is efficient only in a thin region behind the forward shock with the thickness, L_{fm}, which is assumed to be fixed for now. We consider electrons that escape from the shock to the downstream region. Their radial propagation path toward the SNR center, as shown in Figure 3.1, is denoted as y.

As we are primarily interested in electrons that are responsible for the radio emission observed from SNRs, we can neglect the very-high energy particles. Characteristic photon energy emitted by an electron gyrating in magnetic field, B, is given by

$$E_{\mathrm{sy}} \simeq 1.8\,\mathrm{eV} \left(\frac{B}{100\,\mu\mathrm{G}}\right) \left(\frac{E}{\mathrm{TeV}}\right)^2 . \tag{3.1}$$

Usually, the typical magnetic fields in SNRs are of the order of $\sim 100\,\mu$G. As can be seen from Equation 3.1, for magnetic field this strong the radio flux, emitted at roughly $\sim 10^{-6}$ eV, is generated by the electrons in the GeV-energy range. Thus, in our case we may primarily focus on electrons around the GeV-energy range. As mentioned in Section 2.4.5, the particles in cosmic plasma are transported via advection and diffusion

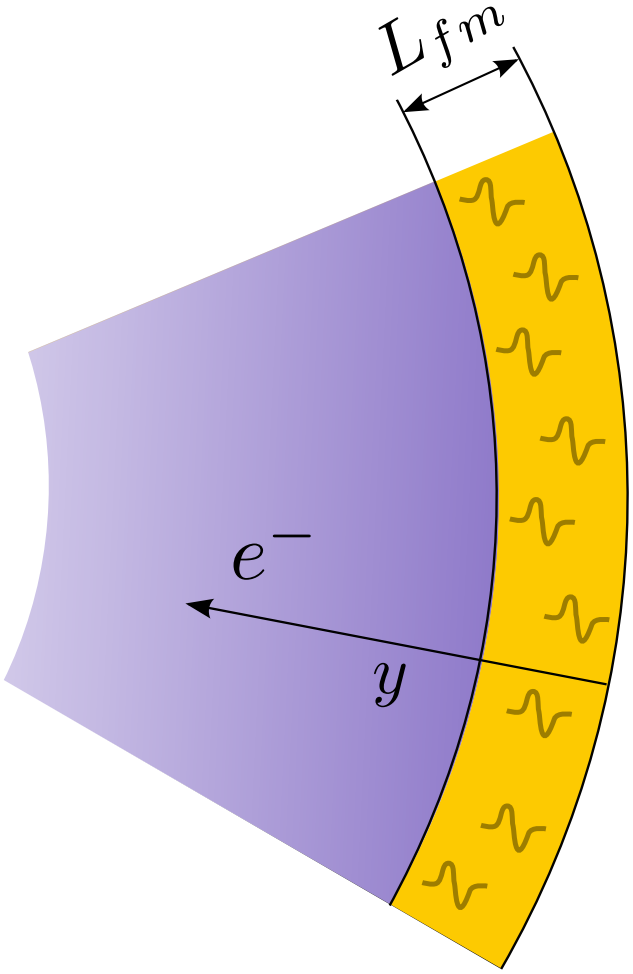

Figure 3.1: Schematic structure of the generic model for stochastic re-acceleration in the immediate post-shock region of an SNRs. The fast-mode waves efficiently operate in the area of the thickness $L_{\rm fm}$, which is marked yellow. In contrast, the far-downstream region of an SNR is shaded blue.

processes. The advective length of a particle is energy-independent and scales with the time period Δt as

$$l_{\rm adv} \simeq v_{\rm adv}\Delta t \simeq 3 \times 10^{15}\,{\rm cm} \left(\frac{v_{\rm adv}}{1000\,{\rm km/s}}\right)\left(\frac{\Delta t}{\rm yr}\right) . \tag{3.2}$$

Here $v_{\rm adv}$ is the advective velocity, which typical value in the post-shock region of an SNR is of the order of $\sim 1000\,{\rm km/s}$. The diffusion length is determined by the spatial diffusion

coefficient, D_s, which we assume to be Bohm-like. According to Equation 2.33, the diffusion length for an electron of the energy E in magnetic field B is (cf. Equation 2.58)

$$\begin{aligned} l_{\rm diff} &\simeq \sqrt{D_s(E)\Delta t} \\ &\simeq (10^{14}\,{\rm cm})\,\xi^{1/2}\left(\frac{E}{\rm GeV}\right)^{1/2}\left(\frac{B}{100\,\mu{\rm G}}\right)^{-1/2}\left(\frac{\Delta t}{\rm yr}\right)^{1/2}. \end{aligned} \tag{3.3}$$

Comparing Equations 3.2 and 3.3, one immediately realizes that advection dominates for the times

$$\Delta t \gg (3\times 10^{7}\,{\rm s})\,\xi\left(\frac{v_{\rm adv}}{1000\,{\rm km/s}}\right)^{-2}\left(\frac{E}{\rm GeV}\right)\left(\frac{B}{100\,\mu{\rm G}}\right)^{-1}, \tag{3.4}$$

and distances

$$\Delta y \gg (3\times 10^{12}\,{\rm cm})\,\xi\left(\frac{v_{\rm adv}}{1000\,{\rm km/s}}\right)^{-1}\left(\frac{E}{\rm GeV}\right)\left(\frac{B}{100\,\mu{\rm G}}\right)^{-1}. \tag{3.5}$$

Thus, for the GeV-electrons in the downstream region with the typical magnetic-field strengths of $\sim 100\,\mu$G, the diffusive transport dominates only on the very short time scales in the immediate vicinity to the shock front. Outside of the layer of the thickness $\sim D_s/v_{\rm adv} \simeq 3\times10^{12}\,{\rm cm} \simeq 10^{-6}\,{\rm pc}$, the transport of the electrons is governed by advection. Obviously, the width of the diffusion-dominated region is extremely small compared to the size of a remnant, usually of the order of a few parsec. Once escaped from the shock, the GeV-electrons cannot return, and their propagation is determined by the advective length, $l_{\rm adv}$. Provided that the turbulent re-acceleration region is large enough, $L_{\rm fm} \simeq \Delta y$, we can neglect the diffusive transport for the bulk of electrons that account for the synchrotron emission in the radio range. Further, since the spatial transport is mostly radial, the system can be reduced to a 1D problem with spherical symmetry. Thus, our findings allow us to define the position of an electron in the shock-rest frame as

$$y = R_{\rm sh} - r = l_{\rm adv} \simeq v_{\rm adv} t\,. \tag{3.6}$$

Here r is the usual radial coordinate, $R_{\rm sh}$ is the shock radius, and t is the time that particles spend leaving the shock front. Thus the initial time $t_0 = 0$ is the time when an electron leaves the shock, and the origin of the coordinate axis y is tied to the shock position, as marked in Figure 3.1. In the vicinity of the shock, the advective velocity is nearly constant, and hence the spatial coordinate y is linear in time. Using the fact that in our model particles move radially with the velocity $v_{\rm adv}$, we can simplify the relation between the volume-integrated, $N(p,t)$, and differential, $N(r,p,t)$, particle number densities:

$$4\pi r^2 N(r,p,t) = N(p,t)\delta(y - v_{\rm adv}t) = N(p,t)\delta(r - (R_{\rm sh} - v_{\rm adv}t))\,. \tag{3.7}$$

The time-evolution of the electron density follows then the transport equation for CR that contains diffusion in momentum space

$$\frac{\partial N(p,t)}{\partial t} = \frac{\partial}{\partial p}\left(D_p(p)\,p^2\frac{\partial}{\partial p}\left(\frac{N(p,t)}{p^2}\right)\right)\,, \tag{3.8}$$

where $D_p(p)$ is the corresponding momentum-diffusion coefficient. Time t and spatial coordinate y are equivalent in our model since they are related trough expression 3.6. Thus, the particle spectrum at the shock can be included as the initial condition at time t_0 in the form of a power-law

$$N(p,t_0) = N_0\,p^{-s}\,. \tag{3.9}$$

The power-law index $s = 2.0$ corresponds then to the well-known DSA solution for the strong shock.

In summary, an electron spectrum of the form given by Equation 3.9 is produced via DSA at the shock. As the electrons escape the shock with the velocity $v_{\rm adv}$, their spectrum undergoes changes determined by Equation 3.8. The particle-turbulence interactions responsible for the energy gain of electrons are described by momentum-diffusion coefficient $D_p(p)$. It is important to note that assuming the turbulent region to be small compared to the size of the remnant, the electrons that propagate away from the shock undergo acceleration only for a short time period. Therefore all the energy losses resulting from the expansion of the remnant can be neglected.

The key ingredient of our scenario is the momentum-diffusion coefficient, which contains the properties of the turbulence. Pohl et al. (2015) found that for an isotropic distribution function of particles the acceleration time does not depend on momentum. Based on this, we can set for the momentum-diffusion coefficient

$$D_p(p) = \frac{p^2}{\tau_{\rm acc}}f(p)\,, \tag{3.10}$$

where $f(p)$ is a dimensionless function, which we introduce to correct the acceleration of particles at higher energies. As mentioned in Pohl et al. (2015), at higher particle energies the isotropization of the corresponding distribution function becomes slower, and thus the stochastic acceleration less efficient. Therefore, it is useful to define the correction function as:

$$f(p) = \begin{cases} 1 & \text{for } p \le p_0 \\ \left(\frac{p}{p_0}\right)^{-m} & \text{for } p \ge p_0. \end{cases} \tag{3.11}$$

Above the critical momentum, p_0, the diffusion coefficient deviates from the form derived for the low-energy particles. The power-law index m determines how fast the acceleration time scale increases with the growing energy of electrons. In this work, the power-law index is a free parameter and is chosen to be $m \in [0, 1]$ to reflect a moderate modification from the momentum-independent diffusion coefficient. For the sake of convenience, we rewrite Equations 3.10 and 3.11 in normalized coordinates, which we define as

$$x = \frac{t}{\tau_{\mathrm{acc}}} \qquad \tilde{p} = \frac{p}{p_0}\,. \tag{3.12}$$

In the new dimensionless coordinates, the transport equation 3.8 becomes

$$\frac{\partial N}{\partial x} = \frac{\partial}{\partial \tilde{p}} \left(f(\tilde{p}) \tilde{p}^4 \frac{\partial}{\partial \tilde{p}} \frac{N}{\tilde{p}^2} \right)\,, \tag{3.13}$$

where the correction function reads

$$f(\tilde{p}) = \begin{cases} 1 & \text{for } \tilde{p} \leq 1 \\ \tilde{p}^{-m} & \text{for } \tilde{p} \geq 1. \end{cases} \tag{3.14}$$

As seen from Equations 3.13 and 3.14, there are two relevant parameters for the system. The first is the time in units of acceleration time scale, x. The second is the power-law index of the momentum-diffusion coefficient, m, which reflects the acceleration efficiency of the turbulence.

As the re-acceleration region is assumed to be small, the electrons reside there only for short time periods, and thus a steady-state solution of the reduced transport equation, $N \propto p^{m-1}$, is not applicable for our scenario. Approximate analytic solutions for equations of the form as Equation 3.13 are presented in the literature (e.g., Gallegos-Cruz and Perez-Peraza (1995); Becker et al. (2006)). For our needs, however, it is more convenient to solve Equation 3.13 numerically. The corresponding code is written in Python and employs the `FiPy` package[2] (Guyer et al., 2009), an object-oriented partial differential equation solver.

We solve Equation 3.13 in the range $0 \leq x \leq T$, where $T = L_{\mathrm{fm}}/v_{\mathrm{adv}}/\tau_{\mathrm{acc}}$ is the total time that a particle spends in the turbulent region in units of the acceleration time scale. The thin re-acceleration region (yellow area in Figure 3.1) would be hardly possible to resolve by radio measurements, and the observed synchrotron flux will be rather an averaged emission over the entire turbulent area. Thus, it is sufficient to calculate the averaged electron number density. Since time and spatial coordinates are equivalent in

[2] https://www.ctcms.nist.gov/fipy/

our model, we define the averaged electron number density as

$$N_{\rm ave}(\tilde{p}, T) = \frac{1}{T}\int_0^T N(\tilde{p}, x)\, dx\,. \tag{3.15}$$

The electrons far downstream maintain the momentum distribution previously gained in the re-acceleration region. Once escaped from the turbulent layer, they no longer undergo any re-acceleration process, and hence their number density is $N_{\rm ave}(\tilde{p}, x = T)$.

In the following section, the solution for $N_{\rm ave}$ for different parameters and the corresponding radio spectral indices are presented. The synchrotron flux is calculated using the emissivity function for a strongly turbulent magnetic field, presented in Section 2.4.1.

3.3 Results

First of all, we check if our code reproduces the steady-state solution of Equation 3.13 if running for significantly long times. Having established the correct test results for various values of parameter m in the steady-state regime, we can focus on the outcome that is relevant for our model. First, we choose for the initial condition the canonical DSA solution for test-particles, $N(p, t_0 = 0) = N_0 p^{-2}$, where we set $N_0 = 1.0$ for simplicity. We compute the integrated electron number density, $N_{\rm ave}$, as defined by Equation 3.15, for fixed $m = 0.6$ but varying times, T. The results are shown in Figure 3.2, where the particle number density $N_{\rm ave}$ is plotted as a function of normalized momentum (p/p_0) and multiplied by $(p/p_0)^2$ in order to emphasize the main scaling. The different lines represent results for varying time normalized by the acceleration time scale.

To be noted from the figure is a distinct bump with a peak slightly above $p/p_0 = 1.0$. As expected, the modification from the stochastic re-acceleration is more pronounced for the longer times available for the re-acceleration process. The peak of the bump shifts to higher momenta with larger T, illustrating that electrons gain higher energies when crossing wider turbulent regions. Nevertheless, it is remarkable that the flux enhancement in Figure 3.2 is pronounced even for one or less acceleration time scales. This indicates that the stochastic re-acceleration by the fast-mode waves in SNRs can be significant even for relatively long acceleration times or narrow turbulent regions.

In the next step, we investigate the dependency of the spectra on the momentum-diffusion coefficient parameter m. Therefore we run our code for the fixed $T = 0.5$ and vary the values of m; the corresponding results can be seen in Figure 3.3. The shape of the spectra does not really change for different m at momenta below $p/p_0 = 1.0$. But the high-energy tail above the critical momentum is basically determined by the momentum-diffusion parameter. As shown in Figure 3.3, the particle spectra attain higher momenta with smaller values of m.

Moreover, to be noted from the figure is that the tail can extend about two decades in momentum. As we shall see in the following plots, this effect causes a synchrotron spectra softer at lower momenta as the canonical -0.5.

Another interesting question is, how far the initial spectra at the shock affect the final

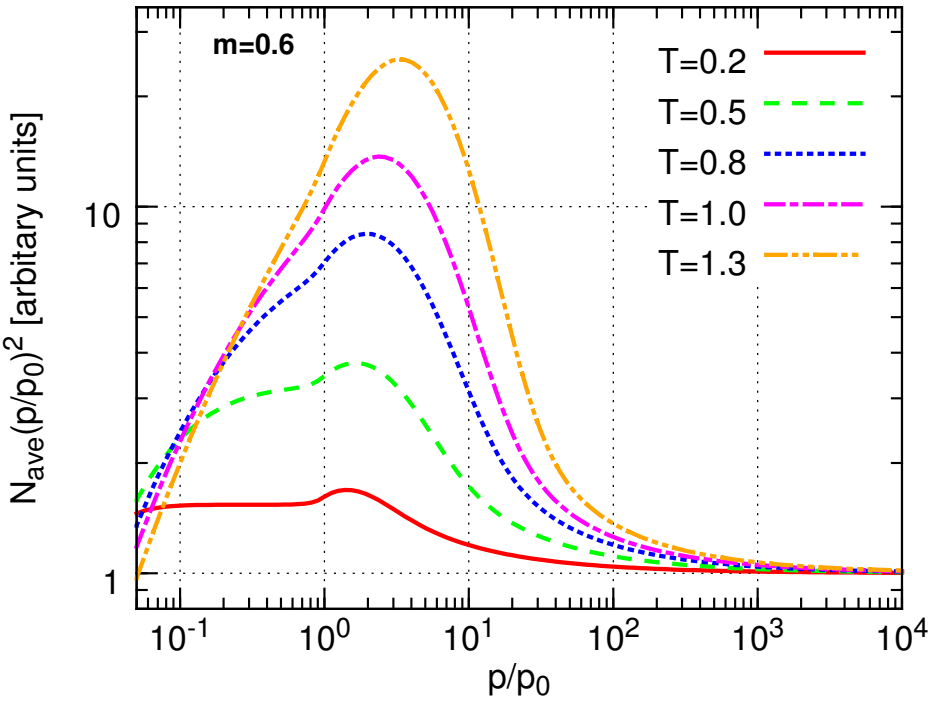

Figure 3.2: Averaged electron number density, N_{ave}, at different times T for fixed index, $m = 0.6$.

particle distribution produced by the stochastic re-acceleration. Therefore we perform calculations for three different values of the power-law index in the initial condition: $s = 1.7$, $s = 2.0$ and $s = 2.3$, where parameters $m = 0.6$ and $T = 0.5$ are fixed. Figure 3.4 presents results where the averaged electron number density is normalized by the associated initial condition $N(t_0)$. It is noteworthy that depending on the initial condition, the re-acceleration bump is unequally pronounced. Nevertheless, we observe degeneracy for certain parameters. As can be seen from Figure 3.4, the set of parameters $T = 0.7$ and $s = 2.0$ produce very similar spectral peak as for $T = 0.5$ combined with $s = 2.3$. Thus we conclude that the exact form of the initial condition plays a minor role in the spectral shape of the bump produced by stochastic re-acceleration.

Having obtained the electron spectra for various parameters, we can compute the synchrotron emission and the corresponding spectral index in the radio range. As mentioned before, therefor the emissivity function for turbulent magnetic field, given by Equation 2.40, is used. The radio spectral index is then presented as a function of normalized frequency (ν/ν_x), where (cf. Equation 2.36)

$$\nu_x \equiv \nu_0(B_{\text{rms}}, p_0) = \frac{3e}{4\pi m_e^3 c^3} B_{\text{rms}}\, p_0^2\,. \tag{3.16}$$

To simplify matters, we choose two values for the momentum-diffusion coefficient,

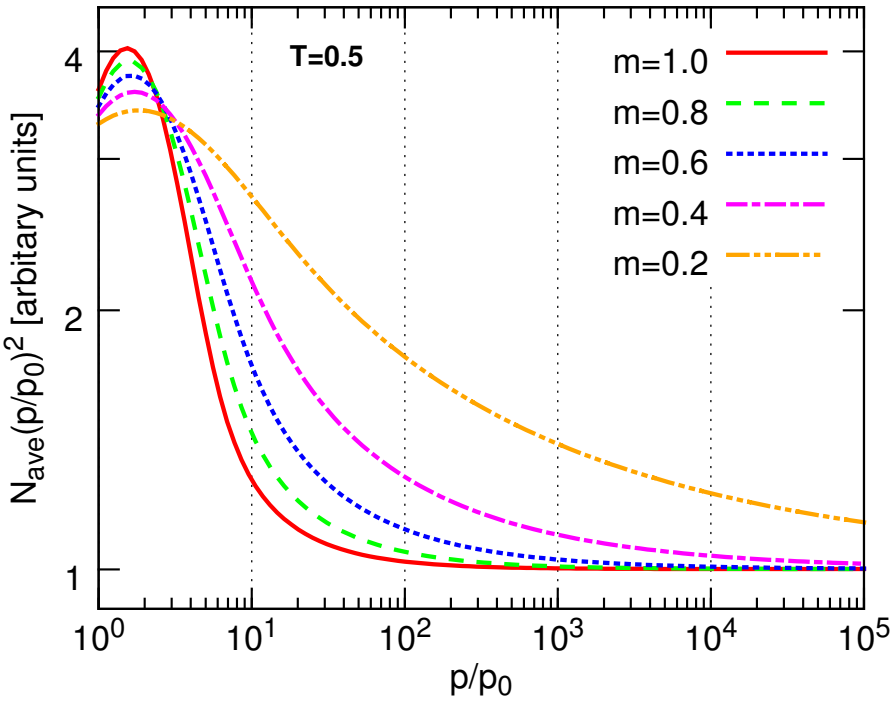

Figure 3.3: Averaged electron number density, $N_{\rm ave}$, plotted for various power indices of the momentum diffusion coefficient m and $T = 0.5$.

$m = 0.2$ and $m = 0.6$, and set at the shock the canonical DSA-solution $N_0 p^{-2}$. The radio flux directly from the turbulent shell (yellow-shaded area in Figure 3.1) originates from the averaged electron number density, given by Equation 3.15. Figure 3.5 shows the radio spectral index calculated for varying normalized times T in the immediate post-shock layer. Thus, the different lines represent how the spectral index changes with a wider re-acceleration region.

When electrons leave the turbulent layer, they keep the energy distribution $N(\tilde{p}, x = T)$ gained through passage of the turbulent region of the width $z_d = \tau_{acc} T v_{\rm adv}$. The corresponding radial spectra for the far downstream (violet-shaded area in Figure 3.1) are presented in Figure 3.6. To be noted from Figures 3.5 and 3.6 is that below $\sim 10\nu_x$ the spectra are harder than the canonical -0.5, and above this frequency the synchrotron spectra become significantly softer. This effect is more pronounced in the far downstream because the particles experienced the full re-acceleration region. It is important to stress that the total radio spectrum observed from an SNR would be an averaged emission of the two regions. The spectral softening is more pronounced for smaller parameters m, in the frequency range $(100 - 1000)\nu_x$. One can easily translate these values into typical quantities of an SNR. Thus, for $\nu_x = 10$ MHz the softening would be observed at $\sim (1 - 10)$GHz with corresponding magnetic-field strength $B_{\rm rms} \approx 100\,\mu$G and critical momentum $p_0 \approx 300\,{\rm MeV}/c$. For small m (e.g., $m = 0.2$ in upper plots of Figures 3.5 and 3.6), the soft synchrotron spectrum extends over three decades in frequency, and

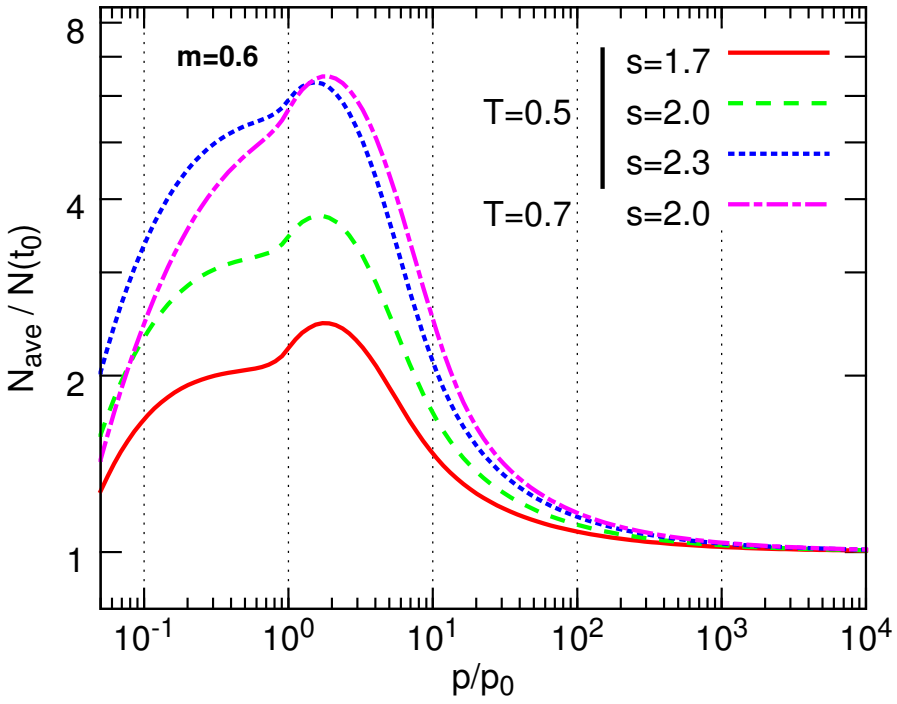

Figure 3.4: Averaged electron number density, $N_{\rm ave}$, normalized by the initial distribution, $N(t_0) = N_0 p^{-s}$, plotted for different initial indices, s.

its curvature is rather marginal. With increasing parameter m, the curvature becomes stronger, especially in the far downstream region (bottom plot in Figure 3.6). The spectral hardening below $\sim 10\nu_x$ is strongly frequency-dependent. For the above example with $\nu_x = 10$ MHz, the harder spectrum below 100 MHz and its curvature should be observable. Radio telescopes such as LOFAR (van Haarlem et al., 2013), which covers the frequency range from 10-240 MHz, should be able to detect hardening at low frequencies in SNRs.

To conclude from the results presented in this chapter is that the electron re-acceleration by fast-mode waves can soften the synchrotron spectrum in the radio range, with a corresponding spectral index between -0.6 and -0.7. In contrast, at very low frequencies a spectral hardening with significant curvature is visible. Summarizing, the stochastic re-acceleration in the immediate post-shock region provides a viable explanation for the soft radio spectra of many galactic SNRs. In the next chapter, we describe how the concept of stochastic re-acceleration is included in a comprehensive code designed for the global modeling of SNRs.

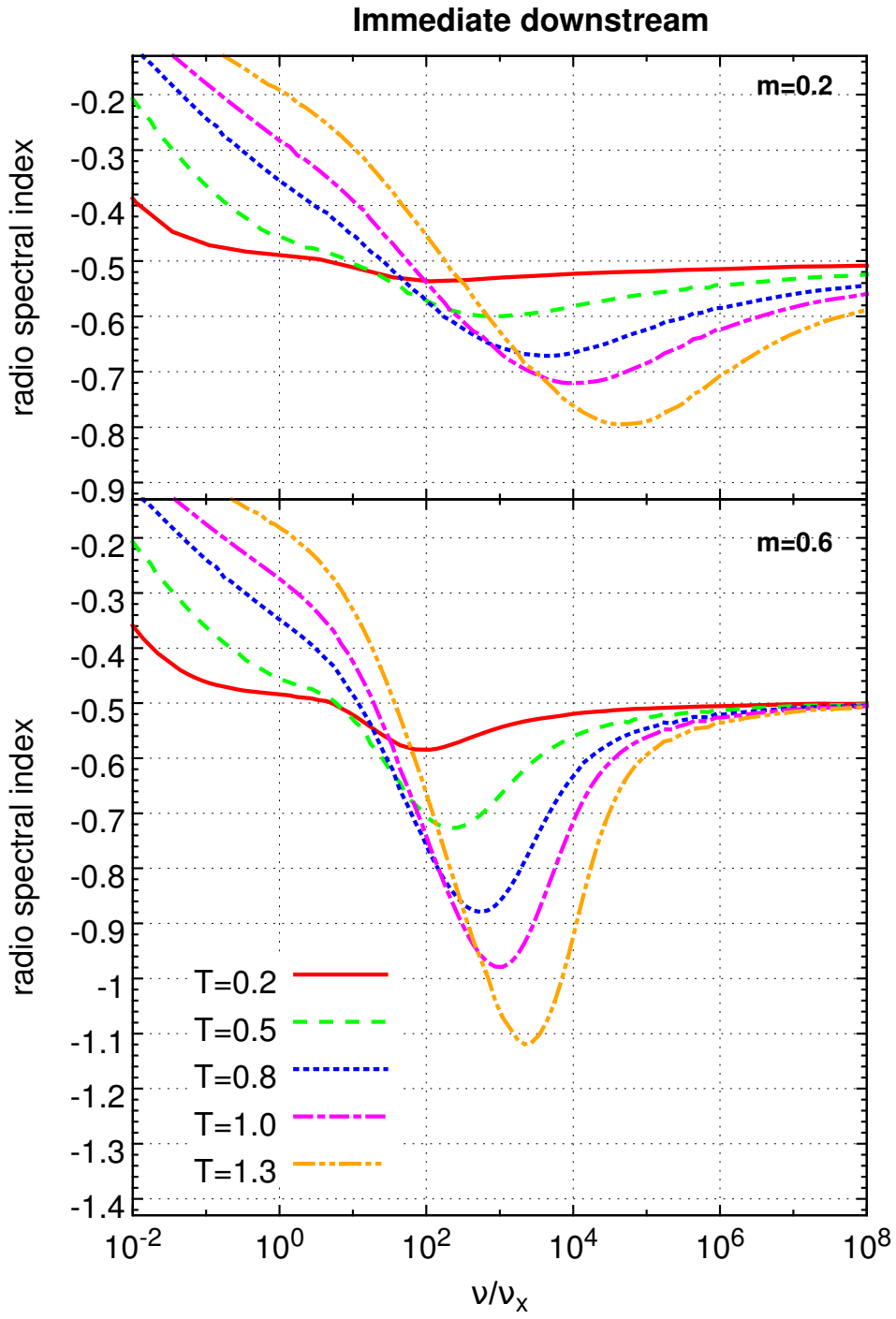

Figure 3.5: Radio spectral index of the shell where re-acceleration occurs, plotted for different times and two choices of m.

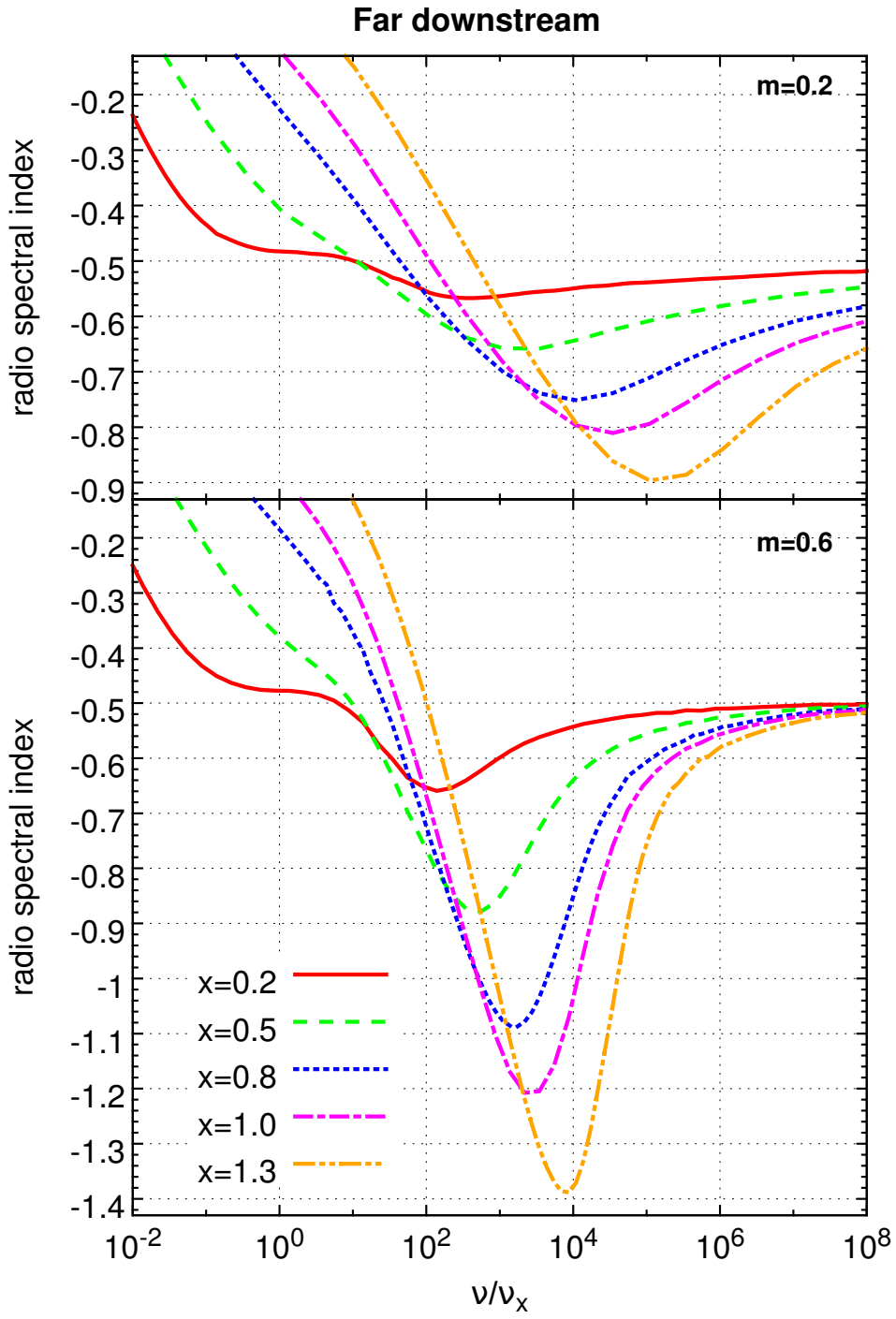

Figure 3.6: Radio spectral index of the far downstream region of an SNR, plotted for different times T and two choices of m.

Parts of this chapter have been published in
Wilhelm et al. 2020, A&A 639, A124
(See table of publications)

Chapter 4

RATPaC: Program for extensive SNRs modeling

4.1 Overview

Figure 4.1: **R**adiation **A**cceleration **T**ransport **Pa**rallel **C**ode (RATPaC) Logo, created by my husband, Igor Isaev, for which I am very grateful.

Throughout the rest of this work, the **R**adiation **A**cceleration **T**ransport **Pa**rallel **C**ode (RATPaC) is used. RATPaC is a fully time-dependent Python-based code that is designed to model particle acceleration and corresponding photon emission in SNRs. Its simplified structure is depicted in Figure 4.2. The blue rectangles represent the individual

program units and the yellow ellipses the program output, respectively. The main block of RATPaC, referred to as "Cosmic-ray transport", solves the transport equation for CR, similar to those presented in Section 2.3.3, and thus is responsible for particle acceleration. The hydrodynamic properties that go into the transport equation for CR can be either provided by comprehensive hydrodynamic simulations or by analytic profiles (Truelove and McKee, 1999; Cox, 1972). Similarly, the magnetic-field profiles can be set analytically or calculated from the plasma flow with the induction equation for ideal MHD. RATPaC is used in the test-particle regime, which enables to treat the transport of CR and the hydrodynamic equations of SNR evolution independently. Both hydrodynamics and particle acceleration are fully time dependent. The transport equation is individually solved for electrons and protons, as well as for forward and reverse shocks. From particle number densities, RATPaC computes the corresponding photon spectra: synchrotron flux, NTB, and γ-ray emission via IC scattering from electrons, and via neutral-pion decay from protons. All together the different emissions give the entire time-dependent and spatially resolved spectral energy distribution (SED) of an SNR, which can be compared to the observational data. More details on RATPaC can be found in Telezhinsky et al. (2012a), Telezhinsky et al. (2012b), and Telezhinsky et al. (2013).

The novel aspect in this work is the inclusion of the second-order Fermi acceleration into RATPaC, which is described in more detail in the following sections. It is important to stress here that RATPaC offers a wide variety of possibilities, e.g., self-consistent calculation of the Alfvénic turbulence generated by the accelerated particles (Brose et al., 2016). Further, the recent version of RATPaC is able to solve hydrodynamical equations on-the-fly (Sushch et al., 2018; Brose et al., 2019, 2020) as well as to calculate hadronic γ-ray emission from havier nuclei (Bhatt et al., 2020). However, only RATPaC features that are used throughout this work are described here in detail.

4.2 Magnetic field

RATPaC offers a large variety of magnetic field profiles available for calculations. For example, the magnetic-field strength can be set as a constant value for the entire remnant or scale linearly with the plasma density. This thesis is confined to two concrete options since they are used in the following chapter to model Tycho's SNR.

For both scenarios, the canonical value for the magnetic-field strength of the ISM in the far upstream is used: $B_{\mathrm{ISM}} = 5\,\mu\mathrm{G}$. In the vicinity of the shock, the magnetic field is amplified, e.g., due to streaming instabilities (Bell, 2004; Bell and Lucek, 2001). The exact treatment of the magnetic-field amplification is beyond the scope of this work. We adopt instead for the magnitude of the magnetic-field strength in the immediate upstream region $B_1 = \sigma B_{\mathrm{ISM}}$, where σ, a generic amplification factor, is a free parameter in our model. Following the ansatz used by Zirakashvili and Ptuskin (2008) and Brose et al. (2016), the magnetic-field profile in the precursor is assumed to drop exponentially to the

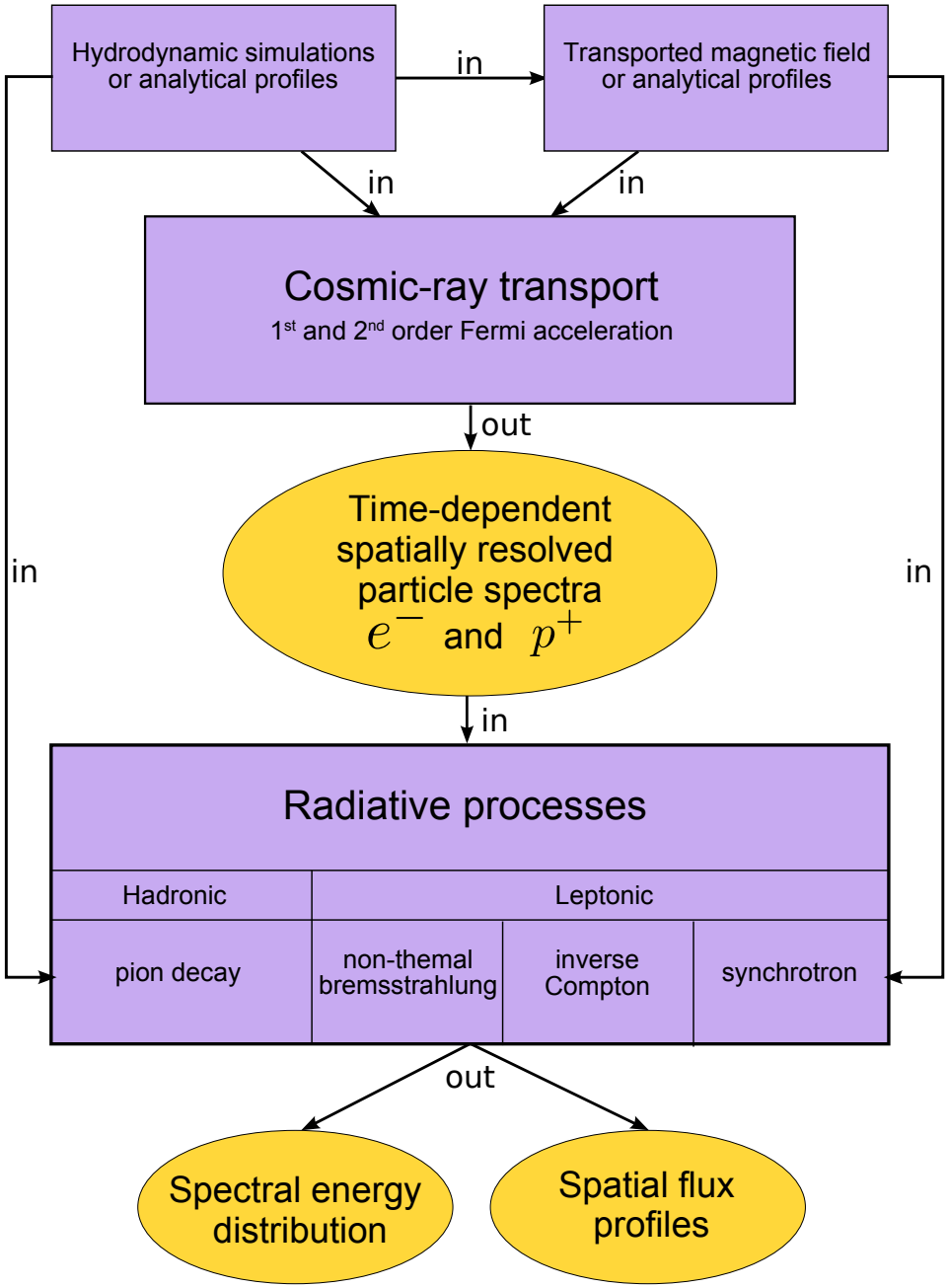

Figure 4.2: Schematic structure of **R**adiation **A**cceleration **T**ransport **Pa**rallel **C**ode (RATPaC).

interstellar field, $B_{\rm ISM}$, at a distance of 5% of the shock:

$$B(r) = \begin{cases} \sigma B_{\rm ISM} \cdot \exp\left(\frac{-(r/R_{\rm sh}-1)}{0.05} \cdot \ln(\sigma)\right) & \text{for } R_{\rm sh} \leq r \leq 1.05 \cdot R_{\rm sh} \\ B_{\rm ISM} & \text{for } r \geq 1.05 \cdot R_{\rm sh}\,. \end{cases} \tag{4.1}$$

It is important to stress that the magnetic-precursor length scale is not related to a spatial "free-escape" boundary, which is usually introduced in the global modeling of SNRs (Völk et al., 2008; Morlino and Caprioli, 2012; Slane et al., 2014). The precursor merely reflects typical characteristics of the spatial profile of the amplified magnetic field in the upstream region.

The pre-shock magnetic field is assumed to be isotropic, i.e., its individual components are equal in their magnitudes. Shock compression for the strong unmodified shock yields an immediate downstream value of

$$B_2 = \sqrt{\frac{1+2\,r_{\rm sh}^2}{3}}\,B_1 = \sqrt{11}\,B_1\,. \tag{4.2}$$

As mentioned above, two scenarios for the magnetic-field distribution inside an SNR are considered in this work. In the first case, the immediate downstream value of the magnetic field is transported inside the SNR with the plasma flow and evolves according to the induction equation for ideal MHD (Telezhinsky et al., 2013):

$$\frac{\partial \boldsymbol{B}}{\partial t} = \boldsymbol{\nabla} \times (\boldsymbol{u} \times \boldsymbol{B})\,. \tag{4.3}$$

Here $\boldsymbol{B}$ is the magnetic-field vector, and $\boldsymbol{u}$ the plasma velocity obtained from hydrodynamic simulations. Equation 4.3 accounts for advection, stretching and compression of the field, implying that magnetic flux is conserved during the entire evolution of the SNR. The separate treatment of hydrodynamics and calculation of magnetic field with Equation 4.3 is justified as long as the dynamic back-reaction from magnetic field is negligible. We shall discuss it in more detail on a concrete example in Section 6.3.

For the second case, we assume that after being amplified in the upstream region and compressed at the shock, the magnetic field decays due to the damping of magnetic turbulence in the downstream region. Magnetic-field damping is one of the key processes in astrophysical plasmas (Kulsrud and Cesarsky, 1971; Threlfall et al., 2011), and is expected to operate in SNRs, where it dissipates turbulently amplified magnetic field (Pohl et al., 2005; Sushch et al., 2018). We do not know the turbulence mode that is most relevant for magnetic-field amplification in SNRs. Instead, we adopt a simple parametrization for the magnetic profile in the downstream region:

$$B(r) = B_0 + (B_2 - B_0) \cdot \exp\left(\frac{-(R_{\rm sh}-r)}{l_{\rm d}}\right)\,, \tag{4.4}$$

where l_d is the characteristic damping length of magnetic turbulence. The residual field level, B_0, is the limit value to which the magnetic-field tends in the far downstream, behind the CD, and the reverse shock of the SNR. In contrast to the previous case, the magnetic flux is not conserved in the scenario described by Equation 4.4. Far inside the remnant, the advection of magnetic field has to become important as the magnetic field approaches the constant value B_0. This inner field is, however, physically nonrelevant. The bulk of the accelerated particles resides in the vicinity of the shock and therefore do not experience the constant magnetic field, B_0. Most of the particles accelerated at the forward shock cannot cross the CD, which separates the swept-up material from the ejecta, because their dynamics are governed by advection. Only a marginal fraction of the very-high energetic particles overcome the CD via diffusive transport. Their radiative contribution to the synchrotron spectrum does not exceed 1% of the overall emission, and is thus negligible for the global SED modeling. Therefore, in the case of particle acceleration at the forward shock, we can omit the advection of magnetic field for the second scenario that includes magnetic-field damping.

The spatial and time-dependent magnetic-field profile goes into calculation of the gyroradius of particles, r_g. Thus, the spatial-diffusion in the block "CR transport" is dynamically co-determined by magnetic-field profile. Furthermore, magnetic-field strength is used to calculate the synchrotron losses of electrons and the corresponding emission flux.

4.3 Transport equation for cosmic rays

To determine the evolution of the differential particle number density, $N(\mathbf{r}, p, t)$, RATPaC solves the *time-dependent* transport equation for CR in space, $\mathbf{r}$, and momentum, p, coordinates:

$$\frac{\partial N}{\partial t} = \nabla(D_s \nabla N - \boldsymbol{u} N) - \frac{\partial}{\partial p}\left((N\dot{p}) - \frac{\nabla \boldsymbol{u}}{3} N p\right) + \frac{\partial}{\partial p}\left(p^2 D_p \frac{\partial}{\partial p}\frac{N}{p^2}\right) + Q\,. \tag{4.5}$$

Here, the spatial diffusion coefficient, with the speed of light c and the Larmor radius r_g is defined in the downstream region as

$$D_s(\mathbf{r}) = \xi \frac{c\, r_\mathrm{g}(\mathbf{r})}{3}\,. \tag{4.6}$$

The parameter ξ is the ratio between the spatial diffusion coefficient and that for Bohm diffusion, sometimes referred to as the gyrofactor. The Larmor radius and hence the spatial diffusion coefficient are calculated using the local magnetic-field strength. Because in our approach the magnetic field is spatially variable (see Section. 4.2), the spatial diffusion coefficient also varies with position. In the upstream region beyond $2R_\mathrm{sh}$, a

Galactic diffusion coefficient is set (Berezinskii et al., 1990; Trotta et al., 2011)

$$D_{\mathrm{G}} = 10^{29} \left(\frac{E}{10\,\mathrm{GeV}} \right)^{1/3} \left(\frac{B}{3\,\mu\mathrm{G}} \right)^{-1/3} \mathrm{cm}^2/\mathrm{s}\,. \tag{4.7}$$

Here, E is the CR energy, and B is the local magnetic-field strength. The transition between Bohm and Galactic diffusion coefficients occurs in RATPaC exponentially with distance.

The synchrotron losses for electrons are included in Equation 4.5 via

$$\dot{p} = \frac{4e^4 B^2}{9c^6 m_e^4} p^2 \equiv b p^2\,, \tag{4.8}$$

with the elementary charge e and the electron rest mass m_e. The synchrotron losses are nonrelevant for protons due to large particle mass and thus are omitted in RATPaC. The plasma velocity, $\boldsymbol{u}$, is obtained from hydrodynamic simulations or from an analytic profile. Stochastic re-acceleration is represented in Equation 4.5 by the momentum diffusion coefficient, D_p, and the injection of particles into the shock is described by the source term, Q. It is important to note here that the original version of RATPaC ignored the diffusion in momentum space and thus neglected the fifth term on the right-hand side. In contrast, the major focus of this work is stochastic acceleration and hence the diffusion in momentum space.

There are several coordinate transformations that we perform to optimize the numerical calculations. The energies of charged particles participating in our simulations range from supra-thermal to ultra-high energies. Hence, the momentum coordinate p has to span ∼25 orders of magnitude to account for all CR in the system. Thus, it is useful to transform Equation 4.5 into the log-scale in momentum space. Defining a normalized particle momentum $p' \equiv p/m_i c$, where m_i is the mass of the corresponding particle species, we can set

$$y \equiv \ln p'\,, \tag{4.9}$$

Following the above notation, we reassign the differential number density, momentum-diffusion coefficient and the source term related to the original quantities by the multiplication of factor e^y:

$$N_y \equiv e^y N = p' N = \frac{d\mathcal{N}}{dV\,dy}\,, \tag{4.10}$$

$$D_y \equiv e^y D_p = p' D_p\,, \tag{4.11}$$

$$Q_y \equiv e^y Q = p' Q\,. \tag{4.12}$$

With transformations 4.9 to 4.12 Equation 4.5 becomes

$$\frac{\partial N_y}{\partial t} = \nabla(D_s \nabla N_y - \boldsymbol{u} N_y) + \frac{\nabla \boldsymbol{u}}{3}\frac{\partial N_y}{\partial y} - \frac{\partial}{\partial y}(be^y N_y) + \frac{\partial}{\partial y}\left(D_y \frac{\partial}{\partial y}(e^{-3y} N_y)\right) + Q_y \,. \quad (4.13)$$

Since a remnant expands rapidly with time, it is convenient to introduce a co-moving frame tied to the shock radius. The new spatial coordinate, normalized by the shock radius, is then defined as

$$r' = \frac{r}{R_{\rm sh}(t)} \,. \quad (4.14)$$

The benefit of the above transformation is that the shock position is at a fixed known cell during the entire calculation. Another advantage of the co-moving coordinate is that our approach does not need a spatial escape boundary. Conventionally, the escape of high-energy particles is implemented by setting the condition $N(x_b, p) = 0$, which emulates the presence of a free-escape boundary at x_b. In contrast, in our treatment the system is large enough (ca. 65 shock radii) to retain all injected particles in the simulation.

Since the spatial diffusion coefficient scales linearly in momentum, the diffusion length of the lowest-energy particles is extremely small. Thus, to resolve newly injected particles at the shock, a very fine grid at $r' = 1.0$ is required. To avoid computationally expensive treatment but to increase the spatial resolution at the shock we, perform another coordinate transformation

$$(r' - 1) = (r_* - 1)^3 \,, \quad (4.15)$$

with corresponding Jacobian

$$J(r_*) \equiv \frac{\partial r'}{\partial r_*} = 3(r_* - 1)^2 \,. \quad (4.16)$$

Substituting the coordinate r' with a new coordinate r_*, for which a uniform grid is set, allows us to achieve a very fine grid in the shock vicinity. At the same time, the numerical costs stay relatively low. As a natural consequence, our mesh becomes more coarse with the shock distance. But the modest resolution far from the shock is justified due to the large mean free path of the particles far upstream. A large Galactic diffusion coefficient particularly ensures that a fine spatial grid becomes unimportant. In contrast, the enhanced spatial resolution close to the shock is of advantage for second-order Fermi acceleration, which we implement in the immediate downstream region.

With the above transformations Equation 4.13 can be rewritten for a spherically sym-

metric shock wave as

$$\begin{aligned}\frac{\partial N_y}{\partial t} =& \frac{1}{J(r_*)}\frac{\dot{R}_{\rm sh}}{R_{\rm sh}}R(r_*)\frac{\partial}{\partial r_*}N_y + \frac{1}{J(r_*)}\frac{1}{R(r_*)^2}\frac{1}{R_{\rm sh}^2}\frac{\partial}{\partial r_*}\frac{R^2(r_*)D_s}{J(r_*)}\frac{\partial}{\partial r_*}N_y \\ &- \frac{1}{J(r_*)}\frac{1}{R^2(r_*)}\frac{1}{R_{\rm sh}}\frac{\partial}{\partial r_*}(R^2(r_*)u_r N_y) + \frac{1}{J(r_*)}\frac{1}{R^2(r_*)}\frac{1}{3R_{\rm sh}}\frac{\partial(R^2(r_*)u_r)}{\partial r_*}\frac{\partial N_y}{\partial y} \\ &- \frac{\partial}{\partial y}(be^y N_y) + \frac{\partial}{\partial y}\left(D_y\frac{\partial}{\partial y}(e^{-3y}N_y)\right) + \frac{Q_y}{R_{\rm sh}J(r_*)}, \end{aligned} \tag{4.17}$$

where u_r is the radial component of the plasma velocity and $R(r_*) \equiv (r_* - 1)^3 + 1$. To solve Equation 4.17 numerically, the `FiPy` library (Guyer et al., 2009), which contains implicit finite-difference methods, is used.

Equation 4.17 is applied for spherically symmetric shocks. The program unit "CR transport" is individually run for forward and reverse shocks since the corresponding particle number densities are independent. The total number density is obtained as a sum of the forward and reverse-shocks contributions. Also, for electrons and protons separate runs are made. The "CR transport" produces particle spectra for the desired time, which are used to obtain the emission fluxes. More details on the method to solve the transport equation can be found in Telezhinsky et al. (2012a).

4.4 Injection

The injection of particles is a complex issue that is not yet fully understood. For simplicity, in RATPaC the thermal leakage injection model, as presented in Blasi et al. (2005), is applied. The source term for electrons and protons is given by

$$Q_i = \eta_{\rm i} n_{1,i} V_{\rm sh} \delta(r - R_{\rm sh})\delta(p - p_{\rm inj,i})\,, \tag{4.18}$$

where index i denotes the particle species (electrons and protons), $\eta_{\rm i}$ the corresponding injection efficiency, and $n_{1,i}$ the particle number density in the upstream region. The particles in this approach are mono-energetically injected. The associated injection momentum is multiple of the mean thermal momentum:

$$p_{\rm inj,i} = 4.45 p_{\rm th,i} \equiv 4.45\sqrt{2 m_i k_{\rm B} T_d}\,, \tag{4.19}$$

where $k_{\rm B}$ is the Boltzmann constant and T_d is the temperature of the plasma in the immediate downstream region. In RATPaC the temperature, T_d, is dynamically read out from the hydrodynamic profile.

Electrons and ions are not in equilibrium at collisionless shocks. In fact, the Rankine-Hugoniot ion temperature is about 100 keV, whereas the observed electron temperature in the post-shock medium is of the order of 1 keV after years of residence in the downstream

region. The ratio of the temperatures of the two particle species scales as $T_e/T_p \propto V_{\rm sh}^{-2}$, and hence for typical shock velocities, $\sim 4000\,\mathrm{km/s}$, one obtains $T_e/T_p \approx 0.01$ (Ghavamian et al., 2007; van Adelsberg et al., 2008).

The thermal leakage model is based on the requirement that particles see the shock as a sharp discontinuity and hence are injected only if their Larmor radius exceeds the width of the shock wave. This condition requires that electrons need to be pre-accelerated to around 100 MeV to participate in DSA. Particle-in-cell simulations provide evidence that thermal electrons can indeed be pre-accelerated by shock-surface and shock-drift acceleration (Matsumoto et al., 2017; Bohdan et al., 2017). Tests demonstrate (Katou and Amano, 2019) that this process yields electron spectra shaped as a power law with a spectral index in the range $\sim (1.5 - 5.5)$. The exact value of the spectral index depends on the internal structure of the shock transition region. We approximate the two-step energization of electrons by DSA at all momenta and electron injection at very low momentum, which intends to replace an advanced, computationally far more expensive treatment of the pre-acceleration. Thus, the same particle temperature set for Equation 4.19 is supposed to mimic the pre-acceleration process of electrons. Although, we do not know the exact value of the spectral index provided by the shock-drift acceleration, it only marginally affects our final spectra, as shown in Chapter 3 (Figure 3.4).

The injection efficiencies of protons, η_p, and electrons, η_e, are free parameters in RATPaC. Since the proton injection efficiency controls the CR pressure, one needs to check a posteriori that the ratio of CR-to-ram pressures stays within the framework of the test-particle approximation.

4.5 Stochastic re-acceleration in RATPaC

As mentioned before, the novel aspect in this work is the stochastic re-acceleration of particles presented in Equation 4.5 by the momentum-diffusion coefficient D_p. Similarly to the approach presented in Chapter 3, the stochastic re-acceleration in RATPaC operates in a thin region behind the forward shock wave. First of all, it is important to stress that the streaming instabilities that amplify the magnetic field do not contribute to the diffusion in momentum space. We recall that the nonresonant instability produces almost standing waves, which cannot be responsible for second-order acceleration. The resonant streaming instability generates Alfvén waves that feature the same helicity and hence tend to move in the same direction. Since for an effective second-order Fermi acceleration a presence of forward and backward moving waves is required (Dung and Schlickeiser, 1990), also the resonant streaming instability fails to accelerate particles.

Pohl et al. (2015) explicitly derived the momentum-diffusion coefficient for the fast-mode waves and demonstrated that for low-energy particles with isotropic distribution function, the acceleration time is independent of momentum and can be of the order of a few years. At higher energy, where the isotropy assumption breaks down, the process is expected to become less efficient. A useful parametrization of the momentum diffusion

coefficient, D_p, is then (Pohl et al., 2015)

$$D_p(r,p) = \begin{cases} 0 & \text{for } r < (R_{\rm sh} - L_{\rm fm}) \\ \frac{p^2}{\tau_{\rm acc}} f(p) & \text{for } (R_{\rm sh} - L_{\rm fm}) \leq r \leq R_{\rm sh} \\ 0 & \text{for } r > R_{\rm sh}\,. \end{cases} \tag{4.20}$$

Exactly as in Chapter 3, $L_{\rm fm}$ denotes the width of the turbulent zone, $\tau_{\rm acc}$ is the acceleration time at small momenta, and $f(p)$ approximates the loss in acceleration efficiency at higher energies as a power law,

$$f(p) = \begin{cases} 1 & \text{for } p \leq p_0 \\ \left(\frac{p}{p_0}\right)^{-m} & \text{for } p \geq p_0\,. \end{cases} \tag{4.21}$$

The critical momentum p_0 and the power-law index m are free parameters of our model. It is important to note here that the energy in fast-mode waves has mostly a kinetic character. As the magnetic component of the fast-mode turbulence in the typical post-shock plasma is weak, it cannot amplify the magnetic field sufficiently. Therefore, in our approach another type of waves, such as nonresonant streaming instability (Bell, 2004) or turbulent dynamos (Giacalone and Jokipii, 2007), are required to provide the magnetic-field amplification at the shock, which is an important scale factor for scattering (see Section. 4.2). There is not necessarily a simple scaling between momentum and spatial diffusion (e.g., Yan and Lazarian, 2004, Equation 14). In addition, different types of turbulence may be responsible for the diffusive transport and stochastic re-acceleration (e.g., Shalchi, 2009, page 23). Therefore, the spatial and momentum diffusion coefficients are independent in our model.

The energy in the fast-mode turbulence that occurs in the post-shock region can be primarily provided by the background plasma. In RATPaC the energy density in the fast-mode waves scales with the thermal energy density of the post-shock background plasma

$$U_{\rm fm} = \epsilon U_{\rm th}\,. \tag{4.22}$$

Here, ϵ is the energy-conversion factor, which is a free parameter in the code and assumed to be of the order of a few percent. The minor value of ϵ provides that the energy transfer from the main plasma flow can be neglected for hydrodynamic simulations. For a strong shock expanding in a cold plasma, the Rankine-Hugoniot conditions provide for the downstream thermal energy

$$U_{\rm th} \approx \frac{9}{8}\rho_{\rm ISM} V_{\rm sh}^2\,, \tag{4.23}$$

where $\rho_{\rm ISM}$ denotes the ambient gas density.

The acceleration time for the fast-mode waves, derived in Pohl et al. (2015), is given

by

$$\tau_{\rm acc} \approx (0.63\,{\rm yr}) \left(\frac{U_{\rm th}}{10\,U_{\rm fm}} \right) . \tag{4.24}$$

If the energy density of the fast-mode waves scales with the thermal post-shock energy density of the plasma, as reflected by Equation 4.22, Equation 4.24 simplifies to

$$\tau_{\rm acc} \approx (6.3\,{\rm yr}) \left(\frac{\epsilon}{0.01} \right)^{-1} , \tag{4.25}$$

providing that the acceleration time scale depends only on the energy fraction that is transferred to the fast-mode waves.

The re-acceleration of CR will inevitably damp the fast-mode waves and affect the width of the turbulent region, $L_{\rm fm}$. The latter quantity can be estimated by equating the energy density of the fast-mode waves, $U_{\rm fm}$, and the total energy per volume that went into CR. Its value can be obtained from the energy transfer rate from waves to particles, $\dot{E}_{\rm tr}$, and the time period that particles spend in the turbulent region interacting with fast-mode waves, Δt, providing

$$U_{\rm fm} = \dot{E}_{\rm tr} \cdot \Delta t = \frac{U_{\rm cr}}{\tau_{\rm acc}} \cdot \frac{L_{\rm fm}}{u_2} . \tag{4.26}$$

Here, $U_{\rm cr}$ is the CR energy density in the immediate post-shock region induced by the stochastic re-acceleration. Combining Equations 4.24 and 4.26, we finally obtain

$$L_{\rm fm} \approx (5 \times 10^{13}\,{\rm cm}) \left(\frac{V_{\rm sh}}{1000\,{\rm km/s}} \right) \left(\frac{U_{\rm th}}{U_{\rm cr}} \right) . \tag{4.27}$$

Equation 4.27 is implemented in RATPaC as a time-dependent function, where $V_{\rm sh}$ and $U_{\rm th}$ are read out from hydrodynamic files. Thus, in contrast to the model presented in Chapter 3, the width of the re-acceleration region is self-consistently calculated and time dependent. Summarizing, the thickness of the re-acceleration region is limited by damping of the turbulence caused by the re-acceleration of particles. Therefore, in our method, $U_{\rm cr}$ from Equation 4.27 is coupled to the intermediate results from Equation 4.5 for the immediate post-shock area. Calculating the energy density of CR, $U_{\rm cr}$, we do not take the contribution from electrons into account because, in our model, their energy is negligible compared to that of protons. Thus, the first step is to run the program unit "CR-Transport" for protons to determine the width of the re-acceleration layer, which is used for electrons in the next step.

Finally, it is important to note that the physically essential quantity for stochastic re-acceleration is the amount of energy available for it, here in the form of fast-mode waves and described by the parameter ϵ. The size of the turbulence region, $L_{\rm fm}$, follows from the acceleration time scale, $\tau_{\rm acc}$, and only their ratio is relevant for the resulting particle spectra. The reason for this is that re-acceleration, once efficient, becomes the main

damping mechanism for the waves and hence ceases when the energy supply is exhausted.

4.6 Radiative processes

To account for the entire SED from an SNR, we calculate synchrotron radiation of electrons and γ-ray radiation resulting from leptonic and hadronic interactions. The synchrotron emission is calculated following Blumenthal and Gould (1970). The original version of RATPaC applied the standard emissivity function to calculate the synchrotron flux (cf. Section 2.4.1). For this work, the modified emissivity function for a turbulent magnetic field (Pohl et al., 2015) was additionally implemented. In the following, we shall use the modified emissivity function from Pohl et al. (2015) when modeling particular SNRs. NBT and IC radiation, which can significantly contribute to the γ-ray spectrum of SNR, are also obtained from the nonthermal electron distribution. The NTB contribution from relativistic electrons follows the calculations of Blumenthal and Gould (1970). For the IC interactions (Blumenthal and Gould, 1970), CMB and IR background can be taken into account. Hadronic γ-rays are the result of decays of neutral pions and other secondaries produced in interactions of CR with nuclei of the ISM. To calculate its spectrum, we follow the method from Huang et al. (2007), who provided matrices for cross section and secondary production obtained from Monte-Carlo simulations. Additionally, the latest version of RATPaC provides thermal bremsstrahlung for a fixed temperature of the thermal electrons in local thermodynamic equilibrium, as estimated in Hnatyk and Petruk (1999).

4.7 Tests for RATPaC

In this section, tests for the RATPaC version that includes stochastic re-acceleration are presented. For the following results, analytic profiles of Cox (1972) for Type Ia SNR in Sedov stage are used, where the explosion energy of supernova is set to 10^{51} erg and the ambient density is $n_{\mathrm{H}} = 0.4\,\mathrm{cm}^{-3}$. It is important to note that only acceleration at the forward shock is taken here into account. The magnetic-field inside the remnant is calculated via Equation 4.3, its value at the shock is set $B = 100\,\mu\mathrm{G}$. To model the spatial diffusion, the Bohm-diffusion coefficient (i.e., $\xi = 1.0$) is chosen. Having established in Chapter 3 that $m = 0.3$ typically provides soft electron spectra, we fix the momentum diffusion parameter m to 0.3 for all following test results.

First, we consider a time-evolution of the proton spectrum that is simultaneously produced by DSA and stochastic re-acceleration by the fast-mode waves. Critical momentum for momentum-diffusion coefficient is set to $p_0 = 1\,\mathrm{MeV/c}$, and the energy fraction is chosen to be $\epsilon = 0.01$. The latter setting means that 1% of the thermal energy of the downstream plasma is transferred to fast-mode waves and thus is available for stochastic re-acceleration. Figure 4.3 illustrates comparisons between electron and proton number densities with and without stochastic re-acceleration, respectively. The particle number densities are obtained by solving Equation 4.5 and are averaged over the SNRs volume. In this section, all spectra are referred to the downstream region of a remnant.

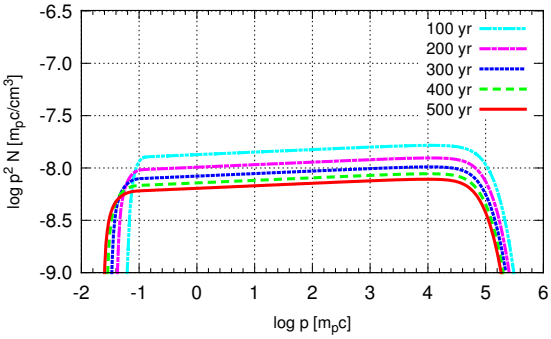

(a) Protons without stochastic re-acceleration.

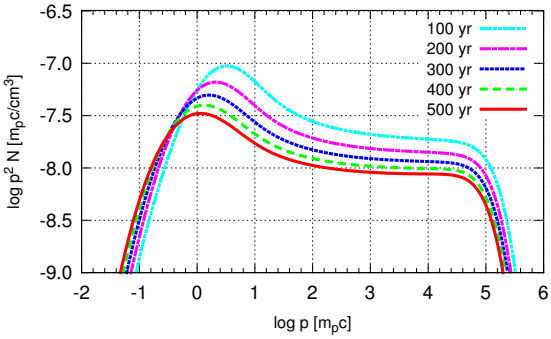

(b) Protons with stochastic re-acceleration.

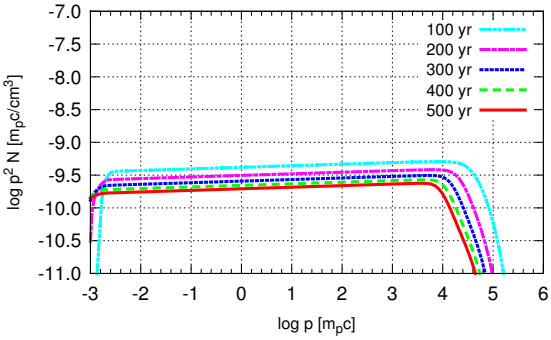

(c) Electrons without stochastic re-acceleration.

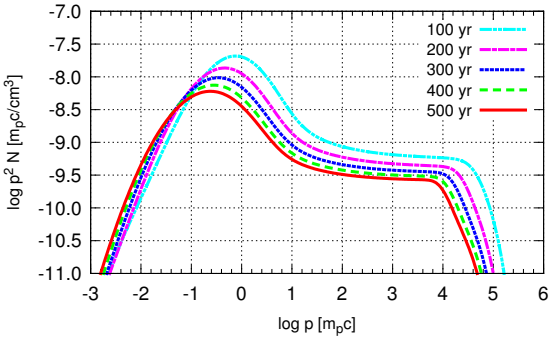

(d) Electrons with stochastic re-acceleration.

Figure 4.3: Time-evolution of electron and proton spectra for scenarios with and without stochastic re-acceleration, respectively.

Time-evolution of proton spectrum generated without stochastic re-acceleration is presented in Figure 4.3(a). To note from the plot is that the normalization of the particle spectra slightly decreases with time. The reason is the time-dependent injection of particles implemented in RATPaC. In fact, the particle number density with spectral index $s = 2$ scales linearly with injection momentum, $p_{\rm inj}$, as can be seen from Equation 2.29. Since the downstream temperature drops with time, so does the injection momentum (cf. Equation 4.19). Another feature of our approach is that the maximum energy of particles, $E_{\rm max}$, decreases with time. This is attributed to the time-dependent hydrodynamics. Indeed, the maximum CR energy in the age-limited case scales linearly with time, and as the square of the shock velocity (e.g., Reynolds):

$$E_{\rm max} \propto V_{\rm sh}^2\, t\,. \tag{4.28}$$

In Sedov-Taylor phase, the shock velocity scales with time as $t^{-3/5}$, as seen by Equation 2.5. Thus, Equation 4.28 gives the relation between the maximum CR energy and time in Sedov-Taylor phase

$$E_{\rm max} \propto t^{-1/5}\,, \tag{4.29}$$

which demonstrates that the maximum energy falls with time. Figure 4.3(b) shows proton spectra generated with switched-on stochastic re-acceleration. To be noted from the figure are that the spectra exhibit distinct bumps around $(1 - 100)m_pc$. Obviously, even with a moderate energy fraction converted to turbulence, modification of the proton spectra is substantial. The spectral bump shrinks with time since the thermal energy in the downstream region decreases due to decelerating shock velocity, and thus less energy becomes available for the re-acceleration. Furthermore, it can be seen from Figure 4.3(b) that the spectral peak slightly broadens with time. The reason is that the bump at later times represents an effectively integrated spectra over the earlier distributions.

Figure 4.3(c) shows the electron spectrum produced by DSA evolving over time. Just like for the proton spectrum, the normalization and the maximum energy of the electron distribution decreases with time. However, in contrast to the protons the electron spectra have steeper cutoffs due to effective synchrotron losses. Like in the case of protons, when stochastic re-acceleration is switched on, electrons form a peak at lower momenta, as shown in Figure 4.3(d). However, the spectral bump produced by stochastic re-acceleration is more pronounced in the case of electrons than that of protons. The reason is the different injection criteria for the two particle species. Since we use the thermal leakage model, electrons and protons feature injection momenta differing by a factor of ~ 40 due to $p_{\rm inj,i} \propto \sqrt{m_i}$, as seen from Equation 4.19. In other words, we do not explicitly treat electron acceleration by, e.g., stochastic shock drift acceleration below 100 MeV (Katou and Amano, 2019), and subsume the entire acceleration from suprathermal to very high energies under DSA, as mentioned before. Electrons and protons at energies between the thermal peak and the injection threshold, which are a factor 4.45 higher in momentum, are considered part of the thermal bulk and are ignored. The electrons between their injection threshold and the proton injection momentum are very numerous, and with stochastic re-acceleration, they can form a larger bump in the particle spectrum

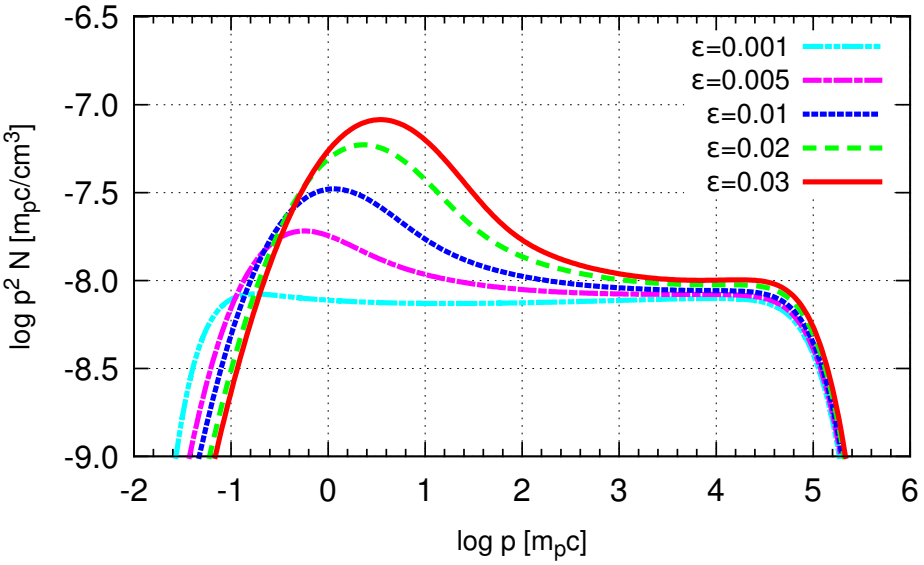

Figure 4.4: Proton spectra for different energy values transferred to fast-mode waves.

than would be observed for protons.

Next, we test how the particle spectrum is varying with energy, ϵ, transferred to the fast-mode waves. Figure 4.4 shows the resulting proton spectra for different values of ϵ. As expected, the contribution from stochastic re-acceleration is more visible with larger energy available for this process. The more energy is converted to the turbulence, the larger peak in the particle spectrum can be formed because the particles undergo the re-acceleration process for longer time periods before the energy is exhausted.

Having established in Chapter 3 that stochastic re-acceleration of electrons is able to soften the radio spectrum of an SNR, we additionally investigate here if the impact of stochastic acceleration can be visible in hadronic emission. Figure 4.5 shows γ-ray flux from the proton spectra for different values of parameter ϵ. The pion bump for value $\epsilon = 0$ means basically that the stochastic re-acceleration is switched off and the emission is produced purely by the standard DSA. Figure 4.5 demonstrates that for the scenario that involves stochastic re-acceleration of protons γ-ray flux around 1 GeV is clearly enhanced compared to the standard case. Depending on the energy fraction transferred to the turbulence, the impact from stochastic re-acceleration is differently pronounced. As a result, for a sufficient energy transfer γ-ray spectrum between 1 GeV and 100 GeV is significantly softer than the standard DSA prediction. Thus, we conclude that besides the radio spectra of SNRs, stochastic re-acceleration can also be visible in the γ-ray energy range.

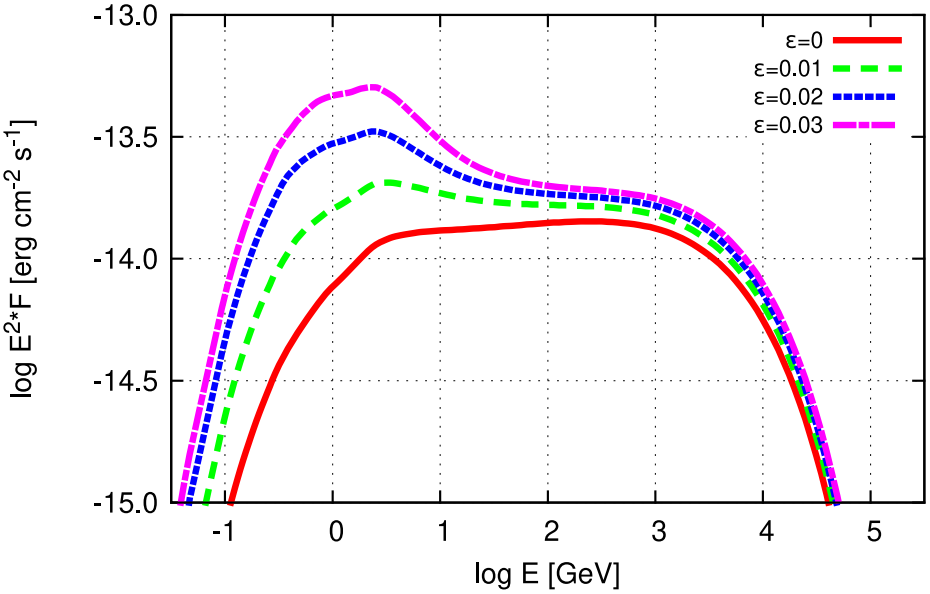

Figure 4.5: Hadronic emission for different energy values transferred to fast-mode waves.

Parts of this chapter have been published in
Abeysekara et al. 2020, ApJ 894, 51
(See table of publications)

Chapter 5

Cassiopeia A SNR

The work presented in this chapter was performed within the VERITAS collaboration, where I undertook the theoretical modeling of the Cassiopeia A SNR (hereafter Cas A). Analysis for the observed γ-ray data was provided by my collaborator Dr. Sajan Kumar (Abeysekara et al., 2020).

5.1 Overview

Cas A is a well-known SNR in the constellation Cassiopeia and one of the most powerful observed radio sources. It is one of the youngest SNRs, as its age is estimated to be $\sim$350 years (Fesen et al., 2006). The remnant is located in our Galaxy, at the distance $\sim 3.4^{+0.3}_{-0.1}$ kpc (Reed et al., 1995), featuring an angular diameter of $\sim 5'$. Most likely Cas A arose from a red supergiant star (Chevalier and Oishi, 2003; Lee et al., 2014; Weil et al., 2020) via a core-collapse Type IIb explosion (Krause et al., 2008a).

Photon emission from Cas A has been observed by numerous instruments and covers the range from low energy to γ-rays, including radio (Medd and Ramana, 1965; Allen and Barrett, 1967; Parker, 1968; Bell et al., 1975; Baars et al., 1977; Braun et al., 1987; Anderson et al., 1991; Kassim et al., 1995; Helmboldt and Kassim, 2009; DeLaney et al., 2014), optical (Reed et al., 1995), IR (Smith et al., 2009; DeLaney et al., 2010) and X-rays (Gotthelf et al., 2001; Uchiyama and Aharonian, 2008; Helder and Vink, 2008; Lee et al., 2014; Maeda et al., 2009; Grefenstette et al., 2015; Wang and Li, 2016; Arias et al., 2018). Cas A has been identified as a point-like source in γ-rays: by *Fermi*-LAT (Abdo et al., 2010; Yuan et al., 2013) at GeV and by HEGRA (Aharonian et al., 2001), MAGIC (Albert et al., 2007; Ahnen et al., 2017) and VERITAS (Acciari et al., 2010) at TeV energies. Due to the capacious amount of data, Cas A represents an ideal astrophysical test-bed for the study of CR acceleration and related phenomena.

The X-ray and radio detections, interpreted as synchrotron emission, attest production of high-energy electrons in Cas A. In contrast, the evidence for the proton acceleration is more delicate because the γ-ray photons can be alternatively provided by the energetic electrons via IC and NTB processes. Thus, the differentiation between the so-called "leptonic" and "hadronic" models is ambiguous. Nevertheless, as already mentioned in Section 2.4.4, hadronic and leptonic emission spectra reveal different shapes, which can

be used to distinguish between the two scenarios.

The latest models (Araya and Cui, 2010; Yuan et al., 2013; Zirakashvili et al., 2014; Saha et al., 2014; Ahnen et al., 2017) prefer a hadronic contribution for Cas A and tend to exclude a purely leptonic origin for the observed γ-ray emission. The corresponding proton spectrum does not show acceleration above TeV energies and hence suggest that Cas A could not be a PeVatron at its present age (Ahnen et al., 2017). An alternative scenario is, however, provided by Zhang and Liu (2019), who shows that specific assumptions for a two-zone model may allow for Cas A a proton cutoff around 3 PeV. The basic idea of Zhang and Liu (2019) is that the bulk of protons is accelerated by the fast-moving inward shocks detected by Sato et al. (2018), while the leptonic contribution is primarily provided by the forward shock. Thus, in this model, the forward shock is irrelevant for hadronic emission, while the small short-living inward shocks have to yield the main hadronic component by providing to protons the energy of the order 10^{50} erg. However, in models with realistic hydrodynamics the crucial role of reflected shocks for proton acceleration is not investigated yet.

In this chapter, the most recent broadband emission from Cas A is interpreted in the context of global hadronic and lepto-hadronic models. For this the recently analyzed γ-ray data from VERITAS and *Fermi*-LAT experiments (Abeysekara et al., 2020) are used. The VERITAS data were taken between 2007 and 2013 within 60 hours and cover the energy range between 200 GeV and 10 TeV. The 10.8 years of *Fermi*-LAT observations, performed from 4th August 2008 to 31st May 2019, provide the photon flux between 0.1 and 500 GeV. Additionally to the γ-ray, the radio and the X-ray data are taken into account.

The following modeling is performed using RATPaC, which was introduced in Chapter 4. However, it is important to stress that not all capabilities of RATPaC are exploited here. In fact, a time-independent one-zone model is applied for Cas A, where time-dependent DSA and stochastic re-acceleration of particles are not yet taken into account. Thus, we neither specify the exact acceleration mechanism nor the region where the CR are produced. Instead, a volume-averaged power-law proton and electron spectra with an exponential cutoffs are assumed. The reason for a rather simple model is the fact that it should primarily provide a quick interpretation for the recently analyzed VERITAS and *Fermi*-LAT data. Besides, in this thesis, the relatively simple model for Cas A serves additionally as a test for the complex program RATPaC.

5.2 Model assumptions

We build a global model to investigate the multi-wavelength spectrum from radio up to the TeV energy range. For simplicity, we assume a one-zone model fixed by two parameters: the ambient hydrogen number density, $n_{\rm H}$, and the post-shock magnetic-field strength, B. Both quantities are assumed constant, i.e., independent of time and location. The differential electron (proton) number densities, $N_{e(p)}$, are assumed to follow power law

with an exponential profile

$$N_i(p) = N_{0,i}\, p^{-s_i} \exp\left(-\frac{p}{p_{cut,i}}\right) , \tag{5.1}$$

with i denoting the particle species. Here p, p_{cut}, and s denote the electron (proton) momentum, the cutoff momentum, and the power-law index of the spectrum, respectively, all of which are free parameters of our model. The normalization, N_0, in principle reflects the injection efficiency of each particle species. As mentioned above, the SED is calculated with RATPaC. For the synchrotron emission from the nonthermal electron spectrum (Blumenthal and Gould, 1970), the modifications caused by the turbulent component of the magnetic field are taken into account (Pohl et al., 2015). For the IC interactions (Blumenthal and Gould, 1970), we consider two target photon fields: the CMB and the IR emission from the shock-heated ejecta with temperature $\sim 100\,\mathrm{K}$ and energy density $2\,\mathrm{eV\,cm^{-3}}$ (Mezger et al., 1986). Additionally, thermal bremsstrahlung from plasma electrons is included assuming local thermodynamic equilibrium (Hnatyk and Petruk, 1999). The γ-ray yield from protons via neutral-pion decay is computed using the procedure of Huang et al. (2007). Including the hydrogen number density and the magnetic field strength, we have in total nine independent parameters in our global model. The parameters are shown in Table 5.1. The hydrogen number density, n_H, corresponds to the upstream value and magnetic-field strength, B, to the downstream region. In the following, we consider two scenarios: a hadron-dominated model and a lepto-hadronic case, which we refer to as Model I and II, respectively.

Table 5.1: Model parameters for Cas A.

Varying parameters						Same for both models			
Model	B (μG)	$N_{0,e}$ $((\mathrm{m_e c})^{s_e-1})$	$N_{0,p}$ $((\mathrm{m_p c})^{s_p-1})$	$p_{cut,e}$ ($\mathrm{m_e c}$)	$p_{cut,p}$ ($\mathrm{m_p c}$)	s_e	s_p	T_e (10^7K)	n_H ($\mathrm{cm^{-3}}$)
I	450	4.2×10^{13}	3.2×10^{23}	9.0×10^6	2.1×10^4	2.5	2.17	1.8	1.0
II	150	2.9×10^{14}	3.8×10^{23}	1.6×10^7	6.0×10^3	2.5	2.17	1.8	1.0

5.3 Hadronic model

We start with a purely hadronic model of the γ-ray emission from Cas A. Assuming that γ-ray flux originates solely from proton-proton interactions, we can drastically reduce the number of free parameters in our model. Indeed, since the proton spectrum is independent of the magnetic field as well as thermal and nonthermal electron distributions, only four parameters affect the hadronic emission. The spectral index, s_p, and the cutoff momentum, $p_{cut,p}$, specify the spectral shape of the pion bump, while the ambient number density, n_H, and normalization factor $N_{0,p}$ determine the normalization of the flux. Furthermore, the ambient number density and normalization of the proton spectrum compensate each other, as can be seen from Equation 2.53. Therefore, the relevant

free parameters that we vary are s_p and $p_{cut,p}$, while normalization of the pion bump is fixed. Using Equation 5.1, we find the best fit for the joint *Fermi*-LAT and VERITAS data points (Abeysekara et al., 2020), shown in Figure 5.1. The corresponding best-fit parameters, with $\frac{\chi^2}{d.o.f.} = 1.38$, are $s_p = 2.17$ and $p_{cut,p} = 2.1 \times 10^4\,\mathrm{m_p c}$ (equivalent to $E_{cut,p} \approx 21\,\mathrm{TeV}$). More instructive than the best-fit model are the confidence regions of

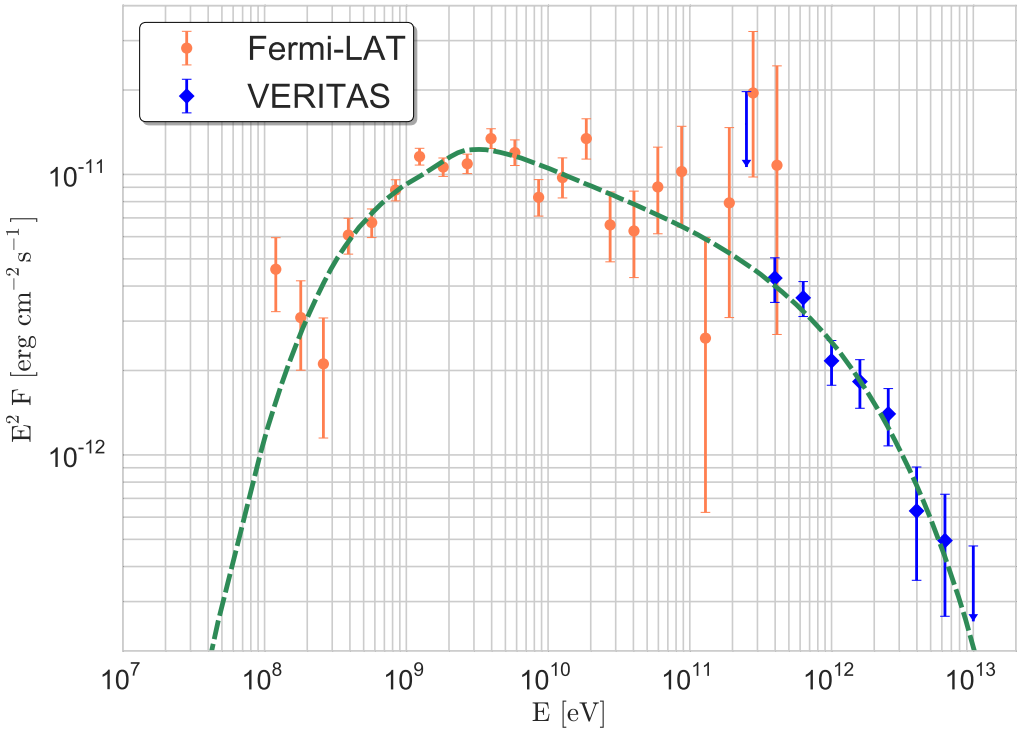

Figure 5.1: Purely hadronic best-fit with $\chi^2 = 36.01$ and $d.o.f. = 26$ ($\chi^2/d.o.f. = 1.38$). The corresponding best-fit parameters following Equation 5.1 are $s_p = 2.17$ and $p_{cut,p} = 2.1 \times 10^4\,\mathrm{m_p c}$.

the parameters, revealed by $\Delta\chi^2 = \chi^2 - \chi^2_{\mathrm{min}}$. Therefore, we scan the $s_p - p_{cut,p}$ parameter space and calculate $\Delta\chi^2$ while optimizing the normalization of the flux. The correct confidence regions with associated significance depend on the number of free model parameters, k (Lampton et al., 1976). The corresponding values are listed in Table 5.2. In our modeling $k = 2$ since the free parameters are s_p and $p_{cut,p}$, for which we estimate the 1σ, 2σ and 3σ confidence levels. The results are shown in Figure 5.2. Here the dark-blue area represents $\Delta\chi^2 < 2.30$, medium-blue $\Delta\chi^2 < 6.18$ and the light-blue $\Delta\chi^2 < 11.83$, which corresponds to 1σ, 2σ, and 3σ, respectively. As seen from Figure 5.2, the canonical solution from DSA theory ($s = 2.0$) is excluded with $> 99.7\%$ confidence. Thus, in the case of a hadronic origin, the γ-ray data mandate a proton spectral index ($s_p \approx 2.1 - 2.2$) softer than predicted by the standard DSA theory ($s = 2.0$) or nonlinear DSA ($s < 2.0$ at $p \gg mc$) (Malkov and Drury, 2001). Figure 5.2 indicates a cutoff with $p_{cut,p} \sim 10^4\,\mathrm{m_p c}$,

Table 5.2: Values of $\Delta\chi^2$ depending on numbers of fitting parameters k.

Significance	Confidence level	$\Delta\chi^2$		
		$k=1$	$k=2$	$k=3$
0.317	68.3% "1σ"	1.0	2.3	3.53
0.0455	95.45% "2σ"	4.0	6.18	8.02
0.0027	99.73% "3σ"	9.0	11.83	14.16
0.00006	99.99% "4σ"	16.0	19.33	22.06

in full agreement with Ahnen et al. (2017), who concluded that Cas A is not a PeVatron. It is important to recall here, though, that these conclusions are made within a one-zone model with an exponentially cutoff power-law spectra. Relaxing these assumptions can slightly change the confidence regions.

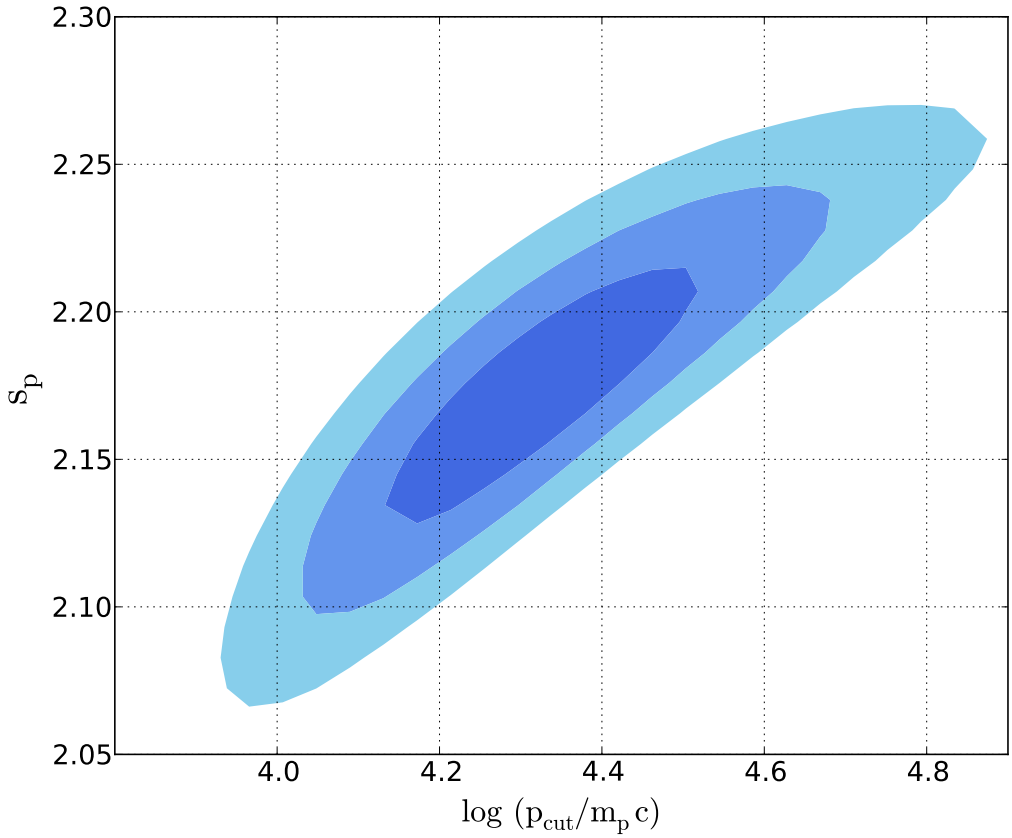

Figure 5.2: Purely hadronic model: The confidence regions for the spectral index, s, and cutoff momentum, p_{cut}. The dark-blue area corresponds to 68.3% probability, or 1σ, medium-blue to 95.5%, or 2σ, and the light-blue field to 99.7%, or 3σ, respectively.

In the next step, we determine the electron spectrum for the global model of broadband emission. The electron power-law index, $s_e \approx 2.5$, is entirely fixed by the radio data (Vinyaikin, 2014), and the X-ray flux (Maeda et al., 2009) is well explained by the synchrotron cutoff. A minor discrepancy occurs above 100 keV where the *INTEGRAL* spectral data (Wang and Li, 2016) suggest a spectral hardening, which might reflect an asymmetric explosion (Wang and Li, 2016) and thus cannot be included in our modeling. An alternative explanation involves weakly relativistic electrons emitting NTB, as we discuss in Section 5.4.

Lee et al. (2014) found that the upstream gas density for Cas A lies in the range 0.6 to 1.2 cm^{-3}. In this work, we follow Lee et al. (2014) and use $n_\mathrm{H} = 1.0\,\mathrm{cm}^{-3}$ for simplicity. In order for the IC component not to dominate the γ-ray production from hadrons, the magnetic field in the downstream region needs to be at least $\sim$450 μG, and we use this minimum value in the model. This magnetic-field strength is compatible with the results of Berezhko et al. (2003), Zirakashvili et al. (2014), and Sato et al. (2018), who argued that for Cas A, $B \sim 0.5 - 1\,\mathrm{mG}$. For a magnetic field this strong ($\sim$450 μG) the thickness of the X-ray rims must reflect synchrotron energy losses of the radiating electrons (Parizot et al., 2006).

The entire SED is presented in Figure 5.3, and the corresponding model parameters are summarized in Table 5.1 (Model I). The hadronic component (green dashed line) is the best-fit spectrum presented in Figure 5.1. Besides the marginal IC contribution, we obtain a negligible NTB component, which we calculate starting from 10 MeV. While the spectral shape of the electrons for energies above $\sim$100 MeV can be constrained by the radio data, there are no data to test the spectral shape for electrons with energies below $\sim$100 MeV. Consequently, accurate modeling of the NTB radiation below $\sim$10 MeV, which corresponds to $\sim$100 MeV electron energy, is not possible. Therefore, in our modeling the total photon spectrum disconnects between 100 keV and 10 MeV. The electron temperature, T_e, is chosen according to Maeda et al. (2009), and the thermal-bremsstrahlung emission provides a moderate contribution to the X-ray flux. The main reason for the rather insignificant thermal and NTB contributions is a relatively low plasma density in the downstream region given for a strong shock by $n_\mathrm{H,d} = 4n_\mathrm{H}$.

Finally, we test if the increasing γ-ray flux at $\sim$100 MeV can be explained by NTB. Indeed, at first glance the two lowest-energy Fermi data points suggest the presence of an additional emission besides the pion bump, such as NTB. Performing the χ^2-test after taking into account both NTB and neutral-pion decay, we find, however, that a negligible NTB contribution is preferred. The corresponding best-fit with $\frac{\chi^2}{d.o.f.} = 1.42$ is presented in Figure 5.4. Nevertheless, Cas A has been considered for a long time as the best candidate for detecting NTB (Cowsik and Sarkar, 1980; Allen et al., 2008). Therefore, we investigate the possibility of a lepto-hadronic model for the observed γ-ray spectrum of Cas A in the following section.

5.4 Lepto-hadronic model

In this section, we determine the observable limits on the presence of NTB and establish a model with a maximum possible NTB contribution. In contrast to the hadron-dominated

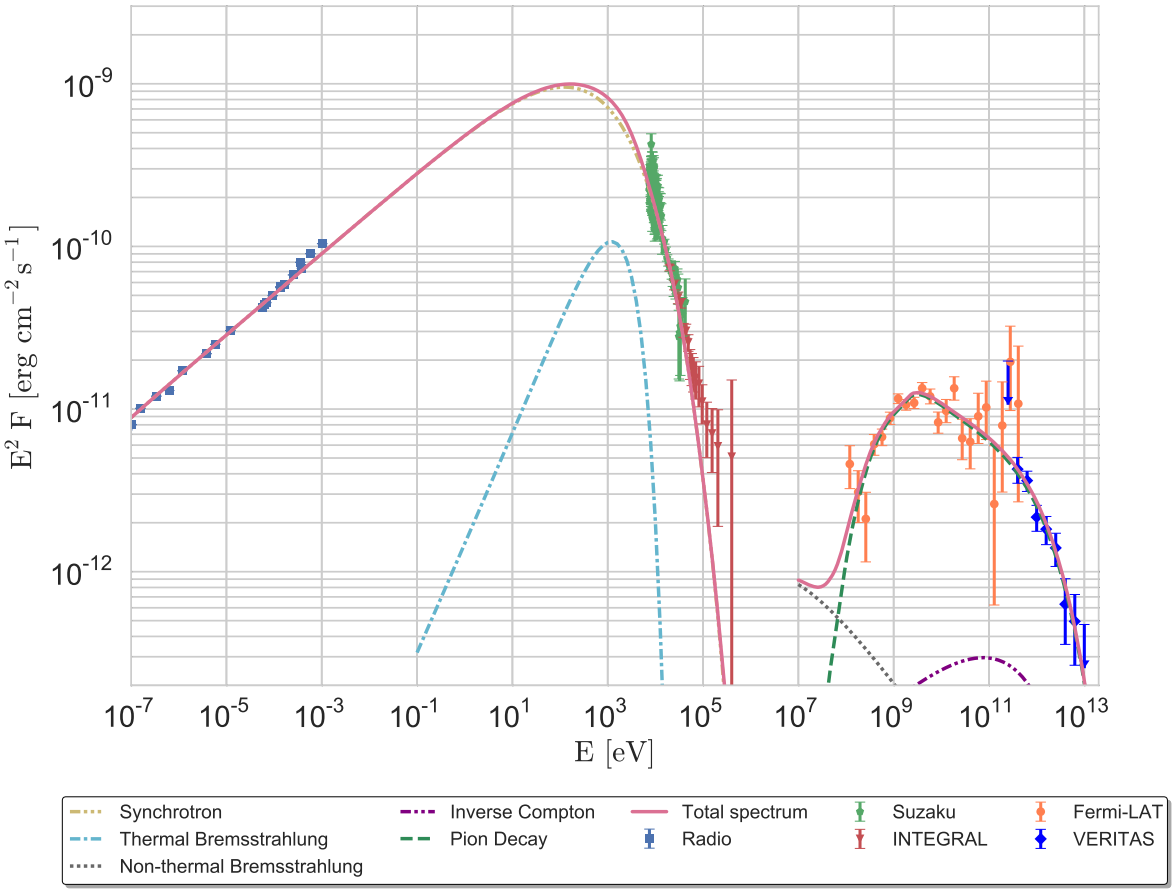

Figure 5.3: Model I: Hadronic model with downstream magnetic field $B \approx 450\,\mu$G and upstream gas density $n_H = 1\,\mathrm{cm}^{-3}$. The radio data are taken from Vinyaikin (2014); X-ray data from Maeda et al. (2009) and Wang and Li (2016).

model, where a χ^2-fit was applied to the γ-ray data, a fit by eye is used for the lepto-hadronic model. For a consistent lepto-hadronic scenario, IC and NTB components need to be additionally included and hence the entire SED has to be considered. However, a formal χ^2-fit and the corresponding interpretation for multiple instruments with different statistical and systematic errors is far more challenging. Furthermore, we are rather interested in a case with the minimum possible magnetic field inside Cas A, which provides the maximal (not best-fit) leptonic contributions.

In the framework of our one-zone model, NTB at a few hundred MeV is emitted by the same electrons that produce radio synchrotron emission at a few hundred MHz, and so a flux comparison between the radio data and the Fermi points at ∼100 MeV, $S_{1\,\mathrm{GHz}}/S_{100\,\mathrm{MeV}}$, determines the relation between the average gas density and the minimum

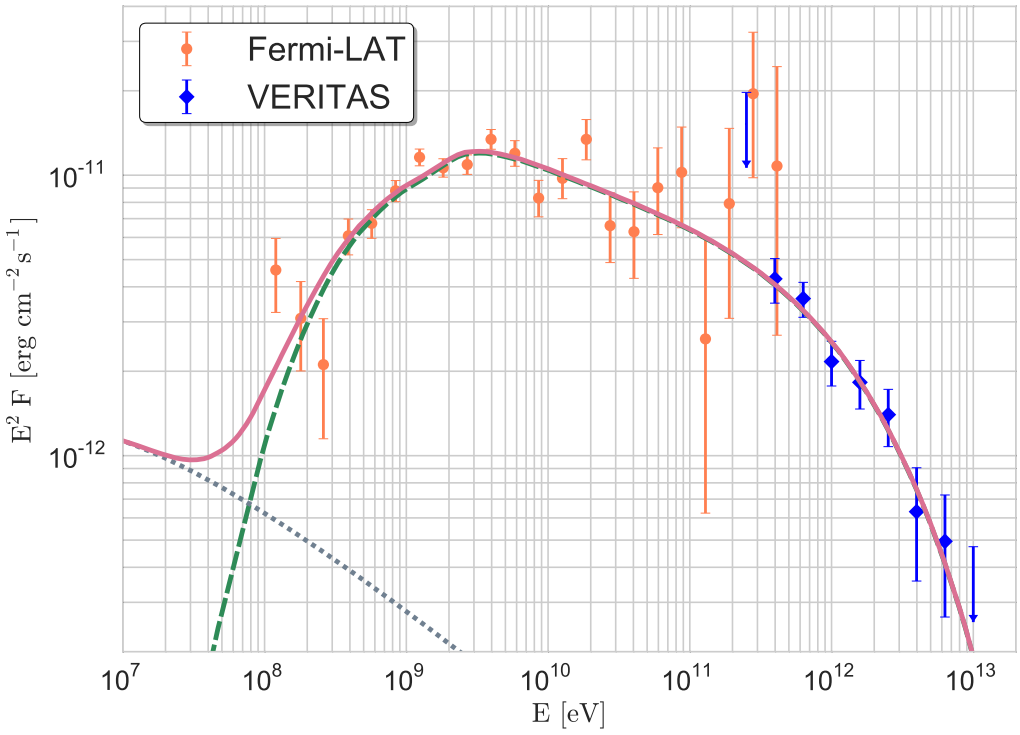

Figure 5.4: Best-fit for the hadronic component (green dashed line) plus NTB (blue dotted line); the total spectrum (pink solid line) with $\chi^2 = 35.50$ and $d.o.f. = 25$ ($\chi^2/d.o.f. = 1.42$).

magnetic-field strength. Choosing the pre-shock gas density according to Lee et al. (2014), $n_{\rm H} = 1.0\,{\rm cm}^{-3}$, we obtain for the minimum downstream magnetic-field strength: $B_{\rm min} \approx 150\,\mu$G. Any weaker magnetic field would lead to NTB overshooting of the data points at ∼100 MeV.

In general, the emission coefficients for synchrotron and NTB scale with magnetic-field strength and gas number density, respectively, as (cf. Section 2.4, see Equations 2.38 and 2.44 in particular)

$$j_{sy} \propto B^{\frac{1+s_e}{2}} \qquad \text{and} \qquad j_{ntb} \propto n_{\rm H}\,. \tag{5.2}$$

Therefore, to sustain constant synchrotron and NTB-flux ratio, the following condition for downstream magnetic field and ambient hydrogen number density has to be fulfilled:

$$\left(\frac{B}{150\,\mu{\rm G}}\right)^{\frac{1+s_e}{2}} = \left(\frac{n_{\rm H}}{1\,{\rm cm}^{-3}}\right)\,. \tag{5.3}$$

Aside from this case, the NTB component becomes suppressed with increasing magnetic

field but constant gas density. Starting from some critical magnetic-field value the overall γ-ray emission becomes hadron-dominated, as discussed in Section 5.3. The minimum post-shock magnetic field for Cas A is therefore given by

$$B \gtrsim 150\ \mu\mathrm{G} \left(\frac{n_\mathrm{H}}{\mathrm{cm}^{-3}}\right)^{\frac{2}{1+s_e}} , \tag{5.4}$$

as can be recognized from Equation 5.3. The minimum magnetic field deduced from potential NTB contribution depends on the ambient density of the remnant. Thus the density uncertainties provided by Lee et al. (2014) suggest that the minimum magnetic-field value may vary from 110 μG to 170 μG.

Having established the strength of the magnetic field inside Cas A, we immediately find several consequences. First, given the age of the remnant, $\sim 10^{10}$ s, only electrons with Lorentz factors $\gamma \gg 10^6$ can be affected by energy losses. The resulting IC peak, which is calculated from a combination of CMB and far-IR target-photon fields, would lie near 100 GeV in the spectrum, and its spectral shape would be incompatible with that measured in the GeV band. The second consequence is that the peak energy flux of the IC component must be about a factor $U_\mathrm{mag}/(U_\mathrm{cmb} + U_\mathrm{fir}) \simeq 250$ lower than that of the near-UV synchrotron emission radiated by the same electrons (Pohl, 1996). Consequently, the IC peak at 100 GeV is roughly a factor of 3 below the observed γ-ray flux and thus, IC emission alone can hardly provide the bulk of the γ-ray emission at 100 GeV. It does contribute to a significant part of it though, and the highest-energy TeV emission is fully accounted for by the highest-energy IC contribution. Both points indicate that an additional radiation component, such as from neutral-pion decay, is required. Therefore, we conclude that a purely leptonic model is very unlikely.

The lepto-hadronic case (Model II) with a maximum possible NTB component that is consistent with the Fermi data points is shown in Figure 5.5. The IC peak (purple dash-dot-dotted line) located at ∼100 GeV sets an additional constraint on the magnetic field inside Cas A. Decreasing the magnetic field would require higher electron injection to explain radio emission. In turn, it would enhance the IC contribution, which would exceed the TeV-flux measured with VERITAS (blue diamond-shaped points in Figure 5.5). Thus, both IC and NTB provide the same lower limit for the post-shock magnetic field, $\sim$ 150 μG. In contrast to NTB, IC does not scale with the gas density. Therefore, it provides an independent constraint on the magnetic-field value and implies that $B <$ 150 μG is highly unlikely for Cas A.

Despite a significant NTB contribution, γ-ray data in the GeV and higher MeV band are adequately explained by the pion bump and the discrimination between lepto-hadronic and purely hadronic models remains vague. Table 5.1 presents the parameters for the global lepto-hadronic model (Model II). The normalization factor, $N_{0,e}$, and the cutoff momentum of the electron spectrum, $p_{cut,e}$, are readjusted to fit the radio data for the weaker magnetic field. Since the cutoff at TeV energies is largely reproduced by the IC, the proton spectrum cuts off already at roughly 6 TeV. Alternatively, the hadronic contribution at TeV energies can be reduced by assuming the proton spectral index softer than 2.17.

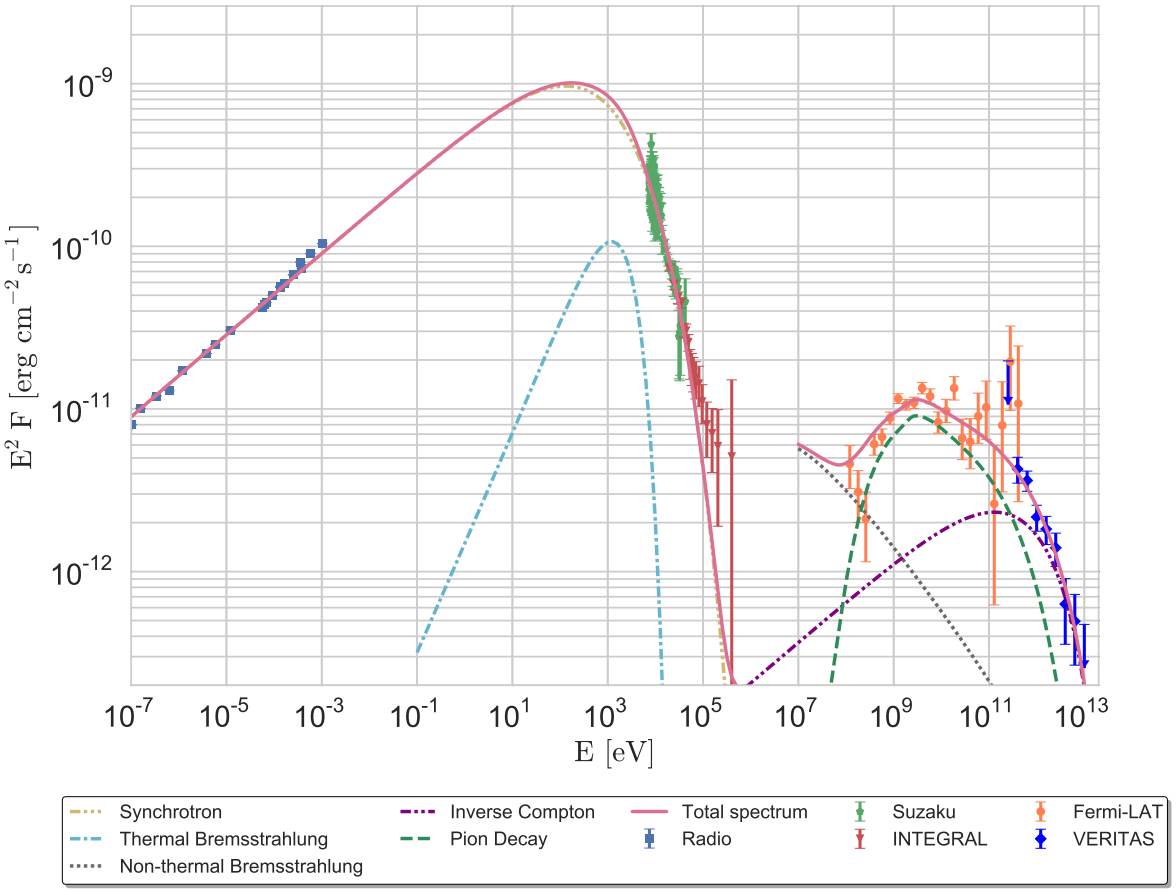

Figure 5.5: Model II: Lepto-hadronic model with a minimum post-shock magnetic field $B \approx 150\,\mu$G and ambient gas density $n_H = 1\,\mathrm{cm}^{-3}$. The radio data are taken from Vinyaikin (2014), X-ray data from Maeda et al. (2009), and Wang and Li (2016).

An advantage of the lepto-hadronic model is a possible explanation for the hardening of the X-ray spectrum above 100 keV observed with *INTEGRAL* (Wang and Li, 2016) by emission from non-relativistic electrons radiating NTB. This idea is supported by the findings of Allen et al. (2008), who analyzed the X-ray data of Cas A and concluded that in the energy range 10-32 keV, NTB exceeds the synchrotron radiation by a factor 2 to 3. A logical extrapolation is that the non-relativistic electrons that are not in thermal equilibrium can provide a significant NTB contribution in the range of 100 keV - 1 MeV and thus explain the hard X-ray spectrum. As mentioned above, we do not model this explicitly because we lack the exact form of the electron spectrum at lower energies.

5.5 Discussion

The observed radio spectrum of Cas A constrains the spectral index of the electrons to be $s_e \approx 2.5$, and the γ-ray data favor a proton spectrum of $s_p \approx 2.17$. These values are obviously softer than predicted by DSA. One possible explanation involves effects arising from turbulence growth and damping (Malkov et al., 2011; Brose et al., 2016). Alternatively, quasi-perpendicular shocks in young SNRs can steepen the spectral index (Bell et al., 2011). In the case of a young core-collapse SNR like Cas A, the hydrodynamical structure of the progenitor wind zone and acceleration at the reverse shock can significantly modify the particle spectra (Atoyan et al., 2000; Telezhinsky et al., 2013; Zirakashvili et al., 2014). The detection of X-ray synchrotron radiation in the interior of Cas A suggests particle acceleration at the reverse shock (Gotthelf et al., 2001; Uchiyama and Aharonian, 2008; Helder and Vink, 2008). However, newer data indicate that essentially all of the > 15 keV synchrotron flux is produced in small knots located in the 3D interior of the remnant, rather than a surface like the reverse shock (Grefenstette et al., 2015). Finally, stochastic re-acceleration of electrons behind the forward shock may be able to soften the spectrum over three decades in synchrotron frequency (Pohl et al., 2015), discussed in detail in Chapter 3. In the present work, we follow a simple procedure to address the most important conclusions: determination of the minimum magnetic field strength, confirmation of the pion bump, and the corresponding proton cutoff energy. More sophisticated models (including, e.g., asymmetric explosion, time-dependent hydrodynamic simulations, acceleration at the reverse shock, magnetic turbulence, and stochastic re-acceleration of particles) are needed to further differentiate between competing scenarios concerning particle acceleration in SNRs.

The total CR energy for the hadron-dominated (Model I) and lepto-hadronic (Model II) models considered here is found to be $E_{\rm CR} \approx 1.7 \times 10^{50}$ erg and $E_{\rm CR} \approx 1.2 \times 10^{50}$ erg, respectively. These numbers roughly represent the total energy that went into the particles as they accumulated over the entire evolution time of the remnant. Unfortunately, there is no easy way to ascertain the original explosion energy of Cas A, $E_{\rm SN}$: the estimations vary between $2{\times}10^{51}$ erg and $5{\times}10^{51}$ erg (Laming and Hwang, 2003; Chevalier and Oishi, 2003; Schure et al., 2008; Lee et al., 2014; Orlando et al., 2016). This suggests that the fraction of the explosion energy expended in accelerating particles is between 2% and 9%. Being a very young SNR, Cas A is very likely in the ejecta-dominated phase (Morse et al., 2004), implying that only a fraction of its explosion energy can be currently extracted from the

shock. The full energy becomes available after the SNR enters the Sedov-Taylor stage. In that case, the above numbers may not accurately indicate the acceleration efficiency of the remnant. Truelove and McKee (1999) suggested that Cas A is in the transition from the ejecta-dominated to the Sedov-Taylor stage. To verify this, we follow calculations in Dwarkadas (2013), who assumed that Cas A is still in the free-expansion phase and expands into a wind with density profile $\rho \propto r^{-2}$. According to Dwarkadas (2013) the maximum shock energy that is available for particle acceleration is found to be:

$$E_{\rm acc} = \frac{2\pi m^3}{(3m-2)} \frac{\rho_{\rm u} R_{\rm sh}^5}{t_{\rm age}^2} \qquad \text{with} \qquad m = \frac{(n-3)}{(n-2)} \,. \tag{5.5}$$

Here $\rho_{\rm u}$ is pre-shock gas density, $R_{\rm sh}$ is shock radius, and $t_{\rm age}$ is age of the remnant. The expansion parameter, defined as $m = d\ln R_{\rm sh}/d\ln t$, is fixed by the ejecta-density profile, $\rho_{\rm ej} \propto r^{-n}$, with $n > 5$ (e.g., Chevalier (1982)). A reasonable value for n is given by Matzner and McKee (1999), who find that a red supergiant star with a radiative envelope has $n \approx 10$. Assuming this ejecta profile and taking typical values for Cas A: $R_{\rm sh} = 2.5$ pc, $\rho_{\rm u} = 2.34\times10^{-24}\,{\rm g\,cm^{-3}}$ and $t_{\rm age} = 350$ years, we obtain the maximum shock energy available at $E_{\rm acc} \approx 3.5 \times 10^{51}$ erg. This result shows that the maximum energy available for particle acceleration in the ejecta-dominated phase is of the same order as the total explosion energy of Cas A, $E_{\rm SN} \approx 2 \times 10^{51} - 5 \times 10^{51}$ erg, that is presented in literature (Laming and Hwang, 2003; Chevalier and Oishi, 2003; Schure et al., 2008; Lee et al., 2014; Orlando et al., 2016). This indicates that a large fraction of the explosion energy is available at the shock front. Therefore, Cas A is not far from the Sedov-Taylor stage. Our estimation of $2\% - 9\%$ of explosion energy is thus appropriate. Further, $E_{\rm acc} \approx 3.5 \times 10^{51}$ erg implies that the acceleration efficiency (defined as $\eta_{\rm acc} = E_{\rm CR}/E_{\rm acc}$) is $\eta_{\rm acc} \approx 0.05$ and $\eta_{\rm acc} \approx 0.03$ for hadronic and lepto-hadronic scenarios, respectively. However, one should treat these conclusions with caution since the values we used for the parameters in Equation 5.5 are not precisely known. Our result is consistent with the total CR energy $\sim 9.9 \times 10^{49}$ erg presented by the MAGIC collaboration (Ahnen et al., 2017) and exceeds the value $\sim 4 \times 10^{49}$ erg found using *Fermi*-LAT (Yuan et al., 2013).

We find that IC and NTB obviously cannot account for the emission around 10 GeV, and thus a hadronic component is clearly needed. The maximum energies obtained for protons are 21 TeV and 6 TeV for the purely hadronic and lepto-hadronic models, respectively. These values are similar to the previous results of Yuan et al. (2013) (10 TeV) and Ahnen et al. (2017)(12 TeV).

5.6 Summary for modeling of Cas A

Considering the entire multi-wavelength spectrum of Cas A, we used a global one-zone model assuming power-law particle spectra with an exponential cutoff. Two different scenarios, a hadron-dominated case (Model I) and a lepto-hadronic model (Model II) are presented. Furthermore, in agreement with previous studies on the SED of Cas A (Araya and Cui, 2010; Saha et al., 2014); a purely leptonic model is excluded under the assumption of a one-zone scenario, leading to the conclusion that proton acceleration up to TeV energies is clearly evident. Nevertheless, our modeling indicates that Cas A is

highly unlikely a PeVatron. This result is in full agreement with Ahnen et al. (2017). The resulting pion bump reflects a slightly softer spectral index for the proton spectrum, $s_p \approx 2.17$, than the canonical DSA predictions (both linear and nonlinear versions (Malkov and Drury, 2001)). We exclude the canonical DSA solution of $s = 2.0$ with 3σ confidence. The total energy converted into CR is at least 10^{50} erg, giving an acceleration efficiency $\eta_{\rm acc} \approx 0.03 - 0.05$.

Although Cas A is the best SNR candidate for NTB emission (Cowsik and Sarkar, 1980; Allen et al., 2008), we cannot indicate any evidence for an NTB flux above 100 MeV. A clear determination may be achieved with the photon measurements extended down to the MeV energy range. Future experiments, such as AMEGO[1], may shed light on that issue. Nevertheless, assuming a potential NTB presence in Cas A, we deduce a minimum value for the magnetic-field strength inside the remnant $B_{\rm min} \approx 150\,\mu$G. This value is independently confirmed by the IC peak. Therefore, it is clear that the magnetic field inside the Cas A SNR is efficiently amplified, when compared to the ISM field.

[1] All-Sky Medium Energy Gamma-ray Observatory: https://asd.gsfc.nasa.gov/amego/

Parts of this chapter have been published in
Wilhelm et al. 2020, A&A 639, A124
(See table of publications)

Chapter 6

Tycho's SNR

6.1 Motivation

Tycho's SNR is associated with the historical supernova event SN 1572 of Type Ia, first described by Tycho Brahe. Thanks to his visual observation, the age of Tycho's SNR (SNR G120.1+1.4, hereafter Tycho) is accurately determined to be ~ 448 years. Along with Cas A, Tycho is one of the best studied young SNRs. Tycho originated from a Type Ia supernova (Krause et al., 2008b) and is assumed to have canonical explosion energy of $\sim 10^{51}$ erg. These details, together with the available broadband spectrum, make Tycho one of the best astrophysical laboratories to study particle acceleration. Nevertheless, several questions still remain unanswered.

As already discussed before, despite the success of DSA theory, it fails to explain the observed radio spectrum S_ν for all SNRs. Also Tycho is no exception, its measured radio spectral index $\alpha \approx -0.65$, with $S_\nu \propto \nu^\alpha$ (Kothes et al., 2006), deviates from the standard DSA prediction $\alpha \approx -0.5$. This discrepancy is generally accounted for using the concept of Alfvénic drift (Bell, 1978a). Hence, various authors postulate Alfvénic drift only in the upstream region (Völk et al., 2008; Morlino and Caprioli, 2012) or in the upstream and downstream (Slane et al., 2014) regions of Tycho's forward shock. The proper motion of CR scattering centers that proceed with Alfvén speed is assumed to decrease the compression ratio felt by the particles, thereby causing a softening of their spectra. To be more precise, the effective compression ratio seen by particles is (cf. Section 2.5.1)

$$r_{\mathrm{eff}} = \frac{u_1 + H_{c1} v_{\mathrm{A1}}}{u_2 + H_{c2} v_{\mathrm{A2}}}\,, \tag{6.1}$$

where u_1, v_{A1} are the plasma velocity and the Alfvén velocity in the upstream and u_2, v_{A2} in the downstream regions, respectively. The relative direction of the propagation of the Alfvén waves in the upstream (downstream) is reflected by the cross helicity, $H_{\mathrm{c1(2)}}$. In the above global models, its value is chosen rather freely, in order to reduce the effective compression ratio and thereby to account for the soft particle spectrum. For example

Völk et al. (2008) and Morlino and Caprioli (2012) take $H_{c1} = -1$ and $H_{c2} = 0$, while Slane et al. (2014) use $H_{c1} = -1$ and $H_{c2} = 1$. However, on closer inspection the concept of Alfvénic drift as an explanation for the spectral softening appears misleading.

First of all, Vainio and Schlickeiser (1999) performed a detailed calculation on self-consistent transmission of the Alfvén waves through the shock and found that the presence of waves results in harder particle spectra than predicted by the standard theory (meaning that Alfvén waves infer exactly the opposite effect to that claimed by Völk et al. (2008), Morlino and Caprioli (2012) and Slane et al. (2014)). The reason is that Alfvén waves that move in the upstream region in the opposite direction to the background plasma ($H_{c1} = -1$) propagate also predominately in the opposite direction in the downstream ($H_{c2} \approx -1$)(Vainio and Schlickeiser, 1999). Therefore, even despite the modifications induced by the strong magnetic-field pressure, the effective compression ratio seen by particles (Equation 6.1) exceeds the standard strong-shock value ($r_{\rm eff} > 4$). Investigating the impact of the Alfvénic drift within the framework of Vainio and Schlickeiser (1999), we find that for the Alfvénic Mach numbers, $M_{\rm A,1} \equiv u_1/v_{1,\rm A}$, in the range 10-13 (as presented in Völk et al. (2008) and Morlino and Caprioli (2012)) the particle spectral index for a strong shock results in $s \approx 1.9$ instead of the $s \approx 2.3$ required by radio observations of Tycho. Furthermore, the negative downstream helicity, $H_{c2} \approx -1$, predicted by Vainio and Schlickeiser (1999) is exactly the opposite of what was assumed by Slane et al. (2014), who used $H_{c2} = 1$.

Secondly, according to Morlino and Caprioli (2012) the Alfvénic-drift phenomenon in the global models of Tycho is referred as resulting from the nonresonant streaming instability of CR (Bell, 2004). According to Bell (2004), the phase speed of the nonresonant modes is negligible compared to the shock velocity. But in the case of Alfvénic drift, the Alfvén velocity required to account for Tycho's radio spectra has to be enormous.

The following estimation should demonstrate the corresponding discrepancy. Let us assume that Alfvénic drift occurs only in the upstream region ($H_{c2} = 0$ and $H_{c1} = -1$), as in Völk et al. (2008) and Morlino and Caprioli (2012), even though it contradicts the findings of Vainio and Schlickeiser (1999). In this case, we can rearrange Equation 6.1 to

$$M_{\rm A,1} = (1 - r_{\rm eff}/r_{\rm sh})^{-1}\,, \tag{6.2}$$

where $r_{\rm sh} \equiv u_1/u_2$ is the gas compression ratio of the shock. The sub-shock compression ratio (defined in Section 2.5.2) in Völk et al. (2008) and Morlino and Caprioli (2012) is in the range $R_{\rm sub} = 3.7 - 3.9$, even if the nonlinear effects of the DSA are included. The effective compression ratio seen by particles, required by the radio observations is $r_{\rm eff} \approx 3.3$. Inserting these values into Equation 6.2 provides a relatively low Alfvénic Mach number, $M_{\rm A} = 6 - 9$, making it clear that the Alfvén speed exhibits a significant fraction of the shock velocity. Therefore, to explain Tycho's radio data with Alfvénic drift, the Alfvén phase speed has to attain $11\% - 16\%$ of the shock velocity. Obviously, this value is in conflict with the phase speed of the nonresonant mode, $v_\phi \approx 0$, as described by Bell (2004). Therefore, Alfvénic drift in the models for Tycho cannot be associated with the nonresonant streaming instability.

It is important to note here that Völk et al. (2008) and Morlino and Caprioli (2012) applied in their modeling somewhat smaller magnetic-field values than required to best match the radio data with Alfvénic drift. The post-shock magnetic fields of $\sim 300\,\mu$G (Morlino and Caprioli, 2012) and $\sim 400\,\mu$G (Völk et al., 2008) provide sufficient flux in the radio range but fit the spectral shape of the observed data only moderately well. The Alfvén velocity in these models (with corresponding Alfvénic Mach numbers of $M_{\rm A} \approx 13$ and $M_{\rm A} \approx 10$) is still $\sim 10\%$ of the shock velocity. The phase speed of the nonresonant mode is much less than that and cannot support Alfvénic drift.

A post-shock magnetic field above $\sim 300\,\mu$G, when combined with the relatively low ambient density of $0.3-0.4\,{\rm cm}^{-3}$ (Völk et al., 2008; Morlino and Caprioli, 2012), becomes dynamically important[1]. The corresponding magnetic-field pressure will affect the shock compression ratio, which results in $r_{\rm sh} < 3.9$. Aside from the work of Morlino and Caprioli (2012), this effect has been neglected in global models for Tycho.

The above arguments illustrate that the Alfvénic-drift concept is unable to explain Tycho's soft radio spectrum consistently. An alternative way to explain the softening of the particle spectra in collisionless shocks to account for neutral hydrogen in the surrounding medium, first proposed by Blasi et al. (2012). Analytic calculations from Ohira (2012) plus later simulations (Ohira, 2016) show that neutrals can leak from the downstream into the upstream region and modify the shock structure. This results in a softer particle spectrum as produced by standard DSA. Morlino and Blasi (2016) build on that idea to model the rather soft γ-ray spectrum of Tycho. However, the leakage of neutral particles is significant for shock velocities $V_{\rm sh} < 3000\,{\rm km\,s}^{-1}$ (Ohira, 2012), which is considerably below the value ascertained for Tycho. Morlino and Blasi (2016) argued that certain regions of Tycho can feature slower shocks that propagate into dense, partially neutral material. Obviously, in this scenario, regions with slower shock velocities would have to provide nearly all of the observed overall emission, while contributions from the regions with the fast shock velocities would have to be weak, otherwise the integrated emission would reflect the hard spectra expected for fast shocks in an ionized medium.

In this work, we suggest a new approach: besides standard DSA, we consider an additional acceleration process, namely the stochastic re-acceleration of particles in the immediate post-shock region of the SNR, as presented in Chapter 3. It has been shown that fast-mode waves that survive the TTD by the background plasma are efficient modes to accelerate charged particles via cyclotron resonance (Yan and Lazarian, 2002; Liu et al., 2008). In previous chapters of this thesis, it was demonstrated that particles may be stochastically re-accelerated by fast-mode turbulence, which occurs in the downstream region, after escaping from the forward shock. Here, we further build on that idea and incorporate it into detailed modeling of Tycho.

Fast-mode turbulence may arise behind the shock from velocity fluctuations of the plasma flow, via, e.g., shock rippling (Giacalone and Jokipii, 2007), and build a thin turbulent region behind the blast wave. The width of this zone is regulated by the energy transfer from the background plasma into turbulence as well as damping induced by the re-acceleration of CR. We show that fast-mode turbulence that carries a few percent of the energy density of the background plasma in the downstream region is strong enough to

[1] In Section 6.3 we shall discuss it in more detail.

modify the spectrum of particles that have already been accelerated by the shock. Thus, in our treatment, stochastic acceleration and DSA operate together and produce a particle spectrum consistent with the observed radio spectral index. An additional advantage of our approach is that it is fully time dependent[2]. We solve the *time-dependent transport equation* for CR that contains a DSA term and diffusion in momentum space and is coupled to hydrodynamic simulations.

Another interesting question regarding Tycho pertains to the extent to which the magnetic field is amplified inside the remnant. A relatively high post-shock magnetic field, $300 - 400\,\mu$G, is postulated by several global models (Völk et al., 2008; Morlino and Caprioli, 2012). One of the reasons is the aforementioned Alfvénic drift, which demands relatively large magnetic-field values to account for the radio spectrum. Since we do not postulate any Alfvénic drift in our model, our approach of inferring the magnetic-field strength is an alternative to that of previous works on Tycho.

A major argument for a high magnetic field downstream of Tycho are the observed narrow nonthermal X-ray filaments (Hwang et al., 2002; Parizot et al., 2006; Helder et al., 2012). Since electrons can only propagate for a finite distance before they lose their energy due to synchrotron radiation, the rim widths may reflect the magnetic-field strength in the immediate downstream of the SNR. An alternative scenario is provided by damping of the turbulent magnetic field in the interior of the remnant (Pohl et al., 2005; Ressler et al., 2014; Tran et al., 2015), in which the narrowness of the nonthermal rims can be explained by the damping of the turbulently amplified magnetic field. Like for other SNRs, also for Tycho a distinction between these two scenarios by means of the energy dependence of X-ray filaments is difficult (Rettig and Pohl, 2012; Tran et al., 2015; Sushch et al., 2018). Magnetic-field damping is widely considered as the scenario that allows for a weak magnetic-field strength inside SNRs. Nevertheless, Tran et al. (2015) find that in either case the minimum downstream magnetic-field value inferred from Tycho's nonthermal filaments is at least $\sim 20\,\mu$G. Assuming that the electron acceleration is limited by the age of the remnant, the work from *NuStar* collaboration (Lopez et al., 2015) estimates $\sim 30\,\mu$G for the downstream magnetic field. However, the majority of studies cited above favor the loss-limited interpretation for particle acceleration in Tycho. Furthermore, the most realistic limit is obtained from an analysis of the entire SED, which provides the minimal downstream magnetic field value of $\sim 80\,\mu$G (Acciari et al., 2011). Attempts to simultaneously fit the radio and the γ-ray data infer that any weaker magnetic field would cause an overproduction of γ-ray photons generated via IC scattering. Therefore, the question about the magnetic field value is automatically tied to the question of whether Tycho's γ-ray emission has a predominately leptonic or hadronic origin. The hadronic scenario has been strongly favored in the literature (Morlino and Caprioli, 2012; Zhang et al., 2013; Berezhko et al., 2013; Caragiulo and Di Venere, 2014; Slane et al., 2014), as opposed to a leptonic model (Atoyan and Dermer, 2012).

For our modeling, we start from the minimal magnetic field compatible with the entire SED. The evolution of the SNR, which is computed using hydrodynamic simulations,

[2]Time-dependent hydrodynamics for Tycho was already used by Slane et al. (2014). In their approach, however, a steady-state solution for DSA was used to numerically inject a specific CR spectrum at the location of the forward shock.

occurs in a medium with a constant density. We explicitly model the acceleration of each particle species in the test-particle limit, taking shock acceleration as well as stochastic acceleration in the downstream region into account, with both acceleration processes being time dependent. We explicitly model advection and diffusion of CR and take synchrotron losses for electrons into account. Furthermore, we consider the nonthermal radio and X-ray filaments and investigate whether they arise from extensive synchrotron losses or magnetic-field damping. For the study of the X-ray filaments, it is especially important to include diffusion of the particles, otherwise the distance that they propagate and thus the rim width would be underestimated. Since I started to work on Tycho in 2012 and used the observational data from roughly that time, the age of Tycho in our simulations is set to be 440 years. As a matter of course, the age difference of 8 years is insignificant for an SNR. Therefore, in the following to the age of Tycho is referred as 440 years.

This chapter is organized as follows: Section 6.2 describes the hydrodynamic picture for Tycho. In Section 6.4.1, we examine the model with the minimal amplified magnetic field compatible with the γ-ray observations. We justify the necessity for magnetic field damping that we introduce in Section 6.4.2. Therein we discuss our preferred model for Tycho and deduce a new theoretical minimum for the magnetic-field strength based on investigation of the multifrequency spectrum along with nonthermal filaments. The γ-ray spectrum of the resulting model comprises both hadronic and leptonic components. In Section 6.4.4, we discuss a potential possibility for a purely hadronic scenario with a strongly amplified magnetic field.

6.2 Hydrodynamics

To model Tycho, the hydrodynamic simulations performed by my collaborator Dr. Vikram Dwarkadas (private communication), are used. His evolutionary model of the remnant is generated by means of the VH-1 code (Blondin and Lundqvist, 1993), a 1-, 2-, and 3-dimensional finite-difference code that solves the hydrodynamic equations using the Piecewise Parabolic Method of Colella and Woodward (1984). An exponential density profile is chosen for the ejecta of Tycho since Dwarkadas and Chevalier (1998) demonstrated that it optimally approximates the density profile for a Type Ia supernova models compared to other distributions. Further, necessary parameters that determine the evolution of a Type Ia SNR are the ejected mass, the explosion energy, and the density of the ambient medium. For the ejecta mass we set the value typical for a Chandrashekhar mass, $1.4 M_{\odot}$, because Type Ia SNR is believed to originate due to thermonuclear deflagration and detonation of a white dwarf. For the energy of explosion we choose the canonical value of 10^{51} ergs.

Although the density around Tycho varies (Williams et al., 2013), as expected for such an extended structure, the remnant appears to expand in a relatively clean environment without any large inhomogeneities, such as molecular clouds (Tian and Leahy, 2011). Therefore, an explosion in a medium with a constant density provides a reasonable description for the dynamics of the remnant. The average ambient density varies in the literature, according to the method with which it was measured. X-ray measurements of the expansion rate suggest an ambient density of 0.2 - 0.6 cm^{-3} (Hughes, 2000).

Later X-ray observations based on proper-motion measurements of the forward shock and reverse-shocked ejecta in Tycho infer an upper limit of 0.2 cm^{-3} (Katsuda et al., 2010). X-ray observations of Cassam-Chenaï et al. (2007) reveal a lack of thermal emission in the post-shock region of Tycho, inferring an ambient density below 0.6 cm^{-3}. A low density of 0.2 cm^{-3} around Tycho is obtained by Williams et al. (2013), who determined the post-shock temperature from mid-IR emission of the remnant. On the other hand, efficient particle acceleration in SNRs can reduce the downstream temperature of the plasma (O'C. Drury et al., 2009), leading to a suppression of thermal emission and hence an underestimation of the ambient density. Higher values for the ambient density are additionally supported by the model of Dwarkadas and Chevalier (1998), who found that densities in the range of 0.6 - 1.1 cm^{-3} better match the X-ray observations of Tycho. Furthermore, Kozlova and Blinnikov (2018) and Badenes et al. (2006) favor a delayed detonation model with $\sim 1.0\,cm^{-3}$ for the X-ray morphology of Tycho. The density uncertainty of Tycho (0.2-1.0 cm^{-3}) is likewise reflected in the uncertainty in the distance to the remnant (see Hayato et al. (2010) for a review and Tian and Leahy (2011)), since both quantities are interdependent. For our modeling, we choose a value for the hydrogen number density of $n_{\rm H}$ =0.6 cm^{-3}, which gives a good fit to the observed shock radii and velocities.

Explosion energy, ejecta mass, and ambient density, together with the exponential density profile, form the suite of parameters necessary to model the complete hydrodynamical evolution of Tycho. Our simulations are spherically symmetric and are similar to those described in Dwarkadas and Chevalier (1998) and Telezhinsky et al. (2012a). The time-evolution of speed, radius, and temperature of the forward shock from our simulations is depicted in Figure 6.1. To note from the figure is that the plasma temperature falls from ∼600 keV at the very early stages to ∼30 keV at the current epoch. At 440 years, our simulations provide a forward shock radius $R_{\rm sh} \approx 3.5$ pc, which implies a distance to the remnant, $d \approx 2.9$ kpc. The velocity of the forward shock yields $V_{\rm sh} \approx 4100\,{\rm km\,s^{-1}}$. The position of the reverse shock, $\sim 0.69 R_{\rm sh}$, is in good agreement with the X-ray measurements of Warren et al. (2005). By contrast, the position of the CD, $R_{\rm CD} \approx 0.78 R_{\rm sh}$, falls below the value identified by Warren et al. (2005), who interpreted the closeness of the CD to the blast wave as evidence for the efficient back-reaction of CR. However, global models that incorporate NLDSA effects (Morlino and Caprioli, 2012; Slane et al., 2014) fail to reproduce the CD position for Tycho. The discrepancy for the CD position can be attributed to the decelerating CD being unstable to the Rayleigh-Taylor instability. Two-dimensional hydrodynamical simulations with the exponential profile show that Rayleigh-Taylor structures can extend almost halfway from the CD to the outer shock (Dwarkadas, 2000; Wang and Chevalier, 2001). Furthermore, Orlando et al. (2012) showed that Rayleigh-Taylor instabilities and ejecta fingers that extend far beyond the CD can misleadingly suggest that the CD is further out than its actual location. Therefore, we conclude that the position of the CD obtained in our model is quite reasonable.
According to our simulations, at the age of 440 years the remnant accumulated $\sim 3.8 M_\odot$ of ambient gas, indicating that in our modeling Tycho is in the transition between ejecta-dominated and Sedov-Taylor stages. The total thermal energy in the remnant at 440 years is $E_{\rm th} \approx 5.6 \times 10^{50}$ erg.

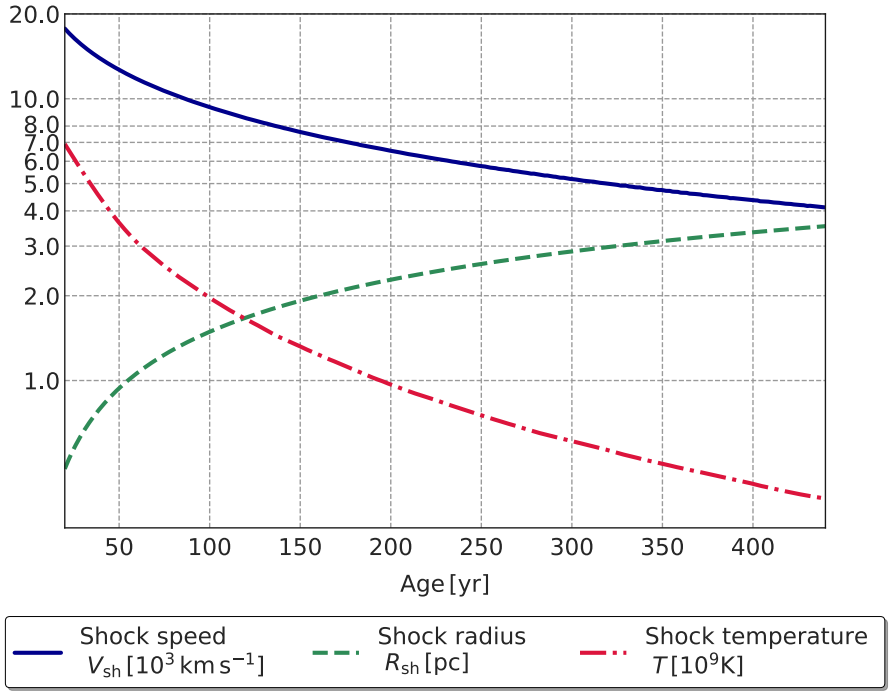

Figure 6.1: Shock speed (blue solid line), radius (green dashed line), and immediate post-shock temperature (red dotted line) as functions of time.

The shock profiles and velocity distribution from the simulation are used in the calculation for the particle acceleration described in Chapter 4.

6.3 Magnetic-field limit within RATPaC

Besides the CR feedback, the shock compression ratio can be affected by the magnetic pressure if a sufficient magnetic-field strength is present. However, dynamic feedback from magnetic-field pressure is not included in RATPaC yet. Therefore, we investigate the range where the impact of magnetic field on the shock structure remains negligible. We analytically solve the classical MHD equations for a plane-perpendicular shock in steady state, assume frozen-in plasma, and derive the dependency of the shock compression ratio on the magnetic-field strength.

For simplicity, we consider the plane-perpendicular shock in its rest-frame, as shown in Figure 6.2. In this scenario plasma-velocity component that is parallel to the shock front vanishes ($u_{||} = 0$ and $u_{\perp} = u$), while the magnetic-field orientation is parallel to the shock front normal ($B_{||} = B$ and $B_{\perp} = 0$). Unlike for a plane-parallel shock wave, presented in Section 2.3.3, for a perpendicular shock magnetic field may be dynamically

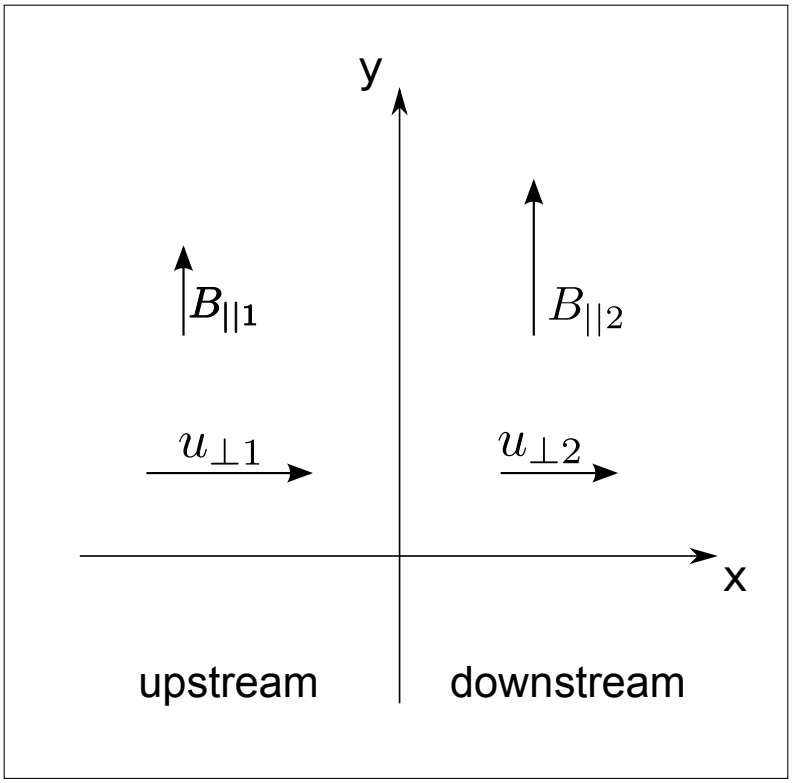

Figure 6.2: Schematic representation of a plane-perpendicular shock with a parallel magnetic component.

important since $B_{||}$ is compressed at the shock. General MHD equations (Appendix A) simplify in that case to the following relations

$$\rho_1 u_1 = \rho_2 u_2 \,, \tag{6.3}$$

$$\rho_1 u_1^2 + P_1 + \frac{B_1^2}{8\pi} = \rho_2 u_2^2 + P_2 + \frac{B_2^2}{8\pi} \,, \tag{6.4}$$

$$\frac{\gamma_a}{\gamma_a - 1}\frac{P_1}{\rho_1} + \frac{1}{2}u_1^2 + \frac{B_1^2}{4\pi\rho_1} = \frac{\gamma_a}{\gamma_a - 1}\frac{P_2}{\rho_2} + \frac{1}{2}u_2^2 + \frac{B_2^2}{4\pi\rho_2} \,. \tag{6.5}$$

$$B_1 u_1 = B_2 u_2 \,. \tag{6.6}$$

Here γ_a is the adiabatic index, u_1, ρ_1, P_1, B_1 are the plasma velocity, density, thermal pressure, and magnetic field in the upstream and u_2, ρ_2, P_2, B_2 in the downstream regions, respectively. Note that Equations 6.3 to 6.6 differ from the Rankine-Hugoniot conditions for purely hydrodynamic and plane-parallel shocks by the additional magnetic-pressure terms, $B^2/(8\pi)$, in Equation 6.4, as well as the heating terms, $B^2/(4\pi\rho)$, in the energy conservation Equation 6.5.

Defining the upstream plasma beta and the upstream Mach number, respectively

$$\beta_1 \equiv \frac{8\pi P_1}{B_1^2}\,, \qquad\qquad M_1 \equiv u_1\sqrt{\frac{\rho_1}{\gamma_a P_1}}\,, \tag{6.7}$$

one can obtain a parametrized cubic equation for the gas compression ratio $r_{\rm sh} \equiv \rho_2/\rho_1$:

$$\left(\frac{2(2-\gamma_a)}{\beta_1}r_{\rm sh}^2 + \gamma_a\Big((\gamma_a-1)M_1^2 + 2(1+\beta_1^{-1})\Big)r_{\rm sh} - \gamma_a(\gamma_a+1)M_1^2\right)(r_{\rm sh}-1) = 0\,. \tag{6.8}$$

The first trivial solution of Equation 6.8 is $r_{\rm sh} = 1$, which basically means that there is no shock. A physically relevant solution for us is provided by the remaining quadratic equation in the first brackets of Equation 6.8. Hence, the shock compression ratio can be simply expressed as a function of plasma beta, Mach number, and adiabatic index. Alternatively, we may introduce the Alfvénic Mach number, $M_{A,1} \equiv u_1/v_{\rm A,1}$, and use the relation

$$M_1^2 = \frac{2}{\gamma_a\beta_1}M_{A,1}^2\,. \tag{6.9}$$

The expression in the first brackets of Equation 6.8 becomes then

$$r_{\rm sh}^2 + [2M_{A,1}^2 + 5(1+\beta_1)]r_{\rm sh} - 8M_{A,1}^2 = 0\,. \tag{6.10}$$

For the squared Alfvén Mach number, it follows immediately from Equation 6.10

$$M_{A,1}^2 = \frac{r_{\rm sh}^2 + 5r_{\rm sh} + 5\beta_1 r_{\rm sh}}{2(4-r_{\rm sh})} \quad \overset{\beta_1\to 0}{=} \quad \frac{r_{\rm sh}^2 + 5r_{\rm sh}}{2(4-r_{\rm sh})}\,. \tag{6.11}$$

Here we used the fact that the typical environment of an SNR is a cold plasma, which provides a negligible upstream plasma beta. Figure 6.3 shows the shock compression ratio as a function of the upstream Alfvén Mach number, as given by Equation 6.11. To be noted from the figure is that the compression ratio of a shock strongly decreases with low Alfvén Mach numbers. For a fixed Mach number, Figure 6.3 illustrates the impact that magnetic field exercises on the shock. Furthermore, Figure 6.3 demonstrates that the dynamic feedback from magnetic field cannot be ignored for Alfvén Mach number roughly below ∼20, as the corresponding shock compression ratio is significantly below 4.

Next, we apply this calculation to Tycho and investigate the magnetic-field range valid for our modeling. We recall that the magnetic field in RATPaC is assumed to be isotropic in the upstream region, i.e., the individual components (one radial, $B_\perp$, and two tangential, $B_{||1}$, $B_{||1}$) are equal in their magnitudes ($B_\perp = B_{||1} = B_{||2}$). Thus, the

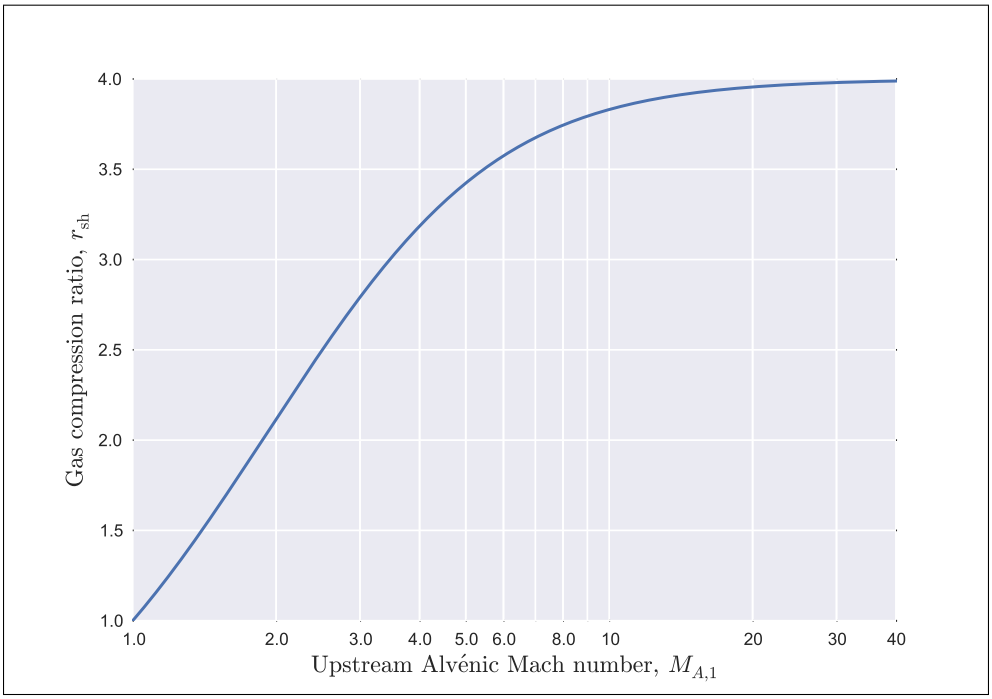

Figure 6.3: Shock compression ratio as a function of upstream Alfvén Mach number.

upstream and downstream magnetic-field strengths are given by relations

$$B_1 = \sqrt{\frac{3}{2}} B_{||}\,, \qquad\qquad B_2 = \sqrt{\left(\frac{1}{2} + r_{\rm sh}^2\right)} B_{||}\,, \tag{6.12}$$

where we introduced the total parallel component in the upstream region $B_{||}$, which is responsible for the magnetic pressure.

Apart from the magnetic field, the resulting gas compression ratio depends mainly on shock speed and upstream density, which in our model are $V_{\rm sh} \approx 4100$ km s^{-1} (at 440 years) and $n_{\rm H} = 0.6\,{\rm cm}^{-1}$ (see Section 6.2). Figure 6.4 presents shock compression ratio as a function of downstream magnetic field, where the hydrodynamic parameters for Tycho were taken. As the extensive magnetic-field pressure reduces the compression ratio of the shock, it consequentially softens the particle spectra. Hence, the corresponding particle spectral index deviates from the canonical DSA solution ($s = 2.0$) by Δs, resulting in $s = 2 + \Delta s$. The resulting radio spectral index, $\alpha = -0.5 + \Delta\alpha$, is accordingly modified by the value $\Delta\alpha = -\Delta s/2$. We choose $\Delta\alpha = -0.01$ (and thus $\Delta s = 0.02$) as the limit within which the magnetic-field pressure can be neglected because the corresponding changes are hardly visible in the radio spectrum when compared to the observed data. We find for the sonic upstream Mach number of $M_1 \approx 3500$, which corresponds to the hydrodynamic quantities we use in this work for Tycho that the magnetic field is dynami-

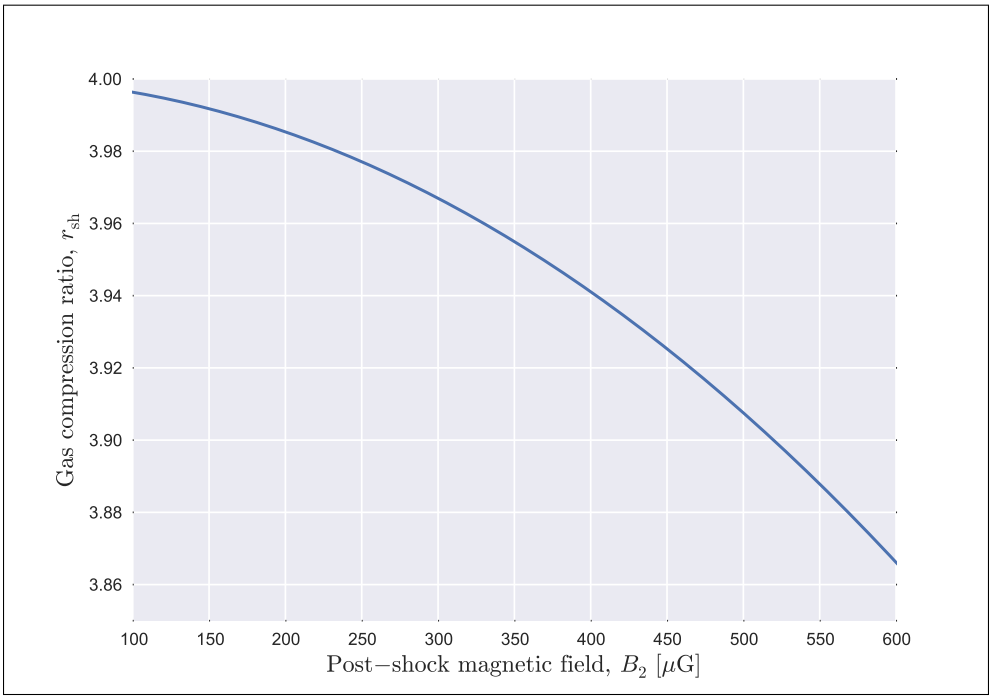

Figure 6.4: Shock compression ratio for Tycho as a function of the downstream magnetic-field strength.

cally unimportant for Alfvénic Mach numbers above $M_{\rm A,1c} \approx 17$. For lower Alfvénic Mach numbers, the deviation from the classical DSA solution exceeds the values of $s = 2.02$ and $\alpha = -0.51$ and hence cannot be neglected. Taking into account that the magnetic-field pressure is exerted only by the tangential components, we find the magnetic-field limits $B_{1,\rm max} \approx 120\,\mu$G for the upstream and $B_{2,\rm max} \approx 400\,\mu$G for the downstream regions, respectively. Any higher magnetic field would efficiently lower the shock compression ratio and produce particle spectra with $s > 2.02$ and radio spectra with $|\alpha| > 0.51$, and thus demand an MHD treatment. The particle spectrum deviation versus post-shock magnetic field for Tycho is shown in Figure 6.5.

6.4 Results

In contrast to previous attempts to model Tycho, we follow the full temporal evolution of the remnant starting at the age of 25 years. For conciseness, however, we show and discuss results for only the current age of Tycho, which for simplicity is taken to be 440 years. We find that the reverse-shock contribution to the particle spectrum in Tycho is negligible in the framework of our modeling at the age of 440 years (Telezhinsky et al., 2012a), in full agreement with Warren et al. (2005). Therefore it is not discussed further.

Given the low gas density, NTB (Blumenthal and Gould, 1970) yields too low a flux for it to be relevant, and so leptonic γ-ray emission is solely provided by IC scattering, for which we consider the CMB as the target photon field (Blumenthal and Gould, 1970;

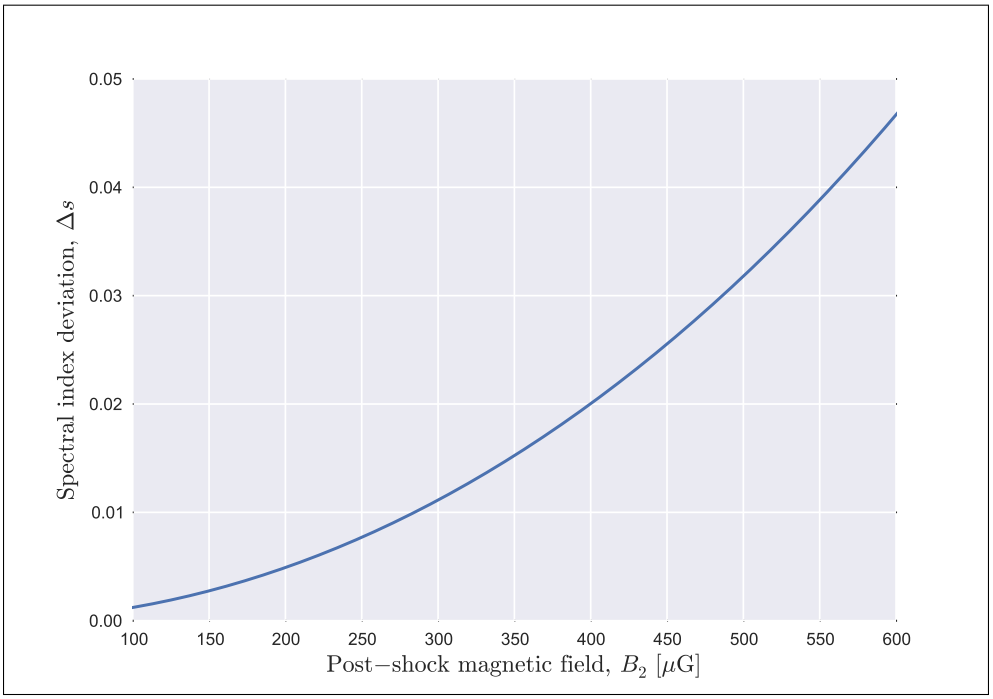

Figure 6.5: Deviation of the particle spectral index for Tycho as a function of the downstream magnetic-field strength.

Sturner et al., 1997). Tycho shows evidence for IR emission (Douvion et al., 2001). However, its contribution to the overall IC spectrum was found by Acciari et al. (2011) to be negligible.

We present two models for the multiwavelength emission of Tycho, which both adequately fit the SED. Model I allows for the weakest magnetic field in the immediate downstream region of the shock, $B_2 = 150\,\mu$G, which is compatible with the entire γ-ray flux observed with *Fermi*-LAT in GeV-range and VERITAS in TeV-band (Archambault et al., 2017). In Model I, the resulting γ-ray flux consists of both leptonic and hadronic components. The magnetic profile deeper inside the remnant is determined by advection of frozen-in magnetic field and corresponds to the MHD solution for negligible magnetic pressure and energy density (Equation 4.3). As we shall demonstrate, this model fails to explain radio and X-ray intensity profiles.

Therefore we present a second model, Model II, involving magnetic field damping and derive constraints on the magnetic field in Tycho. Generic technical details can be found in Section 6.4.1, where we introduce Model I: these also apply to the following sections listing the results for Model II.

6.4.1 Model I: Moderate advected magnetic field

The efficacy of stochastic acceleration is fully determined by three parameters: m, p_0, and the energy fraction of the plasma transferred to the turbulence, ϵ, which were introduced

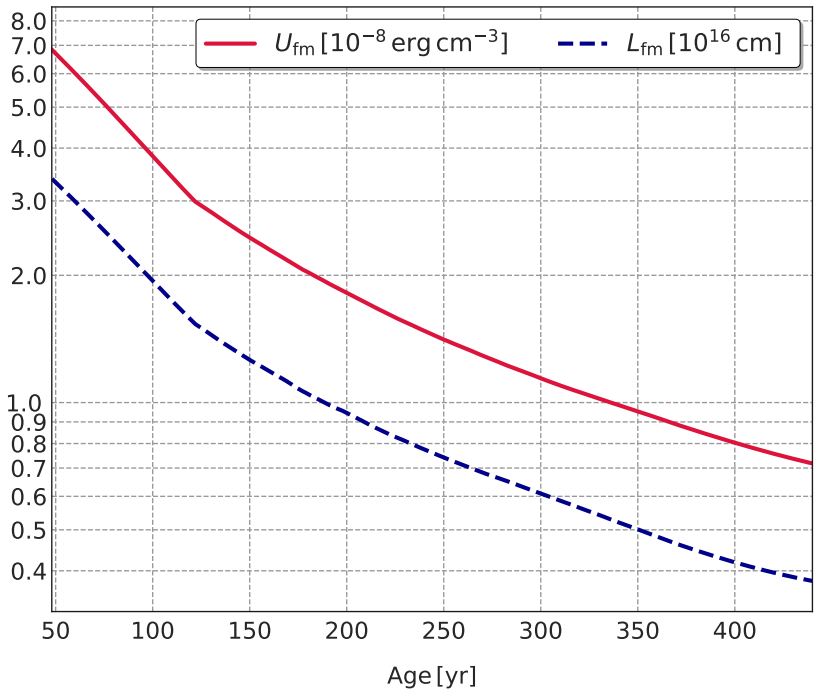

Figure 6.6: Energy density in fast-mode waves (red solid line) and width of the turbulent re-acceleration region (blue dashed line) as functions of time for Model I.

in Section 4.5. The acceleration time scale, $\tau_{\rm acc}$, and the width of the turbulent region, $L_{\rm fm}$, are then self-consistently calculated according to Equations 4.25 and 4.27. The parameter p_0 provides the critical limit up to which the momentum diffusion coefficient D_p is energy-independent (cf. Equation 4.21). We tested several values of p_0 and found that for $p_0 \gtrsim 10^{-3}\,m_{\rm p}c$ the resulting curvature of the radio synchrotron spectrum becomes too strong to remain in agreement with radio data. Therefore, in this work we adopt $p_0 = 9.3{\times}10^{-4} m_{\rm p}c$, which corresponds to electron energy of 500 keV. The power-law index, m, may vary up to 25% (to stay in agreement with observations) and can be compensated by a suitable choice of the energy-conversion factor, ϵ, implying that these quantities exhibit degeneracy to a certain degree. In the following calculations, we fix $m = 0.25$ and $\epsilon = 0.027$ (corresponding to 2.7% of the thermal energy density), which adequately reproduce the observed radio spectrum. The acceleration time scale is determined by the energy-conversion factor, which for $\epsilon = 0.027$ provides $\tau_{\rm acc} \approx 2.3$ yr.

The thickness of the region in which stochastic re-acceleration is operating is fairly small. For 2.7% of the thermal energy density of the post-shock plasma transferred to the turbulence, it results in $L_{\rm fm} \sim 10^{15} - 10^{16}$ cm, as illustrated in Figure 6.6. The width of the re-acceleration region decays with time as the SNR shock slows down, and thus the energy density in the turbulence decreases. At the age of 440 years, the width of

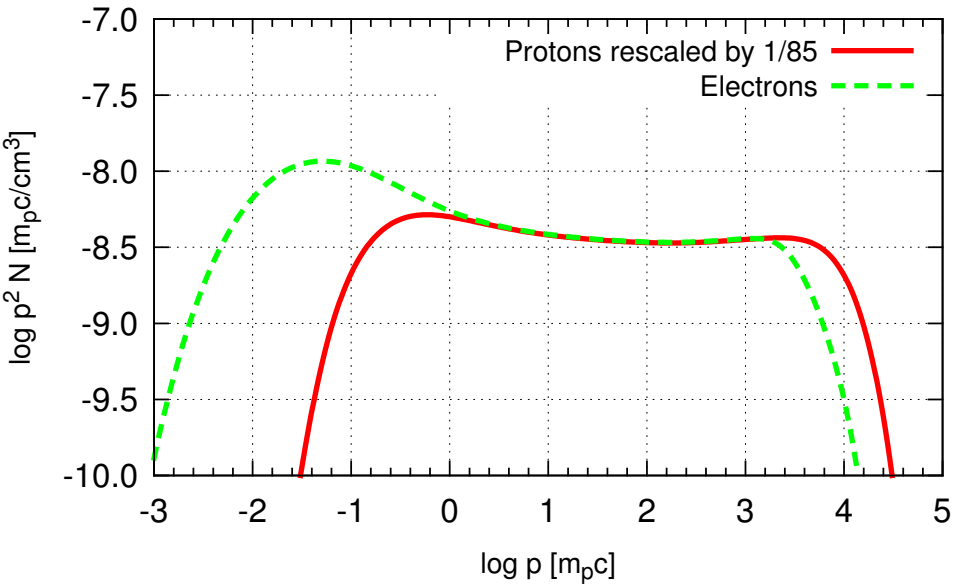

Figure 6.7: Number density of protons (red solid line) and electrons (green dashed line) for Model I involving weakest advected magnetic field with $B_2 = 150\,\mu$G. The proton number density is multiplied with the factor $K_{\rm e/p} = 1/85$.

the turbulent region comprises only $\sim 3 \times 10^{-4} R_{\rm sh}$. Still, the contribution to the particle spectra is substantial.

Figure 6.7 shows the differential number density for electrons and protons as obtained from solving Equation 4.5. For ease of exposition, the proton spectrum is rescaled by the electron-to-proton flux ratio, defined as $K_{\rm e/p} \equiv N_e/N_p \approx 1/85$. As a result of stochastic re-acceleration, the spectra strongly deviate from the canonical solution, $N \propto p^{-2}$, expected for DSA in the test-particle limit. For comparison, a standard case with stochastic re-acceleration turned off but the same remaining parameters is depicted in Figure 6.8. To be noted from Figure 6.7 are distinct bumps for both particle species at low energies with concave tails that extend up to the maximum momenta of the spectra, $\sim 10^3 m_p c$. Deviations between electron and proton spectra at lower momenta result from the different injection criteria for the particles. The total energy that went into electrons, $E_{\rm tot,e} \approx 6.8 \times 10^{47}$ erg, is marginal compared to that of protons, $E_{\rm tot,p} \approx 2.7 \times 10^{49}$ erg. Reasons for this are the small rest mass of electrons and different injection efficiencies $\eta_e = 9.4 \times 10^{-6}$ and $\eta_p = 2.4 \times 10^{-5}$, which are chosen to fit the entire SED. The electron injection efficiency simultaneously accounts for the maximum IC peak consistent with the γ-ray data and sufficient radio emission for $B_{\rm d} = 150\,\mu$G (amplification factor $\alpha \approx 9$), while injection of protons provides an adequate hadronic contribution in the GeV range. The injection efficiencies determine the electron-to-proton flux ratio, $K_{\rm e/p}$, in the range $(10 - 10^3) m_p\, c$.

The proton spectrum cuts off at the maximum momentum, $p_{\rm max} \approx 10^4 m_p\, c \simeq 10\,{\rm TeV/c}$, which is limited by the age of the remnant and particle diffusion in the upstream region. The latter process is determined by two factors: the magnetic precursor, which flat-

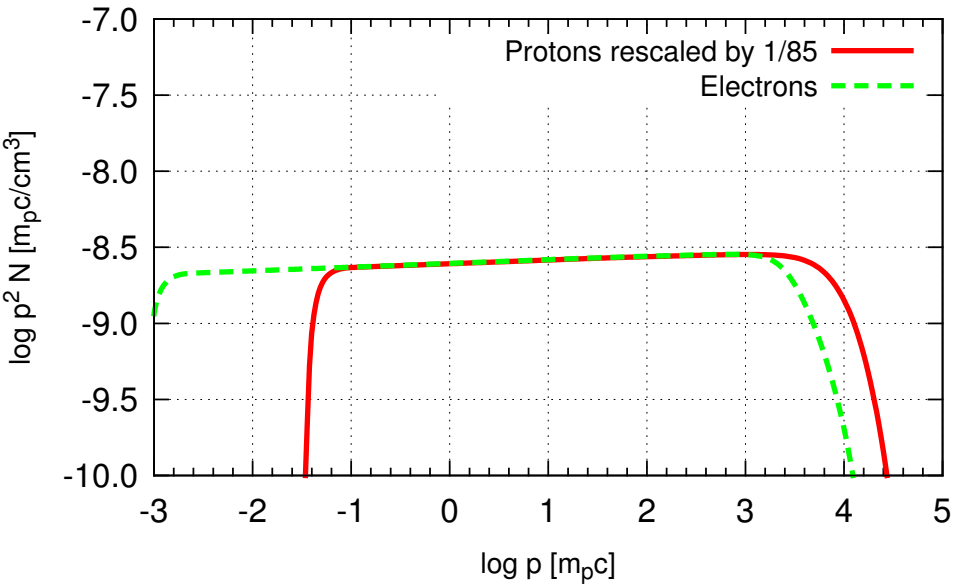

Figure 6.8: Number density of protons (red solid line) and electrons (green dashed line) for Model I with turned off stochastic re-acceleration. A comparison with Figure 6.7 illustrates the quantitative effect of the second-order acceleration in CR spectra.

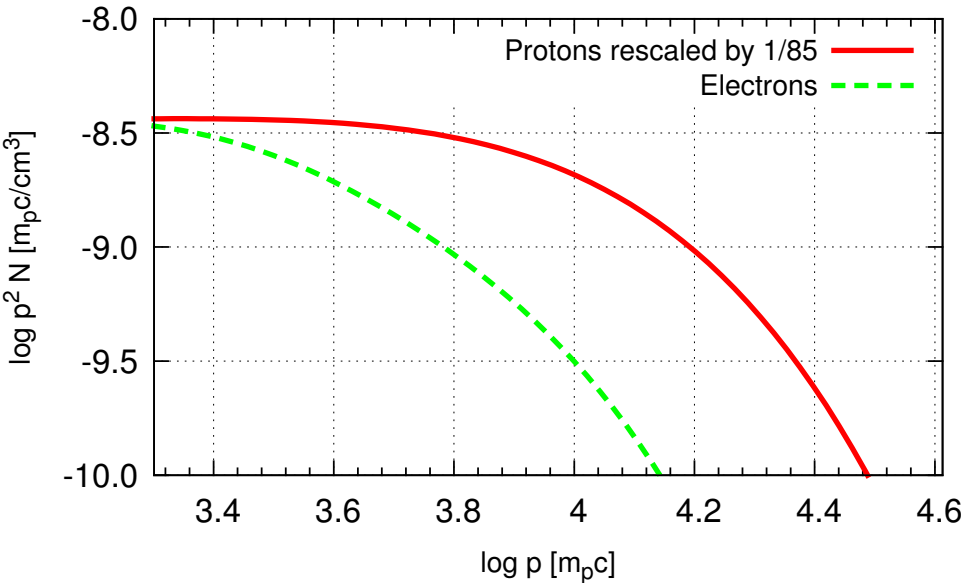

Figure 6.9: Number density of protons (red solid line) and electrons (green dashed line) for Model I as in Figure 6.7 zoomed to the cutoff region.

tens the CR precursor, discussed in Section 4.2, and the gyrofactor, ξ, which besides the magnetic-field strength co-determines the diffusive transport of particles. Since the electrons additionally experience effective synchrotron losses, their maximum momentum, $\sim 3\,\mathrm{TeV/c}$, is lower than the limit ($10\,\mathrm{TeV/c}$) imposed by the spatial diffusion and the age of the remnant. The exact shape of electron and proton cutoffs is shown in Figure 6.9, which allows a direct comparison of the cutoff forms. As one can see, the electron cutoff is steeper than that of protons due to effective synchrotron losses. We recall here that the spectral cutoff in our approach deviates from the simple exponential and super-exponential forms (e.g., Blasi (2010)) due to the full-time dependency of our method. In contrast to the previous works on Tycho, our approach includes the time-dependent transport equation and hydrodynamics. As mentioned in Chapter 4, the maximum CR energy in the age-limited case scales linearly with time and as the square of the shock velocity (e.g., Reynolds):

$$E_{\mathrm{max}} \propto V_{\mathrm{sh}}^2\, t\,. \tag{6.13}$$

Relation 6.13 indicates that in our approach the maximum energy of CR decreases with time. In fact, the shock of the remnant slows down in our simulations, as can be seen in Figure 6.1. The shock velocity drops faster than the linear time-growth, and thus the decrease of V_{sh}^2 in relation 6.13 cannot be compensated by the time t. As a result, the final particle spectrum in our work, which is qualitatively an average of instantaneous spectra, gives a sharper cutoff than predicted within approach with a constant shock velocity.

Instead of showing the entire SED at one single plot, we present figures for particular energy bands (radio, X-ray, and γ-ray) to provide a detailed comparison of data and models. The synchrotron emission from electrons in the radio and microwave bands for Model I is presented as a red solid line in Figure 6.10, where the data are taken from Reynolds and Ellison (1992) and Arnaud et al. (2016). The radio spectrum for Tycho is frequently considered to be distorted in response to shock modification by CR (Reynolds and Ellison, 1992; Völk et al., 2008). Figure 6.10 clearly demonstrates that this is not the only viable interpretation: stochastic re-acceleration in the downstream region of a test-particle shock can reproduce the observed radio spectrum without invoking nonlinear effects. It was noted earlier (Arnaud et al., 2016) that the radiation from Tycho in the microwave band consists of at least two components: synchrotron emission from the nonthermal electrons and thermal dust emission. The latter process is responsible for the sharp rise in flux above ∼30 GHz. We account for the thermal dust emission by calculating the gray-body radiation with a temperature of 25 K and a normalization chosen to fit the flux density measured with Herschel (Gomez et al., 2012). Thus, the red line in Figure 6.10 represents the sum of the synchrotron and thermal spectra. While the slightly concave part of the radio spectrum below ∼30 GHz is dominated by the synchrotron emission from electron population shaped by the stochastic re-acceleration, the steep flux increase above ∼30 GHz results from the thermal dust emission.

The X-ray emission is generated by electrons beyond the cutoff energy, $E_{\mathrm{max,e}} \approx 3$ TeV, via synchrotron radiation; it is presented for Model I as red solid line in Figure 6.11, where the *Suzaku* data at 90% confidence level are taken from Tamagawa et al. (2009). To achieve a good fit for the fixed magnetic field ($B_2 = 150\,\mu\mathrm{G}$) and electron injection

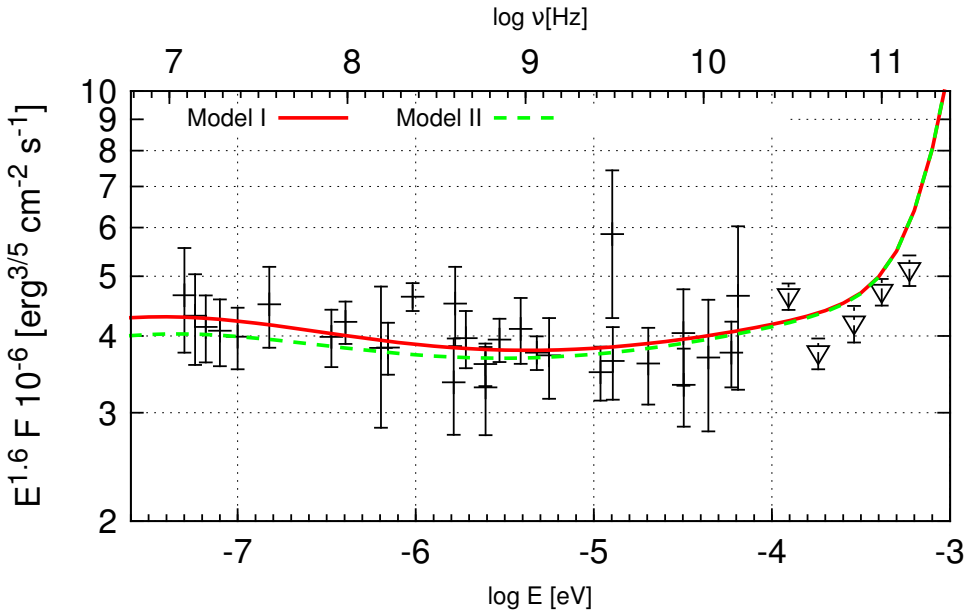

Figure 6.10: Synchrotron plus gray-body emission in the radio and microwave bands for Models I and II. The radio (black error bars) and microwave (black triangles) data are taken from Reynolds and Ellison (1992) and Arnaud et al. (2016).

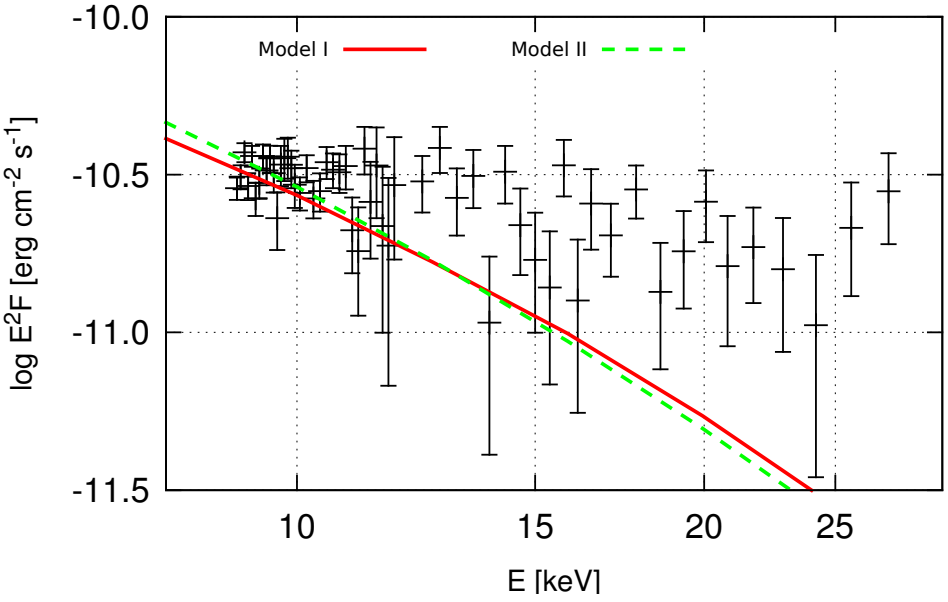

Figure 6.11: Synchrotron emission in the X-ray band for Models I and II with Gaussian distribution of magnetic-field amplitudes. Experimental data at 90% confidence level are taken from Tamagawa et al. (2009).

efficiency ($\eta_e = 9.4 \times 10^{-6}$), we adapt the spatial Bohm-diffusion coefficient parameter and set $\xi = 10$. As already mentioned in Section 4.6, for our calculation of the synchrotron emission we use a Gaussian distribution function for the amplitudes of the turbulent magnetic field. The differences to the standard formula are mostly seen at the cutoff of the synchrotron emission. First of all, since we use a Gaussian distribution function to calculate synchrotron emission, its cutoff deviates from the usually assumed exponential profile. The standard emissivity function produces the steepest slope in the spectral tail, while any extended distribution of the emissivity function smears the spectral cutoff and causes spectral hardening in the X-ray band. Nevertheless, the predicted X-ray spectrum above 10 keV, shown in Figure 6.11, is still softer than that observed. A possible explanation can be attributed to the spherical symmetry of our model geometry. Indeed, Lopez et al. (2015) analyzed 66 different regions across Tycho. Assuming an exponential cutoff in the synchrotron spectra, Lopez et al. (2015) find that the X-ray emission from individual regions of Tycho exhibits varying roll-off energy, which is defined as

$$E_{\rm rolloff} \simeq 7\,{\rm eV} \left(\frac{B_2}{100\,\mu{\rm G}}\right) \left(\frac{E_{\rm max,e}}{\rm TeV}\right)^2 . \tag{6.14}$$

As the magnetic field and the maximum energy of electrons may vary across Tycho's perimeter, so do the corresponding synchrotron spectra. Integration over the individual regions, as in Lopez et al. (2015), results in a total spectrum harder than for a synchrotron spectrum for an individual region because the variations in the roll-off energy invariably smear out the cutoff. This hardening cannot be accounted for in our model due to the 1D geometry, and hence our X-ray spectrum is softer than that observed by *Suzaku*.

The minimum downstream magnetic field that provides the maximum IC contribution compatible with the γ-ray data and sufficient flux contribution in the radio range on account of stochastic re-acceleration is $\sim 150\,\mu$G. A magnetic field any weaker than this would imply an overshooting of γ-ray emission at $\sim 100\,$GeV induced by the IC process. Nevertheless, it is not able to account for the GeV-scale emission, and hence the hadronic channel is required. The resulting γ-ray spectra of Tycho and the corresponding γ-ray data are given in the top panel of Figure 6.12. The pion bump is represented by the blue dotted, and the IC peak by the green dashed lines, respectively. The total γ-ray spectral distribution (red solid line) is rather flat with spectral index $\Gamma \approx 2$. The impact from the stochastic re-acceleration of protons is hardly visible in the pion bump. The reason is a relatively small energy fraction in the fast-mode waves. In our model for Tycho, parameters relevant for the stochastic re-acceleration are dictated by the radio data. For other SNRs, their value can differ, potentially resulting in more efficient re-acceleration of protons and consequentially a softer hadronic spectrum. Thus, stochastic acceleration of protons may provide an alternative explanation for the softening of hadronic emission, as opposed to high-density structures in the ambient medium (Berezhko et al., 2013; Morlino and Blasi, 2016), if enough energy is available for re-acceleration. Nevertheless, the impact of stochastic re-acceleration is more prominent for electron than proton spectra. The cutoff in the leptonic and hadronic γ-ray contributions is linked to that in the synchrotron spectrum via the gyrofactor, ξ, and hence constrained by X-ray data. Thus, in our approach, we do not specifically adjust the model parameters to fit the hadronic

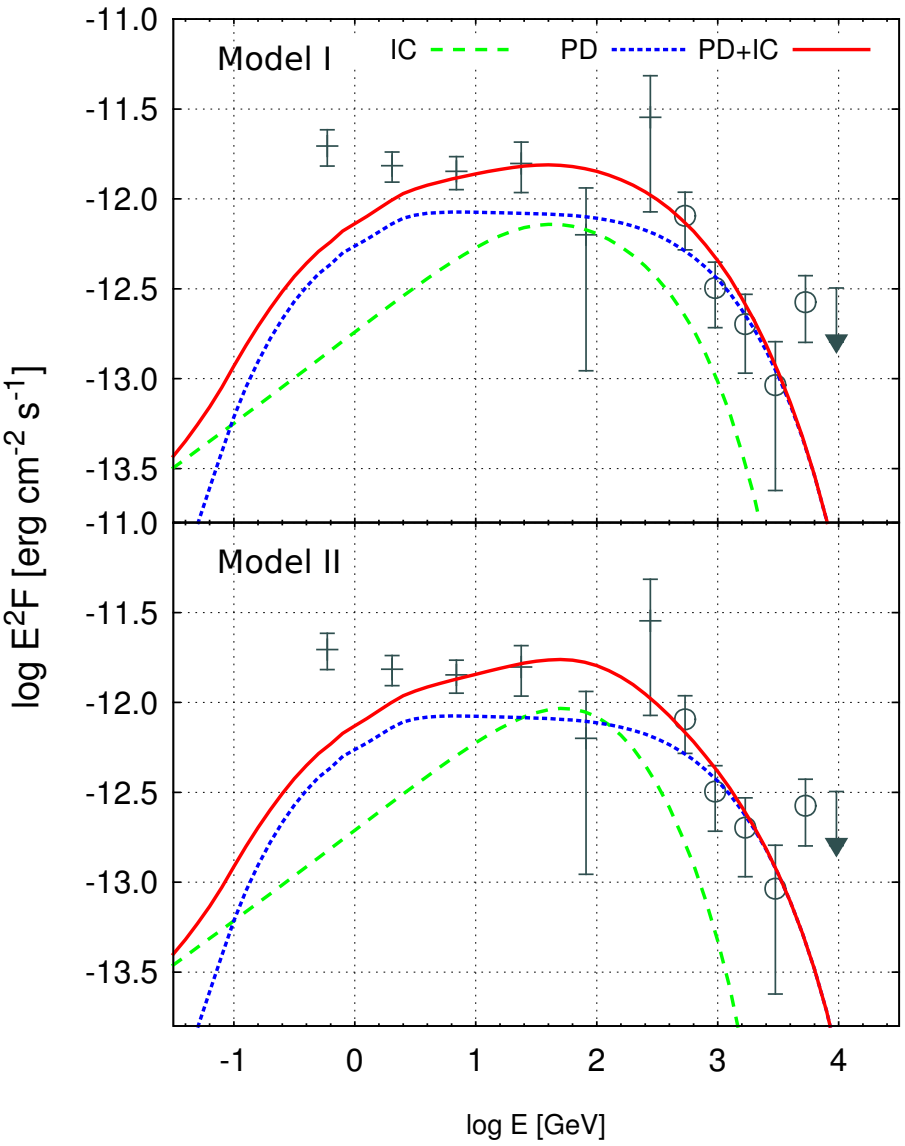

Figure 6.12: Calculated γ-ray emission from Tycho in comparison with measurements of *Fermi*-LAT (black solid) and VERITAS (black circles) from Archambault et al. (2017). The top panel is for Model I involving a moderate transported magnetic field, and the bottom panel presents results for Model II, which includes damping of magnetic field.

cutoff. Nevertheless, it shows a remarkable match with the observed VERITAS data. The corresponding parameters for Model I are summarized in the first row of Table 6.1. The amplification efficiency (i.e., the ratio between CR pressure and the amplified magnetic-field pressure in the immediate upstream region) is roughly ~ 74 for 440 years.

As already mentioned, the contribution from NTB is negligible for the density of gas at Tycho. Therefore, it is not shown in Figure 6.12 and we do not discuss it further.

To further test Model I, we consider the spatial profiles of radio and X-ray synchrotron radiation at 1.4 GHz and 1 keV, respectively. The results are depicted in the top panel of Figure 6.13. The radio (Slane et al., 2014) and X-ray (Cassam-Chenaï et al., 2007) brightness profiles are extracted from the western rim of the remnant and normalized to their peak values. The measured X-ray brightness is strongly peaked at the shock and rapidly decreases towards the CD. The radio profiles are slightly wider but still exhibit a narrow structure close to the shock. The enhancement of the emission towards the interior that is evident in the radio profiles might be attributed to the afore-mentioned Rayleigh-Taylor distortions operating in the vicinity of CD. As seen in the figure, the predictions of Model I involving the smallest possible advected magnetic field are in disagreement with the data. The model can explain neither the narrow X-ray rims nor the structure of the radio emission.

There are at least two potential solutions to this problem that we shall explore in the following section. Turbulent magnetic-field damping would affect the synchrotron emissivity and thus create narrow structures close to the shock. Alternatively, a very strong magnetic field at the shock would impose strong synchrotron losses and thus limit the width of the rims.

6.4.2 Model II: High damped magnetic field

As Model I involving a weak advected magnetic field fails to reproduce the observed intensity profiles of the synchrotron emission in both the radio and the X-ray bands, we now introduce damping of the turbulent magnetic field. Therefore we set the magnetic-field profile described by Equation 4.4. Obviously, in this scenario the magnetic field strength in the immediate downstream of the forward shock must be larger than for Model I because damping suppresses synchrotron emission from the far-downstream region. As IC radiation is produced wherever high-energy electrons reside, an overproduction of photons in the γ-ray band would arise unless the magnetic field is scaled up. Especially when combined with stochastic re-acceleration as an explanation for the radio data, the magnetic-field damping requires an extensive increase of the overall magnetic field. As

Table 6.1: Summary of the model parameters.

	Varying parameters					Fixed for both models				
Model	B_2 (μG)	B_0 (μG)	l_d (R_sh)	ξ	η_e	η_p	n_H (cm^{-3})	p_0 ($10^{-4} m_\mathrm{p} c$)	m	ϵ
I	150	-	-	10	9.4×10^{-6}	2.4×10^{-5}	0.6	9.3	0.25	0.027
II	330	70	0.01	16	10.2×10^{-6}	2.4×10^{-5}	0.6	9.3	0.25	0.027

B_2 magnetic field in the immediate post-shock region
B_0 residual level of the magnetic field
l_d damping scale of the downstream magnetic field
ξ spatial diffusion coefficient parameter (gyrofactor)
η_e injection efficiency of electrons
η_p injection efficiency of protons
n_H ambient hydrogen number density
p_0 critical momentum of the momentum-diffusion coefficient
m power-law index of the momentum-diffusion coefficient
ϵ energy-conversion factor for turbulence

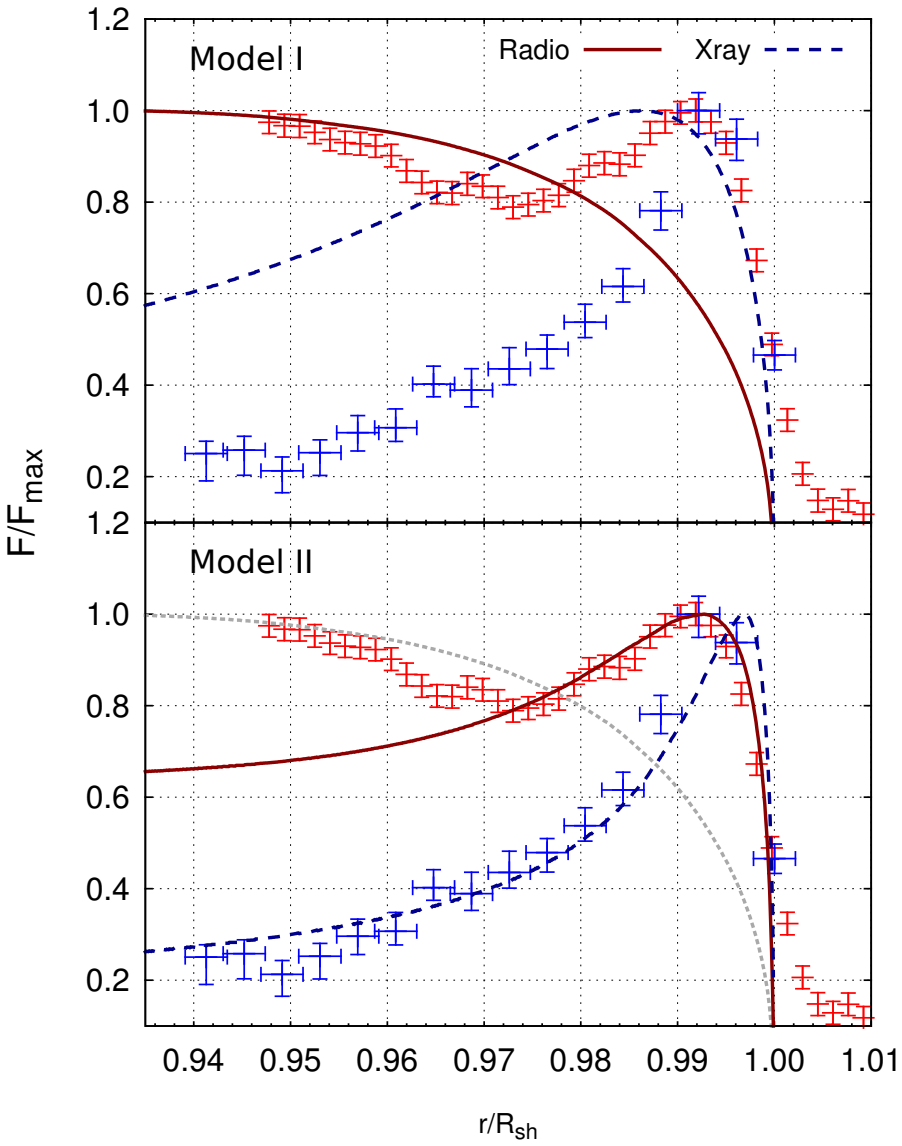

Figure 6.13: Radial intensity profiles for Model I (top panel) and Model II (bottom panel). X-ray emission at 1 keV (blue dashed line) was observed with *Chandra* (Cassam-Chenaï et al., 2007), and radio data at 1.4 GHz (red solid line) were taken from Slane et al. (2014). Following Slane et al. (2014), the radio data were slightly shifted to account for the expansion of the remnant. The gray dotted line in the bottom panel represents a radio profile produced without magnetic-field damping.

reflected by the decreasing width of the turbulent region, the stochastic re-acceleration of particles is more efficient at the early stages of SNR. As the re-accelerated electrons are advected away from the shock, they mostly experience the damped magnetic field. While the total synchrotron emission depends on the absolute values of the immediate post-shock field strength, B_2, and the residual level B_0, the shape of the radio filaments is determined (apart from the damping scale l_d) by the ratio of B_2 and B_0. We find that the immediate post-shock field strength and the residual level must be at least $B_2 = 330\,\mu$G (amplification factor $\alpha = 20$) and, $B_0 = 70\,\mu$G, respectively, in order to maximize the filling factor, and thus to produce sufficient overall synchrotron emission, and to fit the radio filaments simultaneously. Model II is based on these minimum values, and results are displayed as green dashed lines in Figures 6.10 and 6.11, as well as in the bottom panels of Figures 6.12 and 6.13.

Particle acceleration and propagation are modeled following the same procedure as in Model I, but some of the parameters are slightly adjusted. The second row of Table 6.1 lists the relevant model parameters, which now include the damping length, l_d, and the residual field level, B_0. Note that the damping length, l_d, provides spatial characteristics for the turbulence responsible for the magnetic-field amplification. Likewise, the width of the re-acceleration region, L_fm, represents the damping scale for the fast-mode waves. As both quantities are associated with different types of turbulence, they are independent of each other. At 440 years, the amplification efficiency for the second model is ~ 14.

Along the shock surface certain variations in the parameter values are to be expected, as not all filaments are the same (cf. Ressler et al., 2014). Also, Tycho is not a perfectly spherically symmetric SNR, and the projection effects may impose a bias. Therefore, our choice for the residual field level and the damping scale rather provide a reasonable order of their magnitudes as in this work we consider only one particular rim of Tycho. Fitting the *Suzaku* data with an enhanced post-shock magnetic-field $B_2 = 330\,\mu$G requires a moderate increase of the gyrofactor compared to Model I ($\xi = 16$).

Damping quenches the synchrotron emissivity in the deep downstream region. While the suppression is achromatic for power-law electron spectra, i.e., at frequencies below the cutoff in the synchrotron spectrum, it becomes progressively stronger beyond the roll-off energy. A competing process for quenching the emissivity at the roll-off frequency is energy losses preventing the propagation of electrons from the shock to the deep downstream region. The synchrotron loss time can be expressed in terms of the magnetic-field strength and the energy of photons, E_sy, that the electrons would typically emit

$$\tau_\mathrm{loss} \simeq 50\,\mathrm{yr} \left(\frac{B_2}{100\,\mu\mathrm{G}}\right)^{-3/2} \left(\frac{E_\mathrm{sy}}{\mathrm{keV}}\right)^{-1/2} . \tag{6.15}$$

The distance electrons travel during the loss time is roughly equal to the thickness of the filaments. Particle transport is governed by diffusion and advection. The latter process

dominates at lower energies, and its length scale is given by

$$l_{\rm adv} = u_2 \tau_{\rm loss} = \frac{V_{\rm sh}}{r_{\rm sh}} \tau_{\rm loss}$$
$$\simeq 2 \times 10^{17}\,{\rm cm} \left(\frac{V_{\rm sh}}{5000\,{\rm km/s}}\right) \left(\frac{B_2}{100\,\mu{\rm G}}\right)^{-3/2} \left(\frac{E_{\rm sy}}{\rm keV}\right)^{-1/2} . \quad (6.16)$$

At high energies, diffusion with Bohmian energy scaling becomes the dominant propagation process. The corresponding distance is energy-independent and is given by

$$l_{\rm diff} = \sqrt{D_s \tau_{\rm loss}} \simeq 10^{17}\,{\rm cm} \sqrt{\xi} \left(\frac{B_2}{100\,\mu{\rm G}}\right)^{-3/2} . \quad (6.17)$$

Equating relations 6.16 and 6.17, one can find the critical photon energy, where the transition from advection-dominated transport to diffusion-dominated transport occurs:

$$E_{\rm sy,c} \simeq \frac{4\,{\rm keV}}{\xi} \left(\frac{V_{\rm sh}}{5000\,{\rm km/s}}\right)^2 . \quad (6.18)$$

With $\xi = 16$ and $V_{\rm sh} = 4100\,{\rm km/s}$, we obtain $E_{\rm sy,c} \approx 0.2$ keV for Model II, implying that both advection and diffusion impact the distance covered by electrons that account for the 1 keV rims. Estimating the propagation length for the electrons that radiate 1 keV photons, we find $l_{\rm adv} \simeq 3 \times 10^{16}\,{\rm cm}$ and $l_{\rm diff} \simeq 7 \times 10^{16}\,{\rm cm}$, and therefore diffusive transport is more important, but advective transport is not negligible. Accounting for both advective and diffusive terms, the total transport length that the electrons travel before expending their energy is then given by (Parizot et al., 2006)

$$l_{\rm loss} = \left(\sqrt{\frac{u_2^2}{4D_r^2} + \frac{1}{D_r \tau_{\rm loss}}} - \frac{u_2}{2D_r}\right)^{-1} . \quad (6.19)$$

Applying expression 6.19 to electron emitting 1-keV photons in magnetic field of the strength $330\,\mu$G, one obtains $l_{\rm loss} \simeq 10^{17}\,{\rm cm}$. The underlying assumption of a constant magnetic-field strength used in Equation 6.19 is violated for Model II though, as the synchrotron energy losses decrease over a length scale of $l_{\rm d} = 0.01 R_{\rm sh} \simeq 5 \times 10^{16}\,{\rm cm}$ due to magnetic-field damping. Therefore, we conclude that the effective loss length of electrons is much larger than $10^{17}\,{\rm cm}$, and the synchrotron filaments are largely shaped by magnetic-field damping.

To account for the radio profiles, magnetic-field damping is clearly needed. Radio-emitting electrons have energy-loss times far in excess of the age of SNRs, and the radio rims cannot arise from synchrotron losses. The model with magnetic-field damping

(Model II) fits the spectral data reasonably well. To be noted from Figure 6.13 is that an effective damping length of $l_\mathrm{d} = 0.01 R_\mathrm{sh} \simeq 10^{17}$ cm can indeed reproduce the sharply peaked radio profiles in the shock vicinity, but somewhat underpredicts the radio intensity in the deep downstream region where Rayleigh-Taylors fingers from the CD may provide magnetic field amplification (Jun and Norman, 1995; Björnsson and Keshavarzi, 2017) that is not included in our model. In contrast, a radio emission profile calculated for non-damped magnetic field (gray dotted line in the bottom panel of Figure 6.13) obviously contradicts the observed data. As a relatively high magnetic-field value is required to maintain the total radio and γ-ray data, the width of the X-ray rims is inevitably affected by synchrotron losses. Still, magnetic-field damping is more important for the formation of the X-ray filaments since $l_\mathrm{loss} > l_\mathrm{d}$. Without magnetic-field damping, the synchrotron losses for the post-shock magnetic field $B_2 = 330\,\mu$G are able to produce the thin X-ray rims, but fail to form the radio profiles. When introduced as a natural explanation for the radio profiles, magnetic-field damping moreover becomes the dominant process for the production of the X-ray filaments.

We conclude that magnetic-field damping is essential for the radio filaments. Furthermore, for the minimum downstream magnetic field that can explain the complete observed data, $B_2 = 330\,\mu$G, magnetic-field damping is more important for the X-ray profiles than radiative losses. Nevertheless, for 1-keV emission synchrotron losses provide a subordinate additional process for X-ray filaments formation. Simultaneously the width of the radio rim is solely determined by the magnetic-field damping. In agreement with our results, the joint X-ray and radio analysis of Tran et al. (2015) reveals magnetic-field damping to be the preferable scenario. Both studies find similar damping lengths: 1-2% of the SNR radius.

6.4.3 Cosmic-ray pressure

Next, we verify that the test-particle approximation is valid for Model II. To this aim, we calculate the CR pressure, given by

$$P_\mathrm{cr}(r,t) = \frac{c}{3} \int N(r,p,t) \frac{p^2 dp}{\sqrt{p^2 + (m_p c)^2}}\,, \tag{6.20}$$

where m_p is the rest mass of proton and $N(r,p,t)$ the differential proton number density. As mentioned before, the pressure exerted by the nonthermal electrons is negligible in our model. The relative-velocity change of the plasma in the shock rest-frame in a particular region between r_1 and r_2 caused by the particle pressure is (cf. Section 2.5.2)

$$\frac{\delta u}{u} = -\frac{1}{u^2 \rho} \int_{r_1}^{r_2} dx \frac{\partial P_\mathrm{cr}(x)}{\partial x} = \frac{P_\mathrm{cr}(r_2) - P_\mathrm{cr}(r_1)}{P_\mathrm{flow}} \equiv \frac{\delta P_\mathrm{cr}}{P_\mathrm{flow}}\,. \tag{6.21}$$

Here ρ denotes the density, u the velocity, and $P_\mathrm{flow} = \rho u^2$ the dynamical pressure of the plasma. Equation 6.21 is universally valid and holds in any region of the plasma flow.

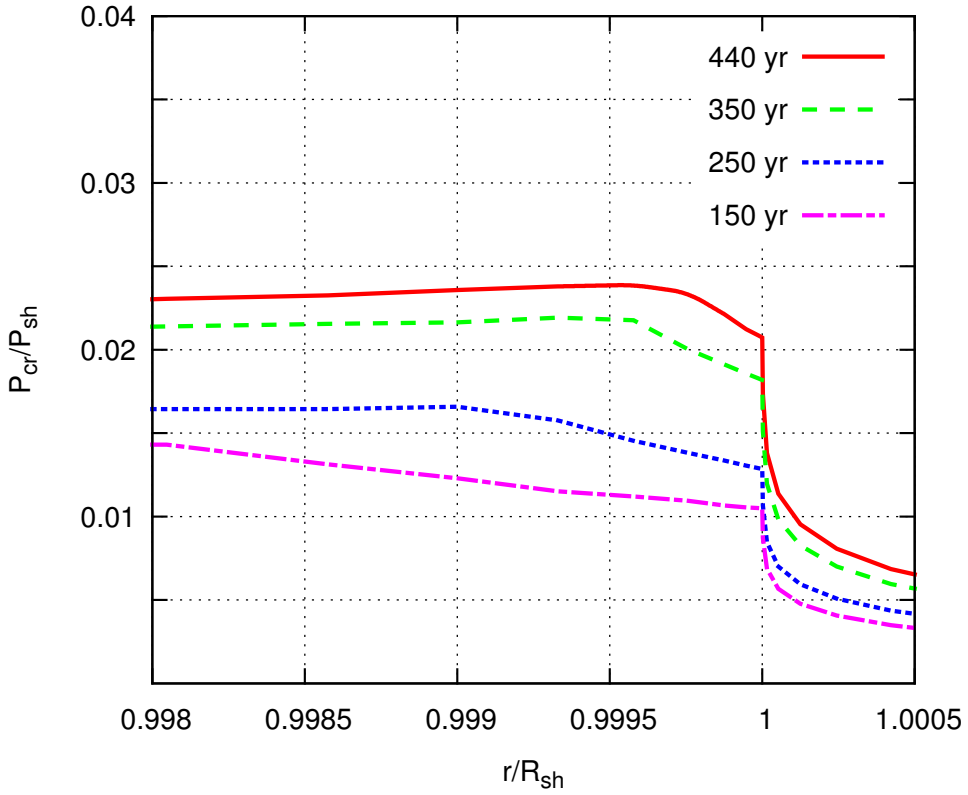

Figure 6.14: CR pressure, $P_{\rm cr}$, normalized by the shock ram pressure, $P_{\rm sh}$, for Model II (damped magnetic field with $B_2 = 330\,\mu$G) for different times.

According to Kang and Ryu (2010), the test-particle approximation is justified as long as the CR pressure in the precursor does not exceed 10% of the shock ram pressure. Consequently, according to Equation 6.21 the test-particle regime requires $\delta u/u = \delta P_{\rm cr}/P_{\rm flow} \leq 0.1$ in the upstream region. Figure 6.14 shows the CR pressure normalized by the shock ram pressure, $P_{\rm sh} = \rho_1 u_1^2$, as a function of the position, $r/R_{\rm sh}$, for different times. To be noted from the figure is that the relative velocity change in the upstream region at 440 years is $\delta u/u = \delta P_{\rm cr}/P_{\rm sh} \approx 0.021$, and hence clearly below the test-particle threshold. Similarly, at the earlier stages, the CR pressure at the shock does not exceed $\delta u/u < 0.1$, verifying that the dynamic CR feedback is indeed negligible in our approach.

Behind the shock wave, the pressure of particles is significantly enhanced due to stochastic re-acceleration. In contrast to standard DSA, where the maximal CR pressure occurs at the shock, in our model it reaches its maximum in the immediate downstream region. The corresponding position is determined by the current width of the turbulent zone where the fast-mode waves operate. Taking into account that the dynamic pressure in the post-shock region is a factor 4 lower than the shock ram pressure in the shock rest-frame, we estimate for the total velocity change at 440 years: $\delta u/u \approx 0.01$. It is worth

recalling here that the test-particle threshold determined by Kang and Ryu (2010) concerns the upstream region of SNRs and is in general not applicable in the post-shock area. In this work, we neglect the dynamical feedback from the re-accelerated particles in the downstream region. Nevertheless, this effect may be of interest for future investigations. Indeed, when strong enough, the stochastic acceleration can have a significant effect on the post-shock structure. The CR pressure in the immediate downstream region enhanced by the stochastic acceleration has to press the plasma away from the re-acceleration region and force it to accumulate directly behind the shock. This process increases the plasma density and the associated magnetic-field strength at the shock of the SNR. It is clear that this phenomenon fundamentally differs from the standard dynamical reaction of particles described in the NLDSA theory.

Summarizing, we conclude that we find a viable self-consistent scenario for Tycho, represented by Model II.

6.4.4 Hadronic model

In the previous section, we present a lepto-hadronic scenario that requires the lowest possible magnetic field in the remnant compatible with radio filaments and the SED. More efficient magnetic-field amplification suppresses the IC component until the γ-ray spectrum becomes purely hadronic. In our approach, where we use magnetic-field damping to fit the radio filaments, we find the magnetic-field values have to be at least $B_0 \approx 120\,\mu$G and $B_2 \approx 600\,\mu$G for a purely hadronic model. The total magnetic energy in the remnant in that case is still moderate, $\sim 1.1 \times 10^{49}$ erg, on account of the magnetic-field damping.

As discussed in Section 6.3, the separate treatment of magnetic field and hydrodynamics for the ambient density of $n_{\rm H} = 0.6\,{\rm cm}^{-3}$ is justified for post-shock magnetic field below 400 μG. Thus, for the hadron-dominated case, the dynamical feedback from the magnetic field becomes significant. The corresponding pressure, with the Alfvénic Mach number $M_{\rm A,1} \approx 9.6$, would lower the shock compression ratio to $r_{\rm sh} \approx 3.87$, as one can see from Figure 6.4. Thus the particle and radio spectra indices are softened to $s \approx 2.05$ and $\alpha \approx -0.52$, respectively. As the electron spectrum becomes slightly softer on account of the impact of the magnetic field, the contribution from the stochastic re-acceleration becomes less necessary. Hence, in general, as competing explanation for the softening of the spectra, very high magnetic field inevitably decreases the energy fraction converted to turbulence, ϵ.

Due to the very high magnetic field, X-ray filaments at 1 keV would be primarily governed by the radiative losses, with a corresponding propagation scale $l_{\rm loss} \simeq 4 \times 10^{16}$ cm. Thus, the brightness profile would lack the X-ray flux due to extreme synchrotron losses. Nevertheless, as pointed out above, the radio as well as the X-ray rims can strongly vary with position along the perimeter due to the natural asymmetry of the remnant. As the electrons emitting the synchrotron radiation in the radio range do not experience significant losses, the radio profiles do require magnetic-field damping.

In summary, we conclude that a purely hadronic model is possible for Tycho, but requires an elaborate and cautious treatment, which among other effects, includes the dynamical feedback from magnetic-field pressure. Nevertheless, the lepto-hadronic sce-

nario, referred to as Model II, is able to explain the broadband observations of Tycho in a satisfactory manner.

6.5 Summary for modeling of Tycho

In this chapter, we conducted extensive multiwavelength modeling of Tycho. For the very first time we accounted for stochastic re-acceleration in the downstream region of the forward shock, which provides a consistent explanation for the soft particle spectra without resorting to Alfvénic drift (Völk et al., 2008; Morlino and Caprioli, 2012; Slane et al., 2014) and its inherent problems, or deducing the particle spectral index from the radio observations (Atoyan and Dermer, 2012; Zhang et al., 2013; Caragiulo and Di Venere, 2014). As discussed in the introduction, although it has been widely used in the global models for various SNRs, we find the concept of Alfvénic drift contradictory. We presented instead a new approach that adds diffusion in momentum space to the standard DSA approach. Furthermore, in our method both hydrodynamics and particle acceleration are fully time dependent.

The stochastic acceleration of particles in the immediate downstream region is assumed to arise from the fast-mode turbulence, which is supplied by the energy of the background plasma. We found that 2.7% of the thermal energy density of the downstream background plasma is sufficient to explain Tycho's soft radio spectra. Simultaneously, the magnetic field is assumed to be amplified by streaming instabilities (Bell, 2004; Bell and Lucek, 2001) or turbulent dynamos (Giacalone and Jokipii, 2007). Based on this, we have presented a self-consistent global model (Model II) that is able to accurately reproduce the observed radio, X-ray, and γ-ray emission, and simultaneously account for the nonthermal filaments in the radio and X-ray ranges. The radio filaments are generated due to magnetic-field damping, which is widely considered to allow a relatively low magnetic-field value inside a remnant. Combining this scenario with stochastic re-acceleration, we found that the minimum magnetic-field required to explain the entire observed data set of Tycho is $B_2 \approx 330\,\mu$G. This value is similar to the results of Morlino and Caprioli (2012), Völk et al. (2008), and Zhang et al. (2013), although the underlying physical assumptions are quite different. We find that for this minimum magnetic-field strength of $B_2 \approx 330\,\mu$G, the X-ray filaments at 1 keV are primarily produced by magnetic-field damping, while the synchrotron losses play a secondary role. This finding is inconsistent with the work of Morlino and Caprioli (2012), who concluded that X-ray filaments shaped by magnetic-field damping are not possible for Tycho. An important criterion here is that the propagation length and hence synchrotron loss scale for electrons radiating at 1 keV, is dominated by diffusion. For this reason, the diffusive transport of particles, which has been previously neglected in all global models of Tycho, must be taken into account to adequately model the X-ray filaments. We stress that an accurate modeling of the filaments is seamlessly tied to the determination of the post-shock magnetic field. Magnetic-field damping is additionally needed for its unique capability to explain the radio rims. In our model for Tycho, the magnetic-decay length is of the order of $l_\mathrm{d} \sim 0.01 R_\mathrm{sh}$, which is consistent with the estimate of Tran et al. (2015). The total magnetic energy in the remnant for Model II is 3.4×10^{48} erg. This value is moderate on account of magnetic-field damping, in spite

of the efficient magnetic-field amplification at the shock.

In the framework of our model, we predict relatively inefficient Bohm diffusion, reflected in the value of the gyrofactor $\xi \approx 16$. This value is required to consistently fit the synchrotron cutoff observed in the X-ray range. In line with most previous works on Tycho, we also conclude that the acceleration of protons is required to explain the γ-ray flux observed by VERITAS and *Fermi*-LAT. Our research cannot account for a purely leptonic origin for the γ-ray emission, as in Atoyan and Dermer (2012). We instead favor a mixed model with a composite flat spectrum ($\Gamma \approx 2$). The electron-to-proton ratio for Model II is $K_{\mathrm{e/p}} \approx 1/80$, and the maximum energy for protons is $E_{\mathrm{max,p}} \approx 10\,\mathrm{TeV}$ since it is linked to the roll-off energy of the synchrotron emission via gyrofactor, ξ. This result falls below the previously presented ∼500 TeV (Morlino and Caprioli, 2012) and ∼50 TeV (Slane et al., 2014). The maximum energy of electrons is ∼3 TeV, which is similar to the value 5 - 6 TeV suggested by Zhang et al. (2013) and Caragiulo and Di Venere (2014). The total energy in protons in our model is $E_{\mathrm{tot,p}} \approx 2.7 \times 10^{49}\,\mathrm{erg}$, implying that a few percent of the explosion energy went into CR. This value is significantly below the 16% claimed by Slane et al. (2014). We can use the test-particle approximation, as a relatively marginal energy fraction is transferred to particles and the CR pressure at the shock does not exceed 2.1% of the shock ram pressure during the entire evolution of the remnant.

Furthermore, we explicitly show that NLDSA effects are not required, either to explain the hydrodynamic structure of Tycho or to produce its slightly concave radio spectrum. First, the hydrodynamic simulations with an ambient gas density of $n_{\mathrm{H}} = 0.6\,\mathrm{cm}^{-3}$ and canonical explosion energy of 10^{51} erg provide a decent fit to the observed radii and a reasonable remnant distance of $\sim$ 2.9 kpc. Second, the radio spectrum is produced by synchrotron emission generated by electrons that are re-accelerated in the immediate downstream region. In general, the imprint left by stochastic re-acceleration is more prominent in electrons than in protons. Thus, future γ-ray observations that can successfully discriminate between leptonic and hadronic models for various SNRs may also be able to distinguish between NLDSA and stochastic re-acceleration scenarios.

We find that a purely hadronic model may also be possible for Tycho for the immediate post-shock magnetic-field $B_2 \approx 600\,\mu\mathrm{G}$ and far-downstream field $B_0 \approx 120\,\mu\mathrm{G}$. However, we do not explicitly model the hadronic scenario in this work because the dynamical reaction of the magnetic field has to be taken into account, an effect that is not yet included in our method. Nevertheless, we favor a lepto-hadronic scenario (Model II) as it might better produce the X-ray filaments. Additionally, extremely efficient magnetic-field amplification is not required, as in the case of a purely hadronic model.

In our model for Tycho, the contribution of the stochastic re-acceleration in the proton spectrum is marginal due to the small energy fraction converted into downstream turbulence. For a larger amount of energy in fast-mode waves, the corresponding γ-ray spectrum has to be naturally softer than predicted by the standard DSA, which could provide a viable explanation for the observed soft γ-ray spectra of some SNRs. This subject is beyond the scope of this work but could be of interest for future investigations.

Finally, we emphasize that the dynamical feedback on the background plasma from the CR re-accelerated in the immediate downstream region of the SNR is of great interest

for future studies, because it clearly differs from the classical nonlinear effects discussed in the literature.

In summary, we find that stochastic re-acceleration is indeed a promising and natural alternative to explain the soft spectra of Tycho and potentially other SNRs.

Chapter 7

Summary and conclusions

SNRs are widely accepted as the most promising CR accelerators, mainly due to the success of the DSA theory and its nonlinear modifications. At the first glance, DSA in its linear and nonlinear versions seem to suffice as the only mechanism that explains the observed spectra of SNRs. Nevertheless, as often the case, the devil is in the detail. A closer look reveals that the standard theory fits the observed emission spectra only in a very rough agreement. Especially the detailed global modeling of particular SNRs demonstrates inconsistencies in spectral slopes, as repeatedly discussed throughout this work.

This thesis addresses the question, why the observed radio spectra of many SNRs are often not in accord with the conventional theory. The main focus of this work lies solely on the softening of the particle and photon spectra. In the majority of the global SNRs models, it is popular to ascribe the soft radio spectra to the Alfvénic drift with a large Alfvén velocity of a few 100 km/s. However, according to the work of Vainio and Schlickeiser (1999), where a self-consistent Alfvén waves transmission through the shock was considered, the presence of Alfvén waves causes exactly the opposite effect, namely the hardening of particle spectra. Therefore, we consider the scenario described in Vainio and Schlickeiser (1999) as a possible explanation for the observed hard spectra. For the opposite case of soft radio spectra, we investigate a viable explanation, which involves a stochastic re-acceleration of electrons inside SNRs.

To this end, we present in Chapter 3 a generic model, where electrons are stochastically re-accelerated by fast-mode waves after escaping from the shock into the downstream region. It was found that stochastic re-acceleration can indeed produce softer electron spectra, with corresponding radio spectral index α between -0.6 and -0.7. Therefore we conclude that re-acceleration of electrons in the post-shock area can explain the observed radio flux from many SNRs.

Next, the concept of stochastic re-acceleration is included in the program RATPaC, originally developed by Telezhinsky et al. (2012a). Chapter 4 reviews the comprehensive code and presents the details of the stochastic re-acceleration in RATPaC. Here, the stochastic re-acceleration works as a secondary process simultaneously with the standard DSA. While Bohm diffusion coefficient and spatial convection terms account for the first-order Fermi acceleration, fast-mode waves provide diffusion in momentum space. In

contrast to the previous approach, the width of the turbulent region is self-consistently calculated from the thermal energy of an SNR.

In the following chapters, RATPaC is applied to two young SNRs, which are both promising objects to study CR acceleration: Cas A and Tycho. In Chapter 5, as a test for RATPaC, a time-independent one-zone model for the young SNR Cas A is presented. Nevertheless, even from a relatively simple approach important conclusions for the processes in Cas A SNR were made. The lower magnetic-field limit inside Cas A is found to be $\sim 150\,\mu$G.

Further, in Chapter 6, RATPaC is applied to model the young Type Ia remnant Tycho, where a detailed, fully time-dependent test-particle approach coupled to hydrodynamical simulations is used. A number of studies (Völk et al., 2008; Morlino and Caprioli, 2012; Slane et al., 2014) suggest that shock acceleration with particle feedback and very efficient magnetic-field amplification combined with Alfvénic drift are needed to explain Tycho's soft radio spectrum and the narrow rims observed in X-rays. In contrast to the previous works, this thesis demonstrates that the broadband spectrum of Tycho can be alternatively well explained if stochastic re-acceleration of particles in the immediate post-shock region is taken into account. Although not as efficient as DSA, stochastic acceleration leaves its imprint on the particle spectra, which is especially notable in the emission at the radio wavelengths. Thus, Alfvénic drift and efficient particle feedback are not required in our scenario. Besides the second-order Fermi process, magnetic field in Tycho comes under scrutiny. It is common to posit magnetic-field strength of a few hundred microGauss when modeling the broadband emission of SNRs. One of the reasons is the afore-mentioned Alfvénic drift, which requires for Tycho magnetic field of the order $\sim 300\,\mu$G to adequately fit the observations. Furthermore, strongly amplified magnetic fields are deduced from the thin X-ray rims observed from SNRs. These are usually interpreted as typical paths of electrons that they travel before exhausting their energy via synchrotron emission (Parizot et al., 2006). Nevertheless, caution should be exercised when estimating magnetic fields from the nonthermal filaments. In addition to the common scenario, where the X-ray emission decreases toward the SNRs center due to effective synchrotron losses, an alternative explanation involves magnetic-field damping. In this case, the observed nonthermal filaments reflect the distribution of the amplified magnetic field, which decays in the interior of an SNR. We studied the nonthermal rims of Tycho and investigated whether synchrotron losses or magnetic-field damping play a more profound role in the formation of the nonthermal filaments. Our results demonstrate that magnetic-field damping is necessary due to its unique capability to explain Tycho's filaments in the radio range. In general, magnetic-field damping allows for a moderately amplified magnetic field inside SNRs compared to the case with loss-limited X-ray filaments. However, we find a lower limit for the post-shock magnetic field in Tycho to be $\sim 330\,\mu$G, implying efficient amplification even for the magnetic-field damping scenario. The reason is a simultaneous fit of the magnetic-field limited radio rims and the entire SED, which requires sufficient radio flux from the re-accelerated electrons as well as relatively low IC peak. For magnetic field this strong the X-ray filaments of Tycho are shaped by both the synchrotron losses and magnetic-field damping.

Despite the slightly different model approaches, the analysis presented in this thesis

demonstrates certain similarities for Type Ia Tycho and core-collapse SNR Cas A. According to our analysis, both Tycho and Cas A accelerate protons, while a purely leptonic model is found to be highly unlikely for both SNRs. In line with previous studies, both remnants are not PeVatrons, and the maximum CR energy is around a few TeV instead. According to our modeling, the corresponding acceleration efficiency in Tycho and Cas A is roughly about a few percent. Both remnants indicate electron spectra softer as predicted by the standard DSA, with $s_e = 2.5$ for Cas A and $s_e = 2.3$ for Tycho, respectively. Furthermore, for Cas A the canonical DSA solution for the hadronic spectra was excluded by more than 3σ, with corresponding best-fit value $s_p = 2.17$. Similarities between the two SNRs can be attributed to their alike young age.

In summary, this work shows the importance of putting the small details of a grand theory under the microscope. After all, more sophisticated models coupled to advanced observations may bring together the fine pieces of the cosmic puzzle.

Appendix A

General MHD equations

The general MHD equations, where any external force, viscosity, heat conduction, and radiative effects are omitted, read as (e.g., Kirk et al. (1994), Ryden (2011))

$$\frac{D\rho}{Dt} = -\rho \boldsymbol{\nabla} \cdot \boldsymbol{u} \qquad \text{(Conservation of mass)} \tag{A.1}$$

$$\rho \frac{D\boldsymbol{u}}{Dt} = -\boldsymbol{\nabla} P + \frac{1}{4\pi}(\boldsymbol{\nabla} \times \boldsymbol{B}) \times \boldsymbol{B} \qquad \text{(Conservation of momentum)} \tag{A.2}$$

$$\rho \frac{D\epsilon_p}{Dt} = -P \boldsymbol{\nabla} \cdot \boldsymbol{u} + \frac{\eta_D}{4\pi} |\boldsymbol{\nabla} \times \boldsymbol{B}|^2 \qquad \text{(Conservation of energy)} \tag{A.3}$$

$$\frac{\partial \boldsymbol{B}}{\partial t} + \boldsymbol{\nabla} \times (\boldsymbol{B} \times \boldsymbol{u}) = -\boldsymbol{\nabla} \times (\eta_D \boldsymbol{\nabla} \times \boldsymbol{B}) \qquad \text{(Induction equation)} \tag{A.4}$$

$$\boldsymbol{\nabla} \cdot \boldsymbol{B} = 0 \qquad \text{(Gauss's law for magnetism)} \tag{A.5}$$

$$\epsilon_p = \frac{1}{\gamma_a - 1} \frac{P}{\rho} \tag{A.6}$$

Here $\boldsymbol{u}$ is the velocity, and $\boldsymbol{B}$ the magnetic field of the plasma, which are primary variables in the MHD[1]. The plasma density is denoted by ρ and the thermal pressure by P. The internal energy per unit mass, ϵ_p, is given by the standard Equation A.6 for an ideal gas where γ_a is the adiabatic index.

The *magnetic diffusivity* is defined as $\eta_D = c^2/(4\pi\sigma_e)$ where σ_e denotes the electric conductivity. This quantity represents the diffusion of the magnetic field and approaches zero in the limit of infinite conductivity. In that case, one speaks of so-called *magnetic flux freezing* because the magnetic flux is tied to the plasma. The approach is also referred to as the *ideal MHD* and is justified for the large variety of astrophysical plasmas. Therefore,

[1] In contrast to electromagnetism where the basic quantities are the electric fields and currents.

in this thesis it is in general set $\eta_D = 0$. The operator

$$\frac{D}{Dt} = \frac{\partial}{\partial t} + \boldsymbol{u} \cdot \boldsymbol{\nabla}$$

is the *material* derivative, which represents changes in the point that convects with the plasma flow. In contrast, the partial time-derivative, $\partial/\partial t$, describes the changes in a fixed point of space.

Bibliography

A. A. Abdo et al. Fermi-Lat discovery of GeV gamma-ray emission from the young supernova remnant Cassiopeia A. *Astrophysical Journal, Letters*, 710(1):L92–L97, 2010.

A. U. Abeysekara et al. Evidence for Proton Acceleration up to TeV Energies Based on VERITAS and Fermi-LAT Observations of the Cas A SNR. *Astrophysical Journal*, 894 (1):51, 2020.

V. A. Acciari et al. Observations of the shell-type supernova remnant Cassiopeia A at TeV Energies with VERITAS. *Astrophysical Journal*, 714:163–169, 2010.

V. A. Acciari et al. Discovery of TeV gamma-ray emission from Tycho's supernova remnant. *Astrophysical Journal, Letters*, 730:L20, 2011.

M. Ackermann et al. Detection of the characteristic pion-decay signature in supernova remnants. *Science*, 339:807–811, 2013.

F. Aharonian et al. Evidence for TeV gamma-ray emission from Cassiopeia A. *Astronomy and Astrophysics*, 370:112–120, 2001.

F. Aharonian et al. A detailed spectral and morphological study of the gamma-ray supernova remnant RX J1713.7-3946 with HESS. *Astronomy and Astrophysics*, 449(1): 223–242, 2006.

F. A. Aharonian et al. High-energy particle acceleration in the shell of a supernova remnant. *Nature*, 432(7013):75–77, 2004.

M. L. Ahnen et al. A cut-off in the TeV gamma-ray spectrum of the SNR Cassiopeia A. *Monthly Notices of the RAS*, 472:2956–2962, 2017.

J. Albert et al. Observation of VHE γ-rays from Cassiopeia A with the MAGIC telescope. *Astronomy and Astrophysics*, 474(3):937–940, 2007.

G. E. Allen, M. D. Stage, and J. C. Houck. Nonthermal bremsstrahlung vs. synchrotron radiation: Cas A. *International Cosmic Ray Conference*, 2:839–842, 2008.

R. J. Allen and A. H. Barrett. Absolute measurements of the radio flux from Cassiopeia A and Taurus A at 3.64 and 1.94 CM. *Astrophysical Journal*, 149:1, 1967.

M. Anderson, L. Rudnick, P. Leppik, R. Perley, and R. Braun. Relativistic electron populations in Cassiopeia A. *Astrophysical Journal*, 373:146, 1991.

M. Araya and W. Cui. Evidence for cosmic-ray acceleration in Cassiopeia A. *Astrophysical Journal*, 720:20–25, 2010.

S. Archambault et al. Gamma-ray observations of Tycho's supernova remnant with VERITAS and Fermi. *Astrophysical Journal*, 836(1):23, 2017.

M. Arias et al. Low-frequency radio absorption in Cassiopeia A. *Astronomy and Astrophysics*, 612:A110, 2018.

M. Arnaud et al. Planck intermediate results. XXXI. Microwave survey of Galactic supernova remnants. *Astronomy and Astrophysics*, 586:A134, 2016.

A. Atoyan and C. D. Dermer. Gamma rays from the Tycho supernova remnant: multizone versus single-zone modeling. *Astrophysical Journal, Letters*, 749:L26, 2012.

A. M. Atoyan, F. A. Aharonian, R. J. Tuffs, and H. J. Völk. On the gamma-ray fluxes expected from Cassiopeia A. *Astronomy and Astrophysics*, 355:211–220, 2000.

W. I. Axford, E. Leer, and G. Skadron. The acceleration of cosmic rays by shock waves. *International Cosmic Ray Conference*, 11:132–137, 1977.

W. Baade and F. Zwicky. Cosmic rays from Supernovae. *Proceedings of the National Academy of Science*, 20:259–263, 1934.

J. W. M. Baars, R. Genzel, I. I. K. Pauliny-Toth, and A. Witzel. The absolute spectrum of Cas A - an accurate flux density scale and a set of secondary calibrators. *Astronomy and Astrophysics*, 61:99–106, 1977.

C. Badenes, K. J. Borkowski, J. P. Hughes, U. Hwang, and E. Bravo. Constraints on the physics of Type Ia Supernovae from the X-ray spectrum of the Tycho supernova remnant. *Astrophysical Journal*, 645:1373–1391, 2006.

A. Bamba, R. Yamazaki, M. Ueno, and K. Koyama. Small-scale structure of the SN1006 shock with Chandra observations. *Astrophysical Journal*, 589(2):827–837, 2003.

A. Bamba, R. Yamazaki, T. Yoshida, T. Terasawa, and K. Koyama. A Spatial and Spectral Study of Nonthermal Filaments in Historical Supernova Remnants: Observational Results with Chandra. *Astrophysical Journal*, 2005.

P. A. Becker, T. Le, and C. D. Dermer. Time-dependent stochastic particle acceleration in astrophysical plasmas: exact solutions including momentum-dependent escape. *Astrophysical Journal*, 647(1):539–551, 2006.

A. R. Bell. The acceleration of cosmic rays in shock fronts. I. *Monthly Notices of the RAS*, 182:147–156, 1978a.

A. R. Bell. The acceleration of cosmic rays in shock fronts. II. *Monthly Notices of the RAS*, 182:443–455, 1978b.

A. R. Bell. Turbulent amplification of magnetic field and diffusive shock acceleration of cosmic rays. *Monthly Notices of the RAS*, 353:550–558, 2004.

A. R. Bell and S. G. Lucek. Cosmic ray acceleration to very high energy through the non-linear amplification by cosmic rays of the seed magnetic field. *Monthly Notices of the RAS*, 321:433–438, 2001.

A. R. Bell, S. F. Gull, and S. Kenderdine. New radio map of Cassiopeia A at 5 GHz. *Nature*, 257:463–465, 1975.

A. R. Bell, K. M. Schure, and B. Reville. Cosmic ray acceleration at oblique shocks. *Monthly Notices of the RAS*, 418:1208–1216, 2011.

E. G. Berezhko and Donald C. Ellison. A simple model of nonlinear diffusive shock acceleration. *Astrophysical Journal*, 526(1):385–399, 1999.

E. G. Berezhko, G. Pühlhofer, and H. J. Völk. Gamma-ray emission from Cassiopeia A produced by accelerated cosmic rays. *Astronomy and Astrophysics*, 400:971–980, 2003.

E. G. Berezhko, L. T. Ksenofontov, and H. J. Völk. The nature of gamma-ray emission of Tycho's supernova remnant. *Astrophysical Journal*, 763:14, 2013.

V. S. Berezinskii, S. V. Bulanov, V. A. Dogiel, and V. S. Ptuskin. *Astrophysics of cosmic rays*. Elsevier Science Ltd, 1990.

M. Bhatt, I. Sushch, M. Pohl, A. Fedynitch, S. Das, R. Brose, P. Plotko, and D. M. A. Meyer. Production of secondary particles in heavy nuclei interactions in supernova remnants. *Astroparticle Physics*, 123:102490, December 2020.

C. I. Björnsson and S. T. Keshavarzi. Inhomogeneities and the modeling of radio supernovae. *Astrophysical Journal*, 841(1):12, 2017.

R. D. Blandford and D. Eichler. Particle acceleration at astrophysical shocks: A theory of cosmic ray origin. *Physics Reports*, 154(1):1–75, 1987.

R. D. Blandford and J. P. Ostriker. Particle acceleration by astrophysical shocks. *Astrophysical Journal*, 221:L29–L32, 1978.

P. Blasi. A semi-analytical approach to non-linear shock acceleration. *Astroparticle Physics*, 16(4):429–439, 2002a.

P. Blasi. A novel approach to non-linear shock acceleration. *Nuclear Physics B Proceedings Supplements*, 110:475–477, 2002b.

P. Blasi. Shock acceleration of electrons in the presence of synchrotron losses - I. Test-particle theory. *Monthly Notices of the RAS*, 402(4):2807–2816, 2010.

P. Blasi, S. Gabici, and G. Vannoni. On the role of injection in kinetic approaches to non-linear particle acceleration at non-relativistic shock waves. *Monthly Notices of the RAS*, 361:907–918, 2005.

P. Blasi, G. Morlino, R. Bandiera, E. Amato, and D. Caprioli. Collisionless shocks in a partially ionized medium. I. Neutral return flux and its effects on acceleration of test particles. *Astrophysical Journal*, 755:121, 2012.

John M. Blondin and Peter Lundqvist. Formation of the Circumstellar Shell around SN 1987A. *Astrophysical Journal*, 405:337, March 1993.

G. R. Blumenthal and R. J. Gould. Bremsstrahlung, synchrotron radiation, and Compton scattering of high-energy electrons traversing dilute gases. *Reviews of Modern Physics*, 42:237–271, 1970.

A. Bohdan, J. Niemiec, O. Kobzar, and M. Pohl. Electron pre-acceleration at non-relativistic high-Mach-number perpendicular shocks. *Astrophysical Journal*, 847:71, 2017.

R. Braun, S. F. Gull, and R. A. Perley. Physical process which shapes Cassiopeia A. *Nature*, 327:395–398, 1987.

R. Brose, I. Telezhinsky, and M. Pohl. Transport of magnetic turbulence in supernova remnants. *Astronomy and Astrophysics*, 593:A20, 2016.

R. Brose, I. Sushch, M. Pohl, K. J. Luken, M. D. Filipović, and R. Lin. Nonthermal emission from the reverse shock of the youngest Galactic supernova remnant G1.9+0.3. *Astronomy and Astrophysics*, 627:A166, July 2019.

R. Brose, M. Pohl, I. Sushch, O. Petruk, and T. Kuzyo. Cosmic-ray acceleration and escape from post-adiabatic supernova remnants. *Astronomy and Astrophysics*, 634: A59, February 2020.

M. Caragiulo and L. Di Venere. Evidence of hadronic interaction in Tycho supernova remnant using Fermi-LAT data. *Nuclear Physics B Proceedings Supplements*, 256:89–93, 2014.

G. Cassam-Chenaï, J. P. Hughes, J. Ballet, and A. Decourchelle. The blast wave of Tycho's supernova remnant. *Astrophysical Journal*, 665:315–340, 2007.

R. A. Chevalier. Self-similar solutions for the interaction of stellar ejecta with an external medium. *Astrophysical Journal*, 258:790–797, 1982.

R. A. Chevalier and J. Oishi. Cassiopeia A and its clumpy presupernova wind. *Astrophysical Journal, Letters*, 593:L23–L26, 2003.

P. Colella and P. R. Woodward. The piecewise parabolic method (PPM) for gas-dynamical simulations. *Journal of Computational Physics*, 54:174–201, 1984.

R. Cowsik and S. Sarkar. A lower limit to the magnetic field in Cassiopeia A. *Monthly Notices of the RAS*, 191:855–861, 1980.

Donald P. Cox. Cooling and Evolution of a Supernova Remnant. *Astrophysical Journal*, 178:159–168, November 1972.

A. Crusius and R. Schlickeiser. Synchrotron radiation in random magnetic fields. *Astronomy and Astrophysics*, 164(2):L16–L18, 1986.

T. DeLaney, L. Rudnick, M. D. Stage, J. D. Smith, K. Isensee, J. Rho, G. E. Allen, H. Gomez, T. Kozasa, W. T. Reach, J. E. Davis, and J. C. Houck. The three-dimensional structure of Cassiopeia A. *Astrophysical Journal*, 725(2):2038–2058, 2010.

T. DeLaney, N. E. Kassim, L. Rudnick, and R. A. Perley. The density and mass of unshocked ejecta in Cassiopeia A through low-frequency radio absorption. *Astrophysical Journal*, 785(1):7, 2014.

T. Douvion, P. O. Lagage, C. J. Cesarsky, and E. Dwek. Dust in the Tycho, Kepler and Crab supernova remnants. *Astronomy and Astrophysics*, 373:281–291, 2001.

L. O. Drury. An introduction to the theory of diffusive shock acceleration of energetic particles in tenuous plasmas. *Reports on Progress in Physics*, 46(8):973–1027, 1983a.

L. O. Drury. On particle acceleration in supernova remnants. *Space Science Reviews*, 36: 57–60, 1983b.

L. O. Drury and J. H. Völk. Hydromagnetic shock structure in the presence of cosmic rays. *Astrophysical Journal*, 248:344–351, 1981.

R. Dung and V. Petrosian. The dynamics of charged particles in turbulent astrophysical plasmas. *Astrophysical Journal*, 421:550, 1994.

R. Dung and R. Schlickeiser. The influence of the Alfvenic cross and magnetic helicity on the cosmic ray transport equation. I - Isospectral slab turbulence. *Astronomy and Astrophysics*, 240(2):537–540, 1990.

V. V. Dwarkadas. Interaction of Type Ia Supernovae with their surroundings: The exponential profile in two dimensions. *Astrophysical Journal*, 541:418–427, 2000.

V. V. Dwarkadas. Exploring the γ-ray emissivity of young supernova remnants - I. Hadronic emission. *Monthly Notices of the RAS*, 434:3368–3377, 2013.

V. V. Dwarkadas and R. A. Chevalier. Interaction of Type Ia Supernovae with their surroundings. *Astrophysical Journal*, 497:807–823, 1998.

E. Fermi. On the origin of the cosmic radiation. *Physical Review*, 75:1169–1174, 1949.

R. A. Fesen, M. C. Hammell, J. Morse, R. A. Chevalier, K. J. Borkowski, M. A. Dopita, C. L. Gerardy, S. S. Lawrence, J. C. Raymond, and S. van den Bergh. The expansion asymmetry and age of the Cassiopeia A supernova remnant. *Astrophysical Journal*, 645:283–292, 2006.

F. Fraschetti. Turbulent amplification of a magnetic field driven by the Dynamo effect at rippled shocks. *Astrophysical Journal*, 770:84, 2013.

T. K. Gaisser. *Cosmic rays and particle physics.* Cambridge University Press, 1990.

T. K. Gaisser, R. J. Protheroe, and T. Stanev. Gamma-ray production in supernova remnants. *Astrophysical Journal*, 492(1):219–227, 1998.

A. Gallegos-Cruz and J. Perez-Peraza. Derivation of analytical particle spectra from the solution of the transport equation by the WKBJ method. *Astrophysical Journal*, 446: 400, 1995.

P. Ghavamian, J. M. Laming, and C. E. Rakowski. A physical relationship between electron-proton temperature equilibration and Mach number in fast collisionless shocks. *Astrophysical Journal, Letters*, 654(1):L69–L72, 2007.

J. Giacalone and J. R. Jokipii. Magnetic field amplification by shocks in turbulent fluids. *Astrophysical Journal, Letters*, 663:L41–L44, 2007.

V. L. Ginzburg and S. I. Syrovatskiĭ. Origin Of Cosmic Rays. *Soviet Physics Uspekhi*, 9 (2):223–235, 1966.

H. L. Gomez, C. J. R. Clark, T. Nozawa, O. Krause, E. L. Gomez, M. Matsuura, M. J. Barlow, M. A. Besel, L. Dunne, W. K. Gear, P. Hargrave, T. Henning, R. J. Ivison, B. Sibthorpe, B. M. Swinyard, and R. Wesson. Dust in historical Galactic Type Ia supernova remnants with Herschel. *Monthly Notices of the RAS*, 420:3557–3573, 2012.

E. V. Gotthelf, B. Koralesky, L. Rudnick, T. W. Jones, U. Hwang, and R. Petre. Chandra detection of the forward and reverse shocks in Cassiopeia A. *Astrophysical Journal, Letters*, 552:L39–L43, 2001.

D. A. Green. A revised Galactic supernova remnant catalogue. *Bulletin of the Astronomical Society of India*, 37:45–61, 2009.

B. W. Grefenstette et al. Locating the most energetic electrons in Cassiopeia A. *Astrophysical Journal*, 802:15, 2015.

K. Greisen. End to the cosmic ray spectrum? *Physical Review Letters*, 16:748–750, 1966.

J. Guyer, D. Wheeler, and J. Warren. FiPy: Partial differential equations with Python. *Computing in Science and Engineering*, 11:6–15, 2009.

W. F. Hanlon. *The energy spectrum of ultra high energy cosmic rays measured by the High Resolution Fly's Eye observatory in stereoscopic mode.* PhD thesis, The University of Utah, 2008.

A. Hayato, H. Yamaguchi, T. Tamagawa, S. Katsuda, U. Hwang, J. P. Hughes, M. Ozawa, A. Bamba, K. Kinugasa, Y. Terada, A. Furuzawa, H. Kunieda, and K. Makishima. Expansion velocity of ejecta in Tycho's supernova remnant measured by Doppler broadened X-ray line emission. *Astrophysical Journal*, 725:894–903, 2010.

E. A. Helder and J. Vink. Characterizing the nonthermal emission of Cassiopeia A. *Astrophysical Journal*, 686:1094-1102, 2008.

E. A. Helder, J. Vink, A. M. Bykov, Y. Ohira, J. C. Raymond, and R. Terrier. Observational signatures of particle acceleration in supernova remnants. *Space Science Reviews*, 173:369–431, 2012.

J. F. Helmboldt and N. E. Kassim. The evolution of Cassiopeia A at low-radio frequencies. *Astronomical Journal*, 138(3):838–844, 2009.

V. F. Hess. Über Beobachtungen der durchdringenden Strahlung bei sieben Freiballonfahrten. *Physikalische Zeitschrift*, 13:1084–1091, 1912.

V. F. Hess. On the observations of the penetrating radiation during seven balloon flights. *arXiv e-prints*, page arXiv:1808.02927, 2018.

A. M. Hillas. TOPICAL REVIEW: Can diffusive shock acceleration in supernova remnants account for high-energy galactic cosmic rays? *Journal of Physics G Nuclear Physics*, 31(5):R95–R131, May 2005.

B. Hnatyk and O. Petruk. Evolution of supernova remnants in the interstellar medium with a large scale density gradient. I. General properties of the morphological evolution and x-ray emission. *Astronomy and Astrophysics*, 344:295, 1999.

C. Y. Huang, S. E. Park, M. Pohl, and C. D. Daniels. Gamma-rays produced in cosmic-ray interactions and the TeV-band spectrum of RX J1713.7-3946. *Astroparticle Physics*, 27:429–439, 2007.

J. P. Hughes. The expansion of the X-ray remnant of Tycho's supernova (SN 1572). *Astrophysical Journal, Letters*, 545:L53–L56, 2000.

J. P. Hughes, C. E. Rakowski, David N. Burrows, and P. O. Slane. Nucleosynthesis and mixing in Cassiopeia A. *Astrophysical Journal, Letters*, 528(2):L109–L113, 2000.

U. Hwang, A. Decourchelle, S. S. Holt, and R. Petre. Thermal and non-thermal X-ray emission from the forward shock in Tycho's supernova remnant. *Astrophysical Journal*, 581:1101–1115, 2002.

Z. J. Jiang, L. Zhang, and J. Fang. Spectral evolution of accelerated particles in supernova remnants. *Monthly Notices of the RAS*, 433:1271–1275, 2013.

F. C. Jones. Calculated spectrum of inverse-Compton-scattered photons. *Physical Review*, 167(5):1159–1169, 1968.

B. I. Jun and M. L. Norman. MHD simulations of Rayleigh-Taylor instability in young supernova remnants. *Astrophysics and Space Science*, 233:267–272, 1995.

H. Kang and D. Ryu. Diffusive shock acceleration in test-particle regime. *Astrophysical Journal*, 721:886–892, 2010.

N. E. Kassim, R. A. Perley, K. S. Dwarakanath, and W. C. Erickson. Evidence for thermal absorption inside Cassiopeia A. *Astrophysical Journal, Letters*, 455:L59, 1995.

T. Katou and T. Amano. Theory of stochastic shock drift acceleration for electrons in the shock transition region. *Astrophysical Journal*, 874(2):119, 2019.

S. Katsuda, R. Petre, J. P. Hughes, U. Hwang, H. Yamaguchi, A. Hayato, K. Mori, and H. Tsunemi. X-ray measured dynamics of Tycho's supernova remnant. *Astrophysical Journal*, 709:1387–1395, 2010.

S. R. Kelner, F. A. Aharonian, and D. Khangulyan. On the Jitter radiation. *Astrophysical Journal*, 774:61, 2013.

J. G. Kirk, R. Schlickeiser, and P. Schneider. Cosmic-ray transport in accelerating flows. *Astrophysical Journal*, 328:269, 1988.

J. G. Kirk, D. B. Melrose, E. R. Priest, A. O. Benz, and T. J.-L. Courvoisier. *Plasma Astrophysics*. Springer, 1994.

O. Klein and Y. Nishina. Über die Streuung von Strahlung durch freie Elektronen nach der neuen relativistischen Quantendynamik von Dirac. *Zeitschrift für Physik*, 52:853–868, 1929.

R. Kothes, K. Fedotov, T. J. Foster, and B. Uyanıker. A catalogue of Galactic supernova remnants from the Canadian Galactic plane survey. I. Flux densities, spectra, and polarization characteristics. *Astronomy and Astrophysics*, 457:1081–1093, 2006.

K. Koyama, R. Petre, E. V. Gotthelf, U. Hwang, M. Matsuura, M. Ozaki, and S. S. Holt. Evidence for shock acceleration of high-energy electrons in the supernova remnant SN1006. *Nature*, 378(6554):255–258, 1995.

A. V. Kozlova and S. I. Blinnikov. Distance estimate of Tycho's SNR. *Journal of Physics Conference Series*, 1038:012006, 2018.

O. Krause, S. M. Birkmann, T. Usuda, T. Hattori, M. Goto, G. H. Rieke, and K. A. Misselt. The Cassiopeia A supernova was of type IIb. *Science*, 320:1195–1197, 2008a.

O. Krause, M. Tanaka, T. Usuda, T. Hattori, M. Goto, S. Birkmann, and K. Nomoto. Tycho Brahe's 1572 supernova as a standard Type Ia as revealed by its light-echo spectrum. *Nature*, 456:617–619, 2008b.

G. F. Krymskii. A regular mechanism for the acceleration of charged particles on the front of a shock wave. *Akademiia Nauk SSSR Doklady*, 234:1306–1308, 1977.

R. M. Kulsrud and C. J. Cesarsky. The effectiveness of instabilities for the confinement of high energy cosmic rays in the Galactic disk. *Astrophysical Journal, Letters*, 8:189, 1971.

J. M. Laming and U. Hwang. On the determination of ejecta structure and explosion asymmetry from the X-ray knots of Cassiopeia A. *Astrophysical Journal*, 597(1):347, 2003.

M. Lampton, B. Margon, and S. Bowyer. Parameter estimation in X-ray astronomy. *Astrophysical Journal*, 208:177–190, 1976.

J. J. Lee, S. Park, J. P. Hughes, and P. O. Slane. X-ray observation of the shocked red supergiant wind of Cassiopeia A. *Astrophysical Journal*, 789:7, 2014.

M. M. Leroy, D. Winske, C. C. Goodrich, C. S. Wu, and K. Papadopoulos. The structure of perpendicular bow shocks. *Journal of Geophysical Research*, 87(A7):5081–5094, 1982.

S. Liu, Z. H. Fan, C. L. Fryer, J.-M. Wang, and H. Li. Stochastic electron acceleration in shell-type supernova remnants. *Astrophysical Journal, Letters*, 683:L163, 2008.

L. A. Lopez, B. W. Grefenstette, S. P. Reynolds, H. An, S. E. Boggs, F. E. Christensen, W. W. Craig, K. A. Eriksen, C. L. Fryer, C. J. Hailey, F. A. Harrison, K. K. Madsen, D. K. Stern, W. W. Zhang, and A. Zoglauer. A spatially resolved study of the synchrotron emission and Titanium in Tycho's supernova remnant using NuSTAR. *Astrophysical Journal*, 814:132, 2015.

Y. Maeda et al. Suzaku X-ray imaging and spectroscopy of Cassiopeia A. *Publications of the Astronomical Society of Japan*, 61:1217, 2009.

M. A. Malkov and L. O. Drury. Nonlinear theory of diffusive acceleration of particles by shock waves. *Reports on Progress in Physics*, 64:429–481, 2001.

M. A. Malkov, P. H. Diamond, and R. Z. Sagdeev. Mechanism for spectral break in cosmic ray proton spectrum of supernova remnant W44. *Nature Communications*, 2:194, 2011.

Y. Matsumoto, T. Amano, T. N. Kato, and M. Hoshino. Electron surfing and drift accelerations in a Weibel-dominated high-Mach-number shock. *Physical Review Letters*, 119:105101, 2017.

C. D. Matzner and C. F. McKee. The expulsion of stellar envelopes in core-collapse supernovae. *Astrophysical Journal*, 510:379–403, 1999.

W. J. Medd and K. V. V. Ramana. Flux-density measurements AR 3.15 Gc/s. *Astrophysical Journal*, 142:383, 1965.

P. G. Mezger, R. J. Tuffs, R. Chini, E. Kreysa, and H. P. Gemuend. Maps of Cassiopeia A and the Crab Nebula at lambda 1.2 MM. *Astronomy and Astrophysics*, 167:145–150, 1986.

G. Morlino and P. Blasi. Spectra of accelerated particles at supernova shocks in the presence of neutral hydrogen: the case of Tycho. *Astronomy and Astrophysics*, 589:A7, 2016.

G. Morlino and D. Caprioli. Strong evidence for hadron acceleration in Tycho's supernova remnant. *Astronomy and Astrophysics*, 538:A81, 2012.

J. A. Morse, R. A. Fesen, R. A. Chevalier, K. J. Borkowski, C. L. Gerardy, S. S. Lawrence, and S. van den Bergh. Location of the optical reverse shock in the Cassiopeia A supernova remnant. *Astrophysical Journal*, 614:727–736, 2004.

L. O'C. Drury, F. A. Aharonian, D. Malyshev, and S. Gabici. On the plasma temperature in supernova remnants with cosmic-ray modified shocks. *Astronomy and Astrophysics*, 496:1–6, 2009.

Y. Ohira. Effects of leakage neutral particles on shocks. *Astrophysical Journal*, 758:97, 2012.

Y. Ohira. Magnetic field amplification by collisionless shocks in partially ionized plasmas. *Astrophysical Journal*, 817:137, 2016.

S. Orlando, F. Bocchino, M. Miceli, O. Petruk, and M. L. Pumo. Role of ejecta clumping and back-reaction of accelerated cosmic rays in the evolution of Type Ia supernova remnants. *Astrophysical Journal*, 749:156, 2012.

S. Orlando, M. Miceli, M. L. Pumo, and F. Bocchino. Modeling SNR Cassiopeia A from the supernova explosion to its current age: The role of post-explosion anisotropies of ejecta. *Astrophysical Journal*, 822:22, 2016.

A. G. Pacholczyk. *Radio astrophysics. Nonthermal processes in galactic and extragalactic sources*. W. H. Freeman, 1970.

E. Parizot, A. Marcowith, J. Ballet, and Y. A. Gallant. Observational constraints on energetic particle diffusion in young supernovae remnants: amplified magnetic field and maximum energy. *Astronomy and Astrophysics*, 453:387–395, 2006.

E. A. Parker. Precise measurement of the flux densities of the radio sources Cas A and Cyg A at metre wavelengths. *Monthly Notices of the RAS*, 138:407, 1968.

C. Patrignani et al. Review of Particle Physics. *Chinese Physics C*, 40(10):100001, 2016.

M. Pohl. Leptonic origin of TeV gamma-rays from supernova remnants. *Astronomy and Astrophysics*, 307:L57–L59, 1996.

M. Pohl, H. Yan, and A. Lazarian. Magnetically limited X-ray filaments in young supernova remnants. *Astrophysical Journal, Letters*, 626:L101–L104, 2005.

M. Pohl, A. Wilhelm, and I. Telezhinsky. Reacceleration of electrons in supernova remnants. *Astronomy and Astrophysics*, 574:A43, 2015.

A. Putze, L. Derome, D. Maurin, L. Perotto, and R. Taillet. A Markov Chain Monte Carlo technique to sample transport and source parameters of Galactic cosmic rays. I. Method and results for the Leaky-Box model. *Astronomy and Astrophysics*, 497: 991–1007, 2009.

J. E. Reed, J. J. Hester, A. C. Fabian, and P. F. Winkler. The three-dimensional structure of the Cassiopeia A supernova remnant. I. The spherical shell. *Astrophysical Journal*, 440:706, 1995.

S. M. Ressler, S. Katsuda, S. P. Reynolds, K. S. Long, R. Petre, B. J. Williams, and P. F. Winkler. Magnetic field amplification in the thin X-ray rims of SN1006. *Astrophysical Journal*, 790:85, 2014.

R. Rettig and M. Pohl. The properties of non-thermal X-ray filaments in young supernova remnants. *Astronomy and Astrophysics*, 545:A47, 2012.

S. P. Reynolds. Supernova remnants at high energy. *Annual Review of Astronomy and Astrophysics*, 46:89–126, 2008.

S. P. Reynolds and D. C. Ellison. Electron acceleration in Tycho's and Kepler's supernova remnants - Spectral evidence of Fermi shock acceleration. *Astrophysical Journal, Letters*, 399:L75–L78, 1992.

Stephen P. Reynolds. Models of synchrotron x-rays from shell supernova remnants. *Astrophysical Journal*, 493(1):375.

B. Ryden. Radiative and magnetohydrodynamic shocks. http://www.astronomy.ohio-state.edu/~ryden/ast825/ch4.pdf, 2011. Accessed: 2019-04-11.

L. Saha, T. Ergin, P. Majumdar, M. Bozkurt, and E. N. Ercan. Origin of gamma-ray emission in the shell of Cassiopeia A. *Astronomy and Astrophysics*, 563:A88, 2014.

T. Sato, S. Katsuda, M. Morii, A. Bamba, J. P. Hughes, Y. Maeda, M. Ishida, and F. Fraschetti. X-ray measurements of the particle acceleration properties at inward shocks in Cassiopeia A. *Astrophysical Journal*, 853(1):46, 2018.

R. Schlickeiser. *Cosmic Ray Astrophysics*. Springer, 2002.

K. M. Schure, J. Vink, G. García-Segura, and A. Achterberg. Jets as diagnostics of the circumstellar medium and the explosion energetics of Supernovae: The case of Cassiopeia A. *Astrophysical Journal*, 686:399–407, 2008.

L. I. Sedov. *Similarity and Dimensional Methods in Mechanics*. Academic Press, 1959.

A. Shalchi. *Nonlinear Cosmic Ray Diffusion Theories*, volume 362. Springer, 2009.

P. Slane, S. H. Lee, D. C. Ellison, D. J. Patnaude, J. P. Hughes, K. A. Eriksen, D. Castro, and S. Nagataki. A CR-hydro-NEI model of the structure and broadband emission from Tycho's supernova remnant. *Astrophysical Journal*, 783:33, 2014.

J. D. T. Smith, L. Rudnick, T. Delaney, J. Rho, H. Gomez, T. Kozasa, W. Reach, and K. Isensee. Spitzer spectral mapping of supernova remnant Cassiopeia a. *Astrophysical Journal*, 693(1):713–721, 2009.

T. Stroman, M. Pohl, and J. Niemiec. Kinetic simulations of turbulent magnetic-field growth by streaming cosmic rays. *Astrophysical Journal*, 706(1):38–44, 2009.

A. W. Strong and I. V. Moskalenko. Propagation of cosmic-ray nucleons in the Galaxy. *Astrophysical Journal*, 509:212–228, 1998.

A. W. Strong, I. V. Moskalenko, and O. Reimer. Diffuse continuum gamma rays from the Galaxy. *Astrophysical Journal*, 537:763–784, 2000.

S. J. Sturner, J. G. Skibo, C. D. Dermer, and J. R. Mattox. Temporal evolution of nonthermal spectra from supernova remnants. *Astrophysical Journal*, 490(2):619, 1997.

I. Sushch, R. Brose, and M. Pohl. Modeling of the spatially resolved nonthermal emission from the Vela Jr. supernova remnant. *Astronomy and Astrophysics*, 2018.

T. Tamagawa, A. Hayato, S. Nakamura, Y. Terada, A. Bamba, J. S. Hiraga, J. P. Hughes, U. Hwang, J. Kataoka, K. Kinugasa, H. Kunieda, T. Tanaka, H. Tsunemi, M. Ueno, S. S. Holt, M. Kokubun, E. Miyata, A. Szymkowiak, T. Takahashi, K. Tamura, D. Ueno, and K. Makishima. Suzaku observations of Tycho's supernova remnant. *Publications of the ASJ*, 61:167, 2009.

G. Taylor. The formation of a blast wave by a very intense explosion. I. Theoretical discussion. *Proceedings of the Royal Society of London Series A*, 201(1065):159–174, 1950.

I. Telezhinsky, V. Dwarkadas, and M. Pohl. Particle spectra from acceleration at forward and reverse shocks of young Type Ia supernova remnants. *Astroparticle Physics*, 35: 300–311, 2012a.

I. Telezhinsky, V. V. Dwarkadas, and M. Pohl. Time-dependent escape of cosmic rays from supernova remnants, and their interaction with dense media. *Astronomy and Astrophysics*, 541:A153, 2012b.

I. Telezhinsky, V. V. Dwarkadas, and M. Pohl. Acceleration of cosmic rays by young core-collapse supernova remnants. *Astronomy and Astrophysics*, 552:A102, 2013.

A. Thornbury and L. O. Drury. Power requirements for cosmic ray propagation models involving re-acceleration and a comment on second-order Fermi acceleration theory. *Monthly Notices of the RAS*, 442:3010–3012, 2014.

J. Threlfall, K. G. McClements, and I. De Moortel. Alfvén wave phase-mixing and damping in the ion cyclotron range of frequencies. *Astronomy and Astrophysics*, 525:A155, 2011.

W. W. Tian and D. A. Leahy. Tycho SN 1572: A naked Ia supernova remnant without an associated ambient molecular cloud. *Astrophysical Journal, Letters*, 729:L15, 2011.

A. Tran, B. J. Williams, R. Petre, S. M. Ressler, and S. P. Reynolds. Energy dependence of synchrotron X-ray rims in Tycho's supernova remnant. *Astrophysical Journal*, 812: 101, 2015.

R. Trotta, G. Jóhannesson, I. V. Moskalenko, T. A. Porter, R. Ruiz de Austri, and A. W. Strong. Constraints on cosmic-ray propagation models from a global bayesian analysis. *Astrophysical Journal*, 729(2):106, 2011.

J. K. Truelove and C. F. McKee. Evolution of non-radiative supernova remnants. *Astrophysical Journal, Supplement*, 120:299–326, 1999.

Y. Uchiyama and F. A. Aharonian. Fast variability of non-thermal X-ray emission in Cassiopeia A: Probing electron acceleration in reverse-shocked ejecta. *Astrophysical Journal, Letters*, 677:L105–L108, 2008.

D. Urošević. On the radio spectra of supernova remnants. *Astrophysics and Space Science*, 354:541–552, 2014.

R. Vainio and R. Schlickeiser. Self-consistent Alfvén-wave transmission and test-particle acceleration at parallel shocks. *Astronomy and Astrophysics*, 343:303–311, 1999.

M. van Adelsberg, K. Heng, R. McCray, and J. C. Raymond. Spatial structure and collisionless electron heating in Balmer-dominated shocks. *Astrophysical Journal*, 689 (2):1089–1104, 2008.

M. P. van Haarlem et al. LOFAR: The LOw-Frequency ARray. *Astronomy and Astrophysics*, 556:A2, 2013.

E. N. Vinyaikin. Frequency dependence of the evolution of the radio emission of the supernova remnant Cas A. *Astronomy Reports*, 58:626–639, 2014.

A. Vladimirov. *Modeling magnetic field amplification in nonlinear diffusive shock acceleration*. PhD thesis, North Carolina State University, 2009.

H. J. Völk, E. G. Berezhko, and L. T. Ksenofontov. Internal dynamics and particle acceleration in Tycho's SNR. *Astronomy and Astrophysics*, 483:529–535, 2008.

C. Y. Wang and R. A. Chevalier. Instabilities and clumping in Type Ia supernova remnants. *Astrophysical Journal*, 549:1119–1134, 2001.

W. Wang and Z. Li. Hard X-ray emissions from Cassiopeia A observed by INTEGRAL. *Astrophysical Journal*, 825:102, 2016.

J. S. Warren, J. P. Hughes, C. Badenes, P. Ghavamian, C. F. McKee, D. Moffett, P. P. Plucinsky, C. Rakowski, E. Reynoso, and P. Slane. Cosmic-ray acceleration at the forward shock in Tycho's supernova remnant: Evidence from Chandra X-ray observations. *Astrophysical Journal*, 634:376–389, 2005.

K. E. Weil, R. A. Fesen, D. J. Patnaude, J. C. Raymond, R. A. Chevalier, D. Milisavljevic, and C. L. Gerardy. Detection of the Red Supergiant Wind from the Progenitor of Cassiopeia A. *Astrophysical Journal*, 891(2):116, March 2020.

B. J. Williams, K. J. Borkowski, P. Ghavamian, J. W. Hewitt, S. A. Mao, R. Petre, S. P. Reynolds, and J. M. Blondin. Azimuthal density variations around the rim of Tycho's supernova remnant. *Astrophysical Journal*, 770:129, 2013.

H. Yan and A. Lazarian. Scattering of cosmic rays by magnetohydrodynamic interstellar turbulence. *Physical Review Letters*, 89:281102, 2002.

H. Yan and A. Lazarian. Cosmic-ray scattering and streaming in compressible magnetohydrodynamic turbulence. *Astrophysical Journal*, 614:757–769, 2004.

H. Yan and A. Lazarian. Cosmic-ray propagation: Nonlinear diffusion parallel and perpendicular to mean magnetic field. *Astrophysical Journal*, 673(2):942–953, 2008.

Y. Yuan, S. Funk, G. Jóhannesson, J. Lande, L. Tibaldo, and Y. Uchiyama. Fermi Large Area Telescope detection of a break in the gamma-ray spectrum of the supernova remnant Cassiopeia A. *Astrophysical Journal*, 779:117, 2013.

X. Zhang and S. Liu. Is supernova remnant Cassiopeia A a PeVatron? *Astrophysical Journal*, 874(1):98, 2019.

X. Zhang, Y. Chen, H. Li, and X. Zhou. On the hadronic γ-ray emission from Tycho's supernova remnant. *Monthly Notices of the RAS*, 429:L25–L29, 2013.

V. N. Zirakashvili and F. A. Aharonian. Nonthermal radiation of young supernova remnants: The case of RX J1713.7-3946. *Astrophysical Journal*, 708:965–980, 2010.

V. N. Zirakashvili and V. S. Ptuskin. Diffusive shock acceleration with magnetic amplification by non-resonant streaming instability in supernova remnants. *Astrophysical Journal*, 678:939–949, 2008.

V. N. Zirakashvili, F. A. Aharonian, R. Yang, E. Oña-Wilhelmi, and R. J. Tuffs. Nonthermal radiation of young supernova remnants: The case of Cas A. *Astrophysical Journal*, 785:130, 2014.

Eidesstattliche Erklärung

Hiermit erkläre ich, dass ich die vorliegende Arbeit eigenständig und ohne fremde Hilfe angefertigt habe. Textpassagen, die wörtlich oder dem Sinn nach auf Publikationen oder Vorträgen anderer Autoren beruhen, sind als solche kenntlich gemacht. Die Arbeit wurde bisher keiner anderen Prüfungsbehörde vorgelegt und auch noch nicht veröffentlicht.

Berlin, den 13.01.2021